University of Massachusetts Amherst

ScholarWorks@UMass Amherst

March 2019

TARGETED DESIGN OF CO-CONTINUOUS NANOSTRUCTURES IN COPOLYMERS

Di Zeng

Follow this and additional works at: https://scholarworks.umass.edu/dissertations_2

Part of the Polymer Science Commons

TARGETED DESIGN OF CO-CONTINUOUS NANOSTRUCTURES
IN COPOLYMERS

A Dissertation Presented

by

DI ZENG

Submitted to the Graduate School of the
University of Massachusetts Amherst
in partial fulfillment of the requirements for the degree of

DOCTOR OF PHILOSOPHY

February 2019

Polymer Science and Engineering

TARGETED DESIGN OF CO-CONTINUOUS NANOSTRUCTURES
IN COPOLYMERS

A Dissertation Presented

by

DI ZENG

Approved as to style and content by:

_____
Ryan C. Hayward, chair

_____
Gregory M. Grason, member

_____
Wei Fan, member

_____
E. Bryan Coughlin, Department Head
Polymer Science and Engineering

DEDICATION

To my families

ACKNOWLEDGEMENTS

First and foremost, I would like to thank my advisor and mentor, Professor Ryan Hayward. I have always felt spoiled to work with him because he is so knowledgeable and he will always be patient to guide and teach me over the past five years. His critical thinking has also reminded me of keeping learning and exploring new areas. I also greatly appreciate his professional attitude in science, which has shaped me as a researcher in both academic and industrial environments. Thank you!

I sincerely thank my thesis committee, Professor Gregory Grason and Professor Wei Fan, for their continuous comments and suggestions, helping me to understand my works from different angles. It is my great pleasure and honor to work under these smart scientists, and they have always encouraged, taught me great ideas by sharing their scientific insight. I also want to thank Professor Yi Gu in Sichuan University who brought me into polymers during my B.S.

I would like to thank my collaborators: Professor E. Bryan Coughlin, S. Piril Ertem, Rohit Gupta, Haomian Yuan, Alexander Ribbe from UMass, Zhenpeng Li from Case Western, Marc Schroeder and Rene Arbter from BASF. They provided me countless help, enriched my scientific background and taught me how to communicate with broader communities. I am also grateful to all past and present Hayward group members: Kyuyoung, Laju, Junhee, Seog-Jin, Weiguo, Soonyong, Ji-Hwan, Hyeong-Jun, Dayong, Cheolhee, Maria, Rachel, Kyle, Anesia, Nakul, Daniel, Adam, Ying, Tetsu, Hyunki, Qi, Alexa, Carolyn, Minjung, David and Jaechul. They are always sharing new ideas to solve all

kinds of problems and bringing many joys to our daily life in Conte. I will never be able finish my PhD in a good shape without this incredible working environment.

I would also like to thank all the faculty members in the Polymer Science and Engineering department who brought me to this department, and taught me in and out of classes. Their classes will always be one of the great resources for me to understand and solve scientific problems in the future. I would also like to express my gratitude to the great PSE staff: Lisa Groth, Alyssa Kristek, Maria Farrigton, Sophie Hsu, Linda Chatfield, Madelyne Skrocki, Sekar Thirunavukkarasu, Alexander Ribbe, and Louis Raboin for their administrative assistance and technical support.

Many thanks to the class of 2013, I feel so blessed to study and work close to them all. The memories of having classes in the same room, going through the first year and cumes together will always be one big part of my PhD journey. Last but not the least, huge thanks to all my great friends in Amherst for making my time here enjoyable and unforgettable. Thanks for offering so many first-time experiences: softball, snowboarding, rafting…and of course big thanks to the dinner groups, they have been more than friends to me, and I will always consider them as my second families in US. I will cherish the memories forever, and best of lucks to all of them.

Finally, I want to thank my parents, grandparents, big families, and Ying for their uncountable love. Nothing would be accompanied without their unconditional support for the years.

ABSTRACT

TARGETED DESIGN OF CO-CONTINUOUS NANOSTRUCTURES IN COPOLYMERS

FEBRUARY 2019

DI ZENG, B.S., SICHUAN UNIVERSITY

M.S., UNIVERSITY OF MASSACHUSETTS AMHERST

PH.D., UNIVERSITY OF MASSACHUSETTS AMHERST

Directed by Professor Ryan C. Hayward

Microphase separated copolymers with nano-scale morphologies are critically important in designing next generation materials. Cocontinuous nanoscale structures, in which domains of multiple different phases each simultaneously percolate in three dimensions, provide opportunities to synergistically combine properties of the constituent polymers in a wide variety of contexts. While cocontinuous nanostructures are fabricated through equilibrium self-assembly of block or graft copolymers and kinetically trapped phase separation of polymer blends or crosslinked copolymer networks, their formation is highly sensitive to changes in chemical details, synthesis and/or processing conditions, bringing practical challenges to generalization to multiple systems.

In this dissertation, we focus on transforming the design of cocontinuous morphologies from complicated protocols to general and robust principles by pre-designing telechelic polymers with well-defined end functionality, molecular weight and polydispersity. Relying on end-linking of telechelic polystyrene (PS) and poly ($_{D,L}$ - Lactide) (PLA) with a multi-functional crosslinker, randomly end-linked copolymer networks (RECNs) are synthesized and thoroughly characterized. Particularly, for the first time we are able to map the phase diagram of symmetric ($M_{n, A} \approx M_{n, B}$) RECNs, highlighting the critical microphase separation transition ($6 < (\chi N)_{critical} < 12$), above which disordered cocontinuous nanostructures span over 30 vol% and morphologies with dispersed domains reside on either side. The critical impacts of chemical parameters (strand length M_n, strand asymmetry, strand dispersity $Đ$, junction functionality) are further evaluated to influence the microphase separated structures. While maintaining cocontinuity, uniaxial stretching of PS/PLA RECNs above the glass transition temperatures introduces controlled orientation through a two-step process (domain stretching and domain rotation), which is found to provide substantial improvements in yield strength, toughness, and stiffness for bulk materials at room temperature. Nanoporous materials with interconnected porous structures are then fabricated by selective removal of the easily degradable PLA domains.

Lastly, linear and branched multi-block copolymers (MBCs) with various block length are fabricated using step polymerization of telechelic PS and PLA. In addition to their ability to form cocontinuous morphologies within microphase

separated and non-crosslinked MBCs, their solubility is dramatically improved in comparison to crosslinked copolymers.

TABLE OF CONTENTS

LIST OF TABLES

LIST OF FIGURES

CHAPTER 1

INTRODUCTION AND BACKGROUND

1.1 Fundamentals of Polymer Phase Separation

Polymer based materials have been extensively studied in the past decades, covering a wide range of applications, including aerospace, automotive, medical and packaging.[1] The nanostructure of a materials is critically important to its macroscopic properties, and therefore determining the potential applications in various environments. Combining different polymeric components into a composite provides a way to integrate multiple properties into a single material. For a two-component linear polymers mixture, the free energy change upon mixing ∆G is given by Flory - Huggins theory,[2,3]

$$\frac{\Delta G}{k_B T} = \frac{\varphi_A}{N_A} ln\varphi_A + \frac{\varphi_B}{N_B} ln\varphi_B + \chi\varphi_A\varphi_B$$

with k_B representing the Boltzmann constant, T the temperature, N_A and N_B the degree of polymerization, φ_A and φ_B the volume fraction and χ Flory-Huggins segment-segment interaction parameter. On the right of this equation, the first two terms reflect the entropy of mixing, while χ in the last term indicates the enthalpy of mixing.

1.2 Co-continuous Morphologies in Binary Copolymers

Physically blending two linear polymers usually serves as the easiest method to achieve phase separation in a binary system; however, phase separation usually results in two macroscopically separated phases at

equilibrium. In many cases, understanding and controlling much smaller structures (nano, or micro scale) are required in order to tune the material properties.[4]
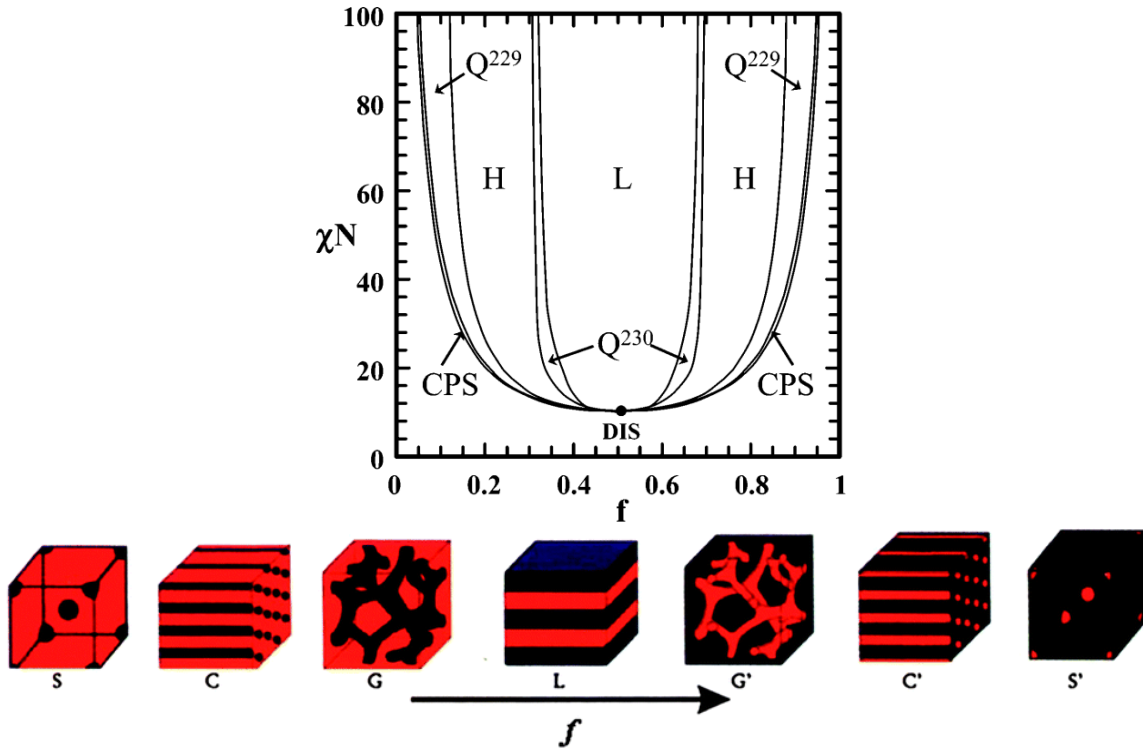
Figure 1. Theoretical phase diagram of diblock copolymers. Reproduced from reference [5,6].

Copolymers formed by covalently linking A and B chains have been intensively studied because of their ability to microphase separate into a variety of structures on the scale of tens to hundreds of nanometers. As seen in the phase diagram of diblock copolymers in Figure 1, morphologies, including spherical, cylindrical, lamellar, and gyroid, are accessible when varying the compositions.[5] Among those morphologies, the co-continuous double gyroid phase, in which both phases simultaneously percolate in three dimensions through the materials, provides particular interesting opportunities to synergistically combine properties of the constituent materials in a wide variety of

contexts, ranging from mass transportation, separations, catalysis, sensing, and energy storage.[7–13]

Although gyroid phase has been widely investigated, it typically only occupies only a narrow region.[14] An alternative approach to achieve co-continuous nanostructures relies on the microphase separation of crosslinked copolymers, where the presence of crosslinks quenches the phase separation. This tends to frustrate the formation of ordered structures and generate co-continuous morphology. Examples include, but are not limited to, amphiphilic polymer conetworks (APCNs)[15], interpenetrating networks (IPNs)[16], and polymerization induced phase separation (PIPS)[17]. APCNs can be defined as two-component networks of covalently interconnected hydrophilic/hydrophobic phases of co-continuous morphology.[18–23] Although continuity of the two phases has been discussed and demonstrated through swelling of the networks in both water and organic solvent, this method leaves some ambiguity, since minority domains can potentially rearrange and become continuous in the presence of a good solvent. Therefore, this swelling method doesn't necessarily prove continuity in dry state. Similarly, in many cases, disordered co-continuous morphologies are also observed in IPNs formed by, either simultaneously growing two crosslinked networks, or sequentially crosslinking the second in the first network swelled by monomers and crosslinkers.[24–28] Notably, this method typically requires precise control of the growth kinetics to achieve the desired co-continuous morphology. A variety of morphologies, including dispersed domains of one phase in another continuous matrix, or co-continuous structures, have

also been studied in PIPS, and they are generally sensitive to reaction and processing conditions.[29–32] In addition, simultaneous crosslinking and polymerization lead to poorly defined network structures, making it hard to predict and design the desired morphology.

In summary, although equilibrium and non-equilibrium co-continuous structures can be fabricated using a variety of copolymers architectures, limitations remain with respect to the robustness and generality of these methods. Firstly, the relative kinetics of phase separation and polymerization/crosslinking results in the competition between micro and macro phase separation, thus making the structures highly sensitive to the system itself and the reaction conditions. Second, the lack of well-defined strand parameters, i.e. molecular weight and polydispersity, makes it difficult to design a generalized method to fabricate co-continuous structures. In contrast to the phase behavior of diblock copolymers, where well designed structures are experimentally predictable, those crosslinked networks unfortunately suffer from greater difficulty in targeting desired nanostructures.

1.3 Randomly End-linked Copolymer Networks (RECNs)

1.3.1 Definition

As illustrated in Figure 2, randomly end-linked copolymer networks (RECNs) represent a class of crosslinked copolymer networks with well-defined architectures, which provide a simple, robust and general pathway to co-continuous nanostructured materials. Specifically, starting from well characterized linear telechelic polymers dissolved in non-selective solvent, the

chains are first end-linked with a multi-functional crosslinker, and microphase separation to a structure with characteristic size d is subsequently induced by removing the solvent. Due to the presence of solvent during crosslinking, screening of unfavorable interactions between the polymers by the non-selective solvent decreases the effective interaction parameter χ_{eff} in solution, ideally below that needed to drive phase separation. For concentrated solutions, χ_{eff} is reduced to $\chi_{eff} = \chi\varphi$, where χ is the Flory-Huggins parameter in the melt and φ is the volume fraction of polymers in solution, according to the mean field theory.[33] Further reduction of χ_{eff} in a semidilute solution is predicted, because the swelling of polymer chains changes their conformation and spatial correlations,[34] and the scaling of $\chi_{eff} = \chi\varphi^{\beta}$ with β = 1.3 - 1.6 is anticipated by Fredrickson and Leibler[35], and by Lodge and coworkers.[36,37] Thus, we expect that the removal of solvent will lead to a significant increase of χ_{eff}, thereby driving microphase separation within the networks.

Importantly, RECNs combine the advantages of block copolymer (well-defined strand parameters) and crosslinked networks (frustrated phase separation favoring co-continuous structures), therefore serving as an ideal platform to fabricate co-continuous nanostructures with high robustness and generality. Given the well-defined telechelic polymers and reasonably simple network structures, we provide a fundamental understanding of the microphase separation behavior of RECNs, transforming the design of co-continuous morphologies from complicated protocols to general and robust principles.
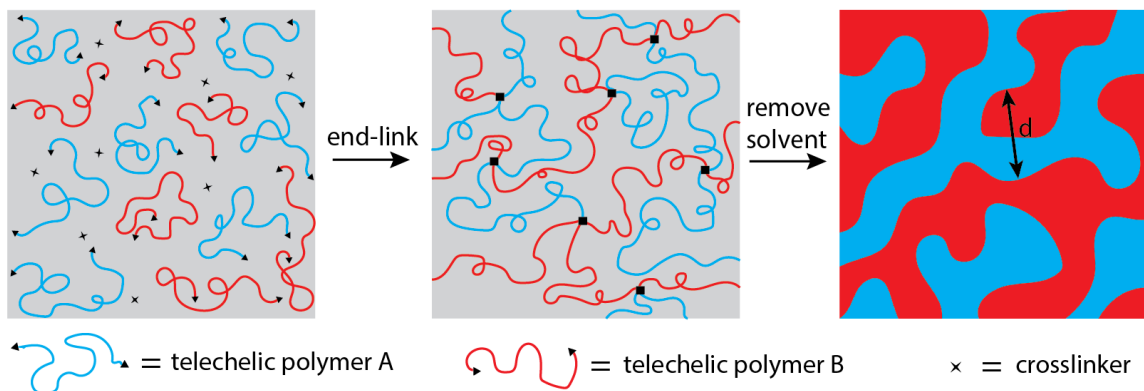
Figure 2. Schematic depiction of the preparation of RECNs by end-linking telechelic polymers in a good solvent, followed by solvent removal.

1.3.2 Previous Studies

Theoretical studies on RECNs were first conducted by de Gennes,[38] who predicted the critical point of microphase separation transition (MST) at $\chi_c(N_A + N_B) = 13.6$ for a symmetric binary RECNs, where N is strand length. The structure factor was also calculated to evolve as $S(q^*) \sim (\chi - \chi_c)^{-1}$, where q^* (corresponds to the peak position in a scattering experiment) scales with $N^{0.5}$. Experimentally, Briber and Bauer[39] have investigated RECNs of deuterated polystyrene (dPS) and poly(vinyl methyl ether)(PVME), and found the variation of $q^* \sim N^{0.5}$ and $S(q^*) \sim \chi^{-1}$, in agreement with prediction of de Gennes' work. However, de Gennes predicted the zero-scattering intensity at $q = 0$, and it is clear from the experiment that non-zero scattering exists in this network. It was then explained by Benmouna and co-workers[40] that the discrepancy arises from the absence of concentration fluctuations in random phase approximation. Indeed, concentration fluctuations exist in most random systems prior to crosslinking, and thus produces zero scattering. McLeish and co-workers have then calculated that $S(q^*)$ diverges as $(\chi - \chi_c)^{-2}$ near the MST, a prediction that

has been supported by simulations[41,42], and they have also calculated a higher critical point with $\chi_c(N_A + N_B) = 19.2$.

Most recently, several experiments have developed this type of ideal network architectures, including polyethylene oxide (PEO)/polydimethylsiloxane (PDMS)[43,44] and polyisobutylene (PIB)/PEO.[45] The morphologies have been assigned as disordered co-continuous nanostructures by transmission electron microscopy (TEM) or swelling measurements in both water and organic solvents, while no further direct evidence has confirmed the co-continuity.[43–46] Our group in collaboration with the Tew group, has considered RECNs formed by end-linking telechelic polystyrene (PS) and PEO with a tetra-functional crosslinker using thiol-ene chemistry. Li ions were incorporated to frustrate the crystallization of PEO phases and provide a pathway to study the continuity of PEO.[47] Measurements of the elastic modulus of above the T_g of PEO but below that of PS provided evidence on the continuity of PS. It was found that the co-continuous window spans over a large composition window, from 0.30 to 0.65 in volume fraction.

Chapter 2

INTERCONNECTED NANOPOROUS MATERIALS FROM RECNS*

2.1 Introduction

Interconnected porous structures where both the matrix and the pores form three-dimensionally (3D) percolating networks are beneficial, because the matrix provides mechanical robustness, while the highly interconnected pores facilitate mass transport and provide large surface areas and porosities, without the need to obtain a high degree of global alignment as generally required for materials with cylindrical pores.[48] Routes to generate polymeric membranes with continuous pore structures can broadly be divided into two approaches: equilibrium self-assembly and kinetically trapped phase separation. With regards to equilibrium routes, the self-assembly of diblock copolymers into double gyroid nanostructures, followed by selective etching of the minority domain, represents an attractive route to porous monoliths with percolating pores of precisely defined sizes.[48–52] However, as this structure is formed only over a narrow range of polymer composition (~ 5 vol%),[5] precisely controlled synthesis and processing conditions are generally required. To kinetically trap bicontinuous structures in systems undergoing phase separation, a wide variety of methods have been employed, including phase inversion techniques widely used to make commercial filtration membranes,[12] solvent[53,54] or crystallization[55] induced phase separation, sol-gel processes,[56] and crosslinking during melt mixing.[57]

Recently, polymerization induced phase separation (PIPS) of mixtures including a degradable polymer has been established as a facile route to interconnected porous materials with well-controlled pore sizes.[58,59] However, as in all examples of kinetically-trapped structures, fine control over the relative rates of phase separation and structural arrest is generally required to obtain the desired structure.

As discussed in Chapter 1, crosslinked copolymer networks containing two or more immiscible network strands, including amphiphilic polymer conetworks (APCNs),[15] interpenetrating networks (IPNs),[16] and networks formed by PIPS[17] are well known to microphase separate into co-continuous structures under appropriate conditions.[19,24,58–61] However, in many cases, the lack of well-controlled strand molecular weights and the sensitivity of network structure to the reaction conditions make it difficult to determine *a priori* where co-continuous structures will be found. In this regard, randomly end-linked copolymer networks (RECNs) formed by reaction of telechelic linear polymer chains with multi-functional crosslinkers in a good solvent for all components, present a particularly interesting class of materials, since they provide comparatively well-controlled network parameters such as strand stoichiometry and length.[44,47] For example, Walker, et al.[47] recently showed that, following solvent removal, RECNs of PS/PEO undergo microphase separation into disordered co-continuous morphologies over a wide range of network compositions (spanning > 30% by volume), thus providing a simple and robust means to achieve this desirable morphology. Despite these advantages, however,

this approach has not yet been applied to generate nanoporous polymeric materials.

In this chapter, we demonstrate that interconnected porous materials based on RECNs can be formed from PS and the degradable polymer poly(D, L-lactide) (PLA). We find that the bicontinuous window spans over 30 vol% for samples with strand number average molecular weights M_n of 11 and 10 kg/mol, respectively, for PS and PLA, and that by selectively etching the PLA phase, free-standing materials with highly interconnected pores can be generated. Further experiments show that pore sizes can be tuned simply by adjusting the designed molecular weight of precursors, in reasonable agreement with the scaling relationship $d \sim M_n^{0.5}$ predicted by De Gennes for randomly crosslinked blends.[38]

2.2 Materials and Methods

2.2.1 Fabrication of Nanoporous PS monoliths

Our approach to form RECNs relies on urethane end-linking chemistry using two different dihydroxyl-terminated polymers homogeneously mixed in solution along with a tetra-isocyanate small molecule crosslinker (Figure 3). We chose PS and PLA as a model system to study the formation of interconnected porous materials for a number of reasons. The driving force for segregation between PS and PLA in the absence of solvent is reasonably high, corresponding to a Flory-Huggins parameter (χ) of about 0.2 at 20 °C,[62] thus enabling microphase separation for fairly low molecular weights, and therefore access to small pore sizes. Furthermore, PLA is non-crystalline and can easily be

selectively etched under basic conditions (pH > 7), while PS provides a high modulus structural phase.
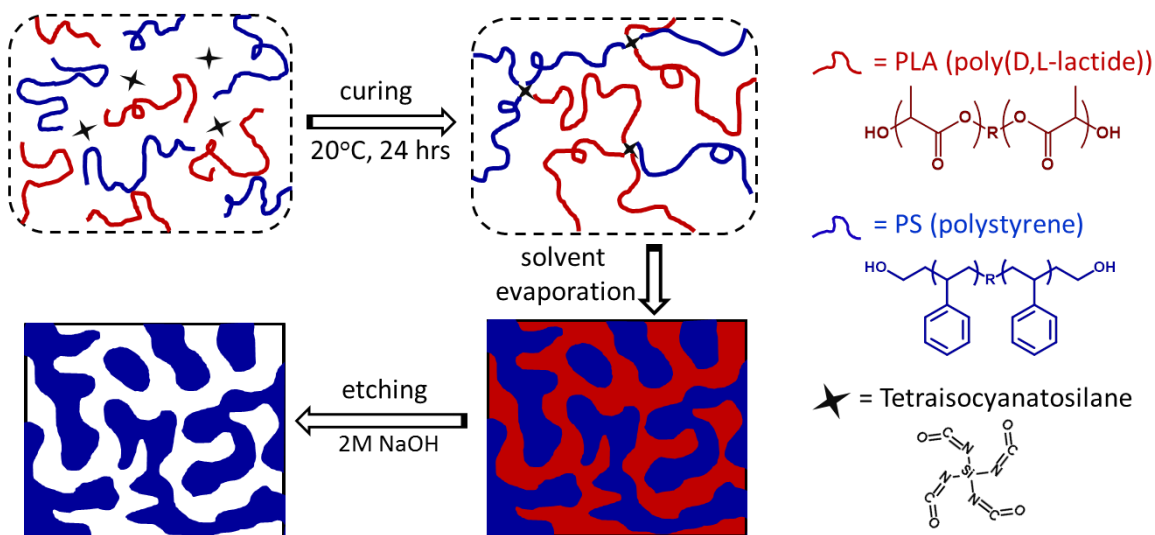
Figure 3. Schematic depiction of the preparation of interconnected porous samples from hydroxyl end-functionalized precursor polymers.
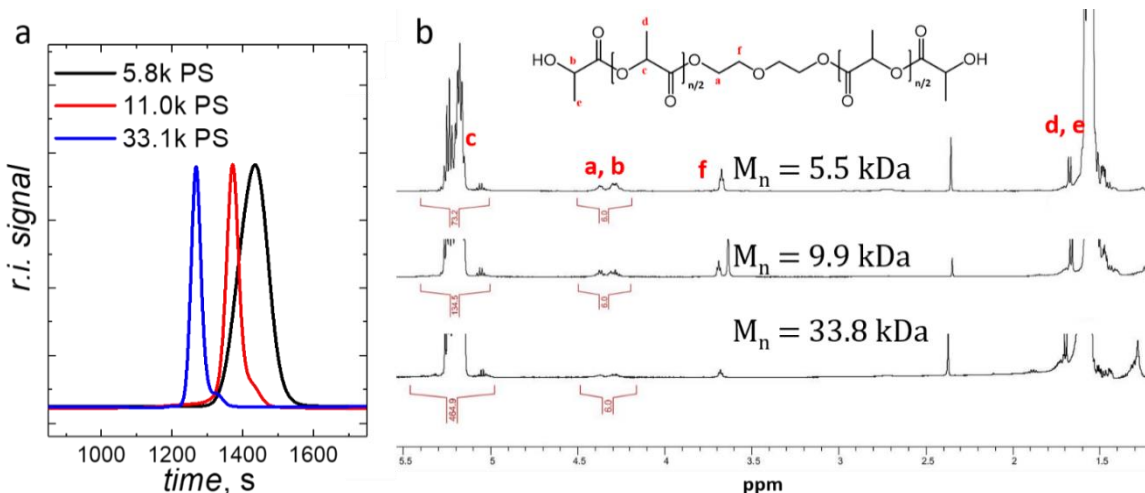
Figure 4. (a) GPC chromatograms for PS-diol strands. (b) Molecular weights of PLA as characterized by NMR using peaks at 4.29 ppm (a, 4*H*, -COO-C*H*2-), 4.37 ppm (b, 2*H*, HO-C*H*(CH3)-COO-), and 5.2 ppm (c, n*H*, -COO-C*H*(CH3)-COO-). M_n was calculated by end-group analysis to be 5.5 kg/mol, 9.9 kg/mol and 33.8 kg/mol, respectively.

Dihydroxyl-terminated PS and PLA, tetraisocyanatosilane, methanol and anhydrous tetrahydrofuran were purchased from Polymer Source, Advanced Polymer Materials, Gelest, Fisher Scientific, and Sigma Aldrich, respectively, and

used without further purification. Functionalities of PS and PLA provided by the suppliers are 1.9 and 2.0, respectively.

In this chapter, we focus on RECNs that are nearly symmetric with regards to strand molecular weight, in particular three different systems with respective M_n values for PS and PLA of 6 and 5 kg/mol, 11 and 10 kg/mol, or 33 and 34 kg/mol. PS and PLA are dissolved in tetrahydrofuran (THF) in a nitrogen-filled glove bag to a total polymer concentration of 30 wt% (or 15 wt% in the case of 33 kg/mol PS and 34 kg/mol PLA, as 30 wt% solutions of these polymers undergo phase separation), followed by addition of tetraisocyanatosilane with NCO/OH = 1.4. This modest excess of isocyanate groups is selected as it gives networks with gel fractions typically > 95 wt% (though only > 90 wt% for the 33 kg/mol PS and 34 kg/mol PLA system), compared to values of less than 80 wt% for NCO/OH = 1.0 or 1.2, presumably a fraction of the isocyanate groups react with water, thereby lowering the effective functionality of the crosslinkers. The gel was dried under N_2 flow for 1 d and then immersed into THF for 1 d to extract the sol portion, followed by drying under N_2 flow for 1 d and in a vacuum chamber for 1 d. The dry sample was then immersed in a 2 M solution of NaOH in water/methanol (6/4, v/v) for a defined length of time to selectively remove PLA domains, followed by washing with water/methanol (6/4, v/v) at least three times. The sample was finally dried under reduced pressure for 1 d.

Samples are named following the convention $S_{MPS}L_{MPLA}$ - X, where the subscripts refer to the molecular weights of the respective strands and X

represents the percentage by weight of PLA initially present in solution prior to end-linking.

2.2.2 Characterization

^{1}H NMR spectra were measured at 500 MHz using a Bruker 500 Ascend spectrometer and chloroform-d as the solvent. Gel permeation chromatography (GPC) was performed using an Agilent 1260 series system. THF was used as the eluent at a flow rate of 1.0 mL/min. Differential scanning calorimetry (DSC) measurements were conducted using a TA Instruments DSC Q200 and samples were analyzed under a heating rate of 5 ^{o}C/min under a flow of nitrogen (50 mL/min). Fourier transform infrared spectroscopy (FTIR) was measured using PerkinElmer Spectrum 100. Small-angle X-ray scattering (SAXS) measurements were performed using GANESHA 300 XL SAXS and samples were prepared with thickness around 2 mm. For transmission electron microscopy (TEM) analysis, ultra-thin sections were cut on a Leica Ultracut UCT microtome operating at -70 ^{o}C, stained with RuO_4 for 10 min, and imaged using a JEOL 2000FX operating at an accelerating voltage of 200 kV. Scanning electron microscope (SEM) measurements were conducted using a Magellan 400 FESEM in immersion mode. Samples were coated with 1 nm of Au using a Cressington Sputter Coater 108. For N_2 adsorption isotherm analysis, a sample tube was filled with dried sample (40–70 mg) and thoroughly dried in vacuum at 60 °C for 1 d and then was measured with Micromeritics Tristar II at 77.3 K. A thin porous sample for TEM tomography was prepared using a Leica Ultracut UCT cryo-ultramicrotome at -70 ^{o}C. A drop of basic solution (2 M solution of NaOH in water/methanol) was placed

13

on the TEM grid to remove PLA, followed by washing with water/methanol. A tilt

series from - 60⁰ to + 60⁰ at 1⁰ intervals was collected using a JEOL-2200FS

EFTEM transmission electron microscope operated at 200 kV. To increase

contrast, zero-loss filtering was applied employing a slit aperture of ΔE = 20 eV

after the energy filter. Reconstructions were performed using etomo part of the

IMOD software[63] applying simple back projection algorithm. Volume rendering

was done using UCSF Chimera[64] through applying a 3D Gaussian filter and

choosing a threshold to delineate pores from PS walls by matching the porosity

to the value measured by N_2 adsorption. ImageJ was used for flood filling

analysis, porosity and pore size distribution calculation (using the bonej

plugin[65]).

2.3 Results and Discussion

2.3.1 Interconnected Nanoporous PS

We first characterize the formation of interconnected nanoporous

materials from RECNs consisting of 11 kg/mol PS and 10 kg/mol PLA. The

extent of removal of PLA domains is studied by gravimetry, Fourier transform

infrared spectroscopy (FTIR), and differential scanning calorimetry (DSC), as

shown in Figure 6a-c for sample $S_{11k}L_{10k}$-55. Gravimetry shows that the weight

loss reaches 0.55, equal to the feeding ratio of PLA in the network, within ~ 1 d of

etching, and remains subsequently unchanged even after 16 d, suggesting that

the PLA component is removed quantitatively. Compared with the PS/PLA

networks (black lines), the complete disappearance of both the –C=O stretching

peak from the ester group in PLA (1751 cm^{-1}) from the FTIR spectrum (Figure 6b)

and the PLA glass transition at 38 °C from the DSC curves (Figure 6c) for PS porous monoliths (red lines) further support the complete removal of PLA.
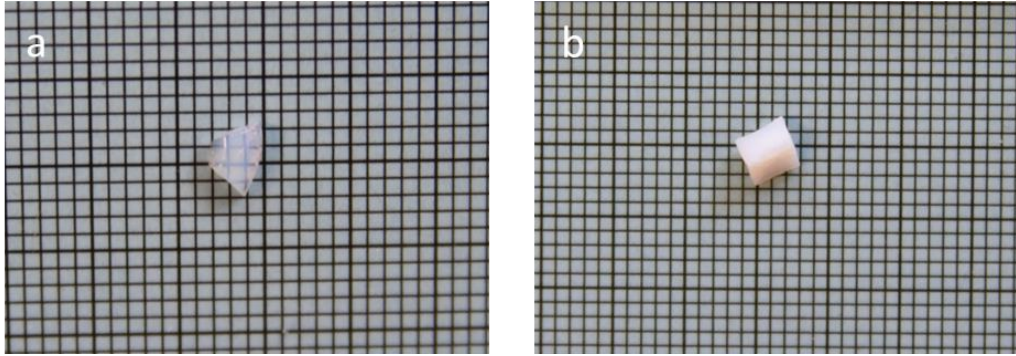
Figure 5. (a) A photograph of a PS/PLA RECN ($S_{11k}L_{10k} - 55$) showing slight cloudiness likely due to the trapped concentration fluctuations. (b) A photograph of a porous PS monolith prepared by etching a PS/PLA RECN ($S_{11k}L_{10k} - 55$)
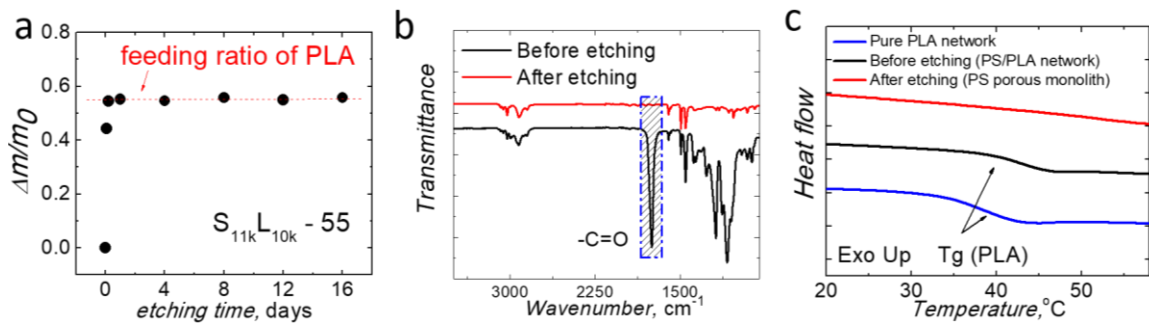
Figure 6. Characterization of sample S11kL10k-55. (a) Weight loss against time when immersed in a 2 M solution of NaOH in water/methanol (6/4, v/v); (b) Fourier transform infrared spectroscopy (FTIR) measurements before (black) and after (red) etching; (c) differential scanning calorimetry (DSC) measurements of $S_{11k}L_{10k}$-55 before (black) and after (red) etching, and pure PLA network (blue).

The structures of the network are investigated by small-angle X-ray scattering (SAXS). As seen in Figure 7a, $S_{11k}L_{10k}$-55 shows a clear and broad scattering peak at $q^* = 0.20$ nm^{-1}, corresponding to d-spacing = $2\pi/q^* = 31$ nm, consistent with a disordered microphase separated structure. Specifically, the d-spacing we are referring here and in the following chapters is the average characteristic length corresponding to the primary scattering peak in SAXS. As for a disordered morphology, it is a somewhat ambiguous to correlate the-real

space domain size to scattering characteristic length, due to the irregular structures and broad distribution of domain size. In fact, in this thesis we are going to use TEM tomogram to better understand how is the average domain thickness related to d-spacing (see details on Page 20). Notably, similar SAXS patterns are obtained when samples are prepared under different conditions (*i.e.*, with the network formed at an elevated temperature to increase the end-linking kinetics, or as a thin film to increase the rate of solvent evaporation), suggesting that this method is not highly sensitive to the kinetics of reaction or solvent evaporation, as shown in Figure 8.
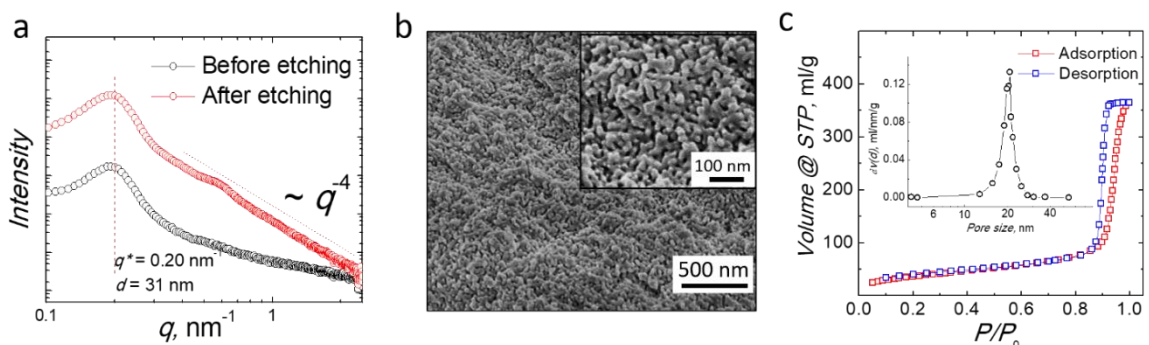
Figure 7. (a) small-angle X-ray scattering (SAXS) characterization before (black) and after (red) etching; (b) scanning electron microscope (SEM) characterization, 1 nm of Au was coated before imaging; (c) Nitrogen adsorption isotherm at 77.3 K.

After extracting PLA phases, the corresponding porous monolith exhibits a scattering peak with the same shape and *d*-spacing, suggesting that the characteristic structure has not changed; however, the scattering intensity is increased due to the greater contrast in electron density between PS and vacuum, compared to that between PS and PLA. This increased contrast also makes it possible to detect a weak higher order peak centered at 0.60 nm^{-1}, corresponding to $3q^*$. The presence of such weak secondary reflections has also

been noted in many other disordered co-continuous structures[58,66–69], including from similar end-linked networks.[47] Although the origin of these higher order peaks is still not fully understood, within late stage spinodal structures they have been interpreted in terms of the structure factor defined by locally ordered regions,[67,68] or as a signature of the negative Gaussian curvature interfaces.[69] In the high q region, the intensity decrease corresponding to q^{-4} for porous monoliths, indicating the sharp interfaces between PS matrix and pores.[67]. Interestingly, the porous material is also soluble in THF, indicating that degradation of PLA is sufficient in this case to reduce the crosslink density below the gel point. Unfortunately, as the current materials are composed of modest molecular weight polystyrene, they are fairly brittle, making it difficult to determine their mechanical properties.
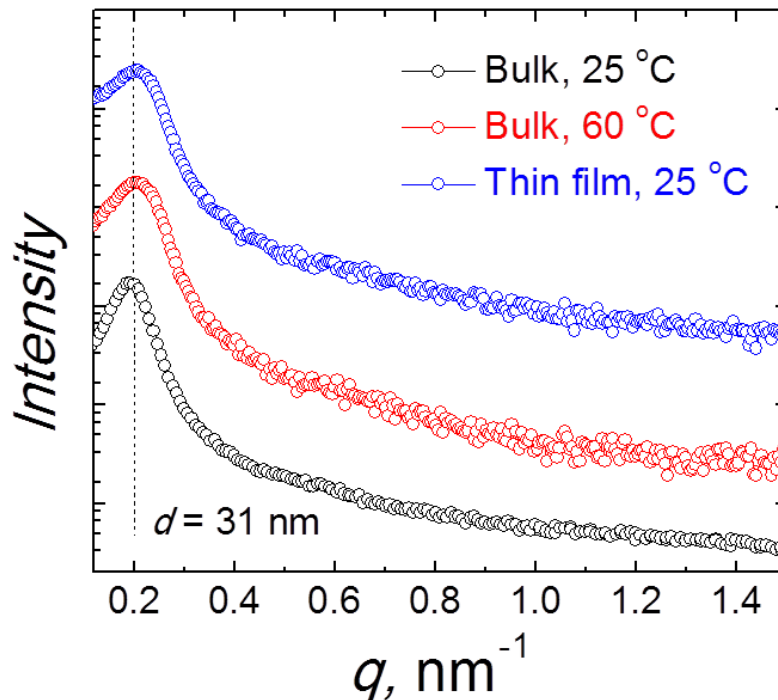
Figure 8. SAXS patterns of $S_{11k}L_{10k}$ – 55 samples prepared under different conditions: a bulk monolithic sample of ~ 5 mm dimensions end-linked at 25 ^{o}C

(black), corresponding to the conditions used elsewhere in the manuscript, a bulk monolithic sample end-linked at 60 °C (red), which yields a roughly 8-fold increase in the rate of end-linking based on an activation energy of ~ 50 kJ/mol for formation of urethane linkages,[1] and a sample end-linked at 25 °C and prepared as a ~ 0.5 mm thick film (blue), which is expected to increase the rate of solvent evaporation by ~ 100-fold, assuming that mass transport is diffusion limited (but at least ~ 10-fold, even in the case of a desorption-limited process). All three samples show similar scattering patterns with nearly identical peak locations, indicating that the structure is not highly sensitive to kinetics effects.

The pore size distribution is next studied by a nitrogen adsorption isotherm measurement, as shown in Figure 7c. Based on Barrett-Joyner-Halenda (BJH)[70] analysis, the average pore size is 20 nm. The pore volume is calculated to be 0.55 cm^3/g by the nitrogen uptake at P/P_0 = 0.95, which is somewhat smaller than the ideal value of 0.98 cm^3/g based on respective densities for PS and PLA of 1.05 cm^3/g and 1.25 cm^3/g. We suspect that this difference reflects the collapse of micropores within the PS walls generated by etching of PLA chains 'trapped' within the PS phase, or perhaps the influences of cracks in the monolith formed during solvent evaporation. The surface area is calculated by Brunauer-Emmett-Teller (BET) analysis[71] to be 134 m^2/g, comparable to other porous materials with similar pore size and porosity.[72] The morphology of the porous monolith is further characterized by scanning electron microscopy (SEM), as shown in Figure 7b. The PS phase is clearly well percolated, but is penetrated by an interconnected and disordered network of pores, with a characteristic spacing of ~ 30 nm, in agreement with the SAXS measurement.
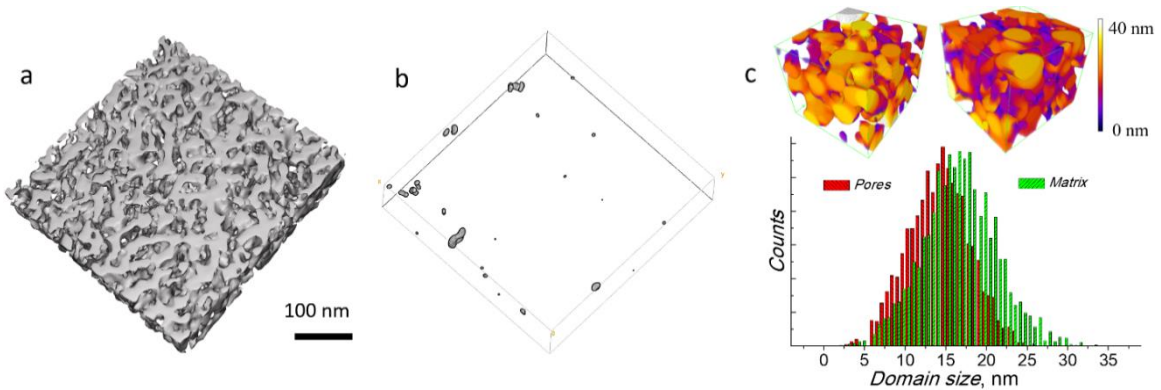
Figure 9. (a) TEM tomographic reconstruction of the porous sample with the PS matrix shown in dark colors. (b) The same reconstruction following 3D flood filling of interconnected pores, with the unfilled (disconnected porous) portions shown in dark colors. (c) Size distributions of pore (left image and red bars) and matrix (right image and green bars) domains calculated by finding the diameter of the largest sphere that fits within the respective domain at each point in the tomogram.

Transmission electron microscope (TEM) tomography is used to provide a more detailed characterization of the nanoporous structure, as shown in Figure 9a. In performing the reconstruction, the threshold between pores (bright) and PS walls (dark) is chosen to match the porosity measured by N_2 adsorption. The tomogram reveals a disordered morphology with a well-defined length scale similar to 30 nm, and a high degree of interconnectivity between both PS and porous phases. By applying 3D flood filling analysis, we identify that less than 0.5 % by volume of the pores are not connected to the percolating porous region within the reconstruction volume, as shown in Figure 9b. Since these regions are located almost exclusively along the boundaries, it is likely that they are indeed connected to the percolating pore network through connections outside of the reconstruction volume. The complete removal of the PLA phase and the interconnecting pore structure, along with the PS phase maintaining its structural integrity, clearly indicates that this randomly end-linked network is co-continuous

with both phases percolating in 3D. As seen in Figure 9c, we further characterize the distribution of domain sizes from the tomogram by calculating the diameter of the largest sphere at each point that fits completely within the domain and contains the point.[65] From this analysis, the average sizes of pore and matrix phases are determined to be 13.5 and 16.8 nm, respectively. Interestingly, the total average domain thickness (30 nm) is in good agreement with d-spacing (31 nm) characterized from SAXS, suggesting that the domain thickness obtained from sphere fitting at some level captures the characteristic length measured by scattering.

2.3.2 Wide Co-continuous Window

To determine the composition window over which co-continuous structures can be formed in PS-PLA RECNs, we consider $S_{11k}L_{10k}$ networks prepared using a variety of composition, expressed in terms of the weight fraction of the constituent polymers. As seen in Figure 11a, ω_{PLA} is varied from 0.31 to 0.85, corresponding to volume fractions φ_{PLA} of 0.27 to 0.83. SAXS measurements reveal a similar scattering pattern in all cases, i.e., a broad scattering peak with a d-spacing of 30 - 31 nm (Figure 10), indicating disordered microphase separated morphologies over the full range of composition. Unfortunately, these scattering patterns do not provide any clear evidence as to the co-continuity of the samples.
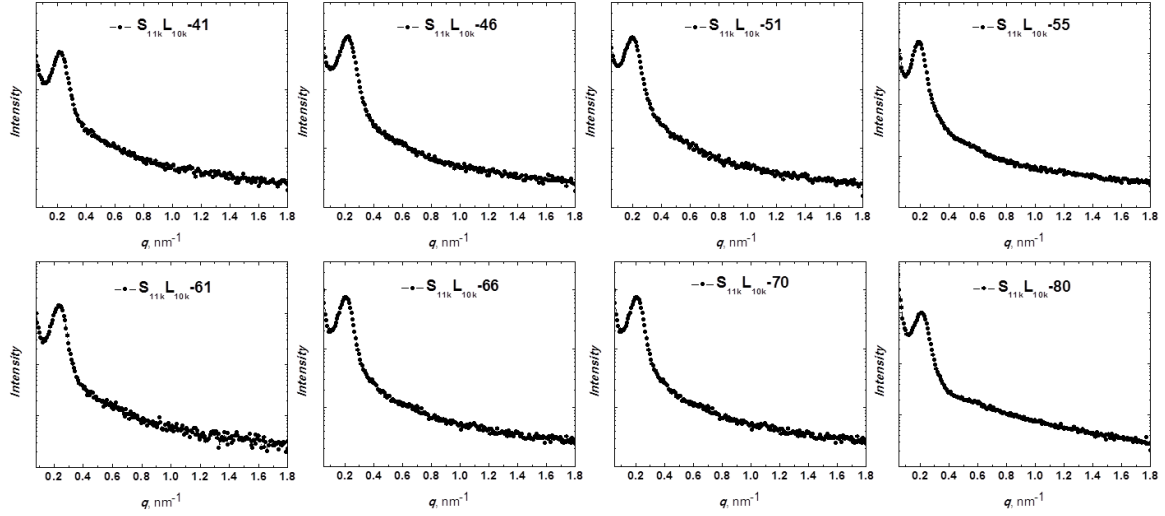
Figure 10. SAXS patterns for samples of $S_{11k}L_{10k}$ with different compositions.
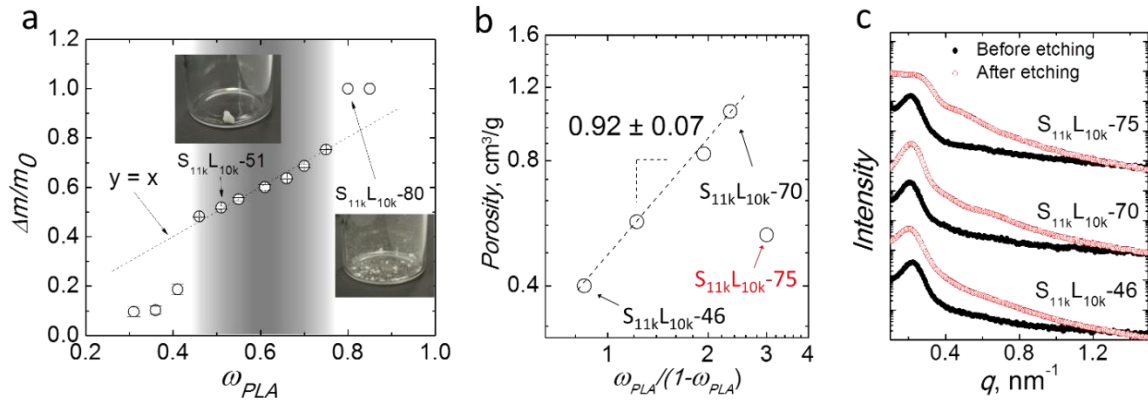
Figure 11. (a) Gravimetric results of $S_{11k}L_{10k}$ samples. Images are taken for sample $S_{11k}L_{10k}$-51 and $S_{11k}L_{10k}$-80 after PLA are etched; (b) Porosities calculated from N_2 adsorption isotherm measurements for samples prepared from $S_{11k}L_{10k}$ networks with different compositions. Increasing the PLA content ω_{PLA} = 0.46 to 0.70 yields a linear increase in porosity from 0.40 cm^3/g to 1.05 cm^3/g as a function of ω_{PLA}/(1 - ω_{PLA}), indicating that the monoliths have similar interconnected pore structures, while the lower porosity at ω_{PLA} = 0.75 suggests partial pore collapse. (c) SAXS characterization of $S_{11k}L_{10k}$-46, $S_{11k}L_{10k}$-70 and $S_{11k}L_{10k}$-75.

Thus, we instead turn to a combination of gravimetry, porosimetry, FTIR, and SAXS measurements to unambiguously determine percolation of both phases. The gravimetric data, plotted as the mass loss after etching Δm normalized by the initial sample mass m_0, *vs.* the initial loading of PLA ω_{PLA},

exhibit three distinct regions, as shown in Figure 11a. When $\omega_{PLA} \leq 0.41$, values of $\Delta m/m_0$ points fall well below the line of $y = x$, indicating that PLA is only partially etched, and revealing the presence of isolated PLA domains embedded within the PS matrix that are not part of a percolating network, and therefore inaccessible to the basic solution. Surprisingly, ~ 10 wt% of the samples ($w_{PLA} = 0.30$ and 0.35) can still be extracted in this non-percolating regime, presumably due to cracking of the monolith that provides access to PLA domains neighboring these surfaces. Above $\omega_{PLA} = 0.41$, however, the fraction of PLA extracted increases rapidly with increasing PLA content, corresponding to the percolation of PLA domains. When $0.46 \leq \omega_{PLA} \leq 0.70$ ($0.42 \leq \varphi_{PLA} \leq 0.66$), the values $\Delta m/m_0$ fall upon the line $y = x$, representing essentially quantitative removal of PLA, and indicating that both PS and PLA are fully percolating, allowing complete accessibility of base to the PLA phase, while all portions of the PS phase remain part of a single monolith following etching. For all samples in this region, the consistency of SAXS patterns before and after etching, as shown in Figure 11c for $S_{11k}L_{10k}$-46 and $S_{11k}L_{10k}$-70, also indicates that PS domains are highly percolated, providing mechanical integrity. In Figure 12, FTIR and SEM also support the complete removal of PLA and persistence of a fully interconnected structure.
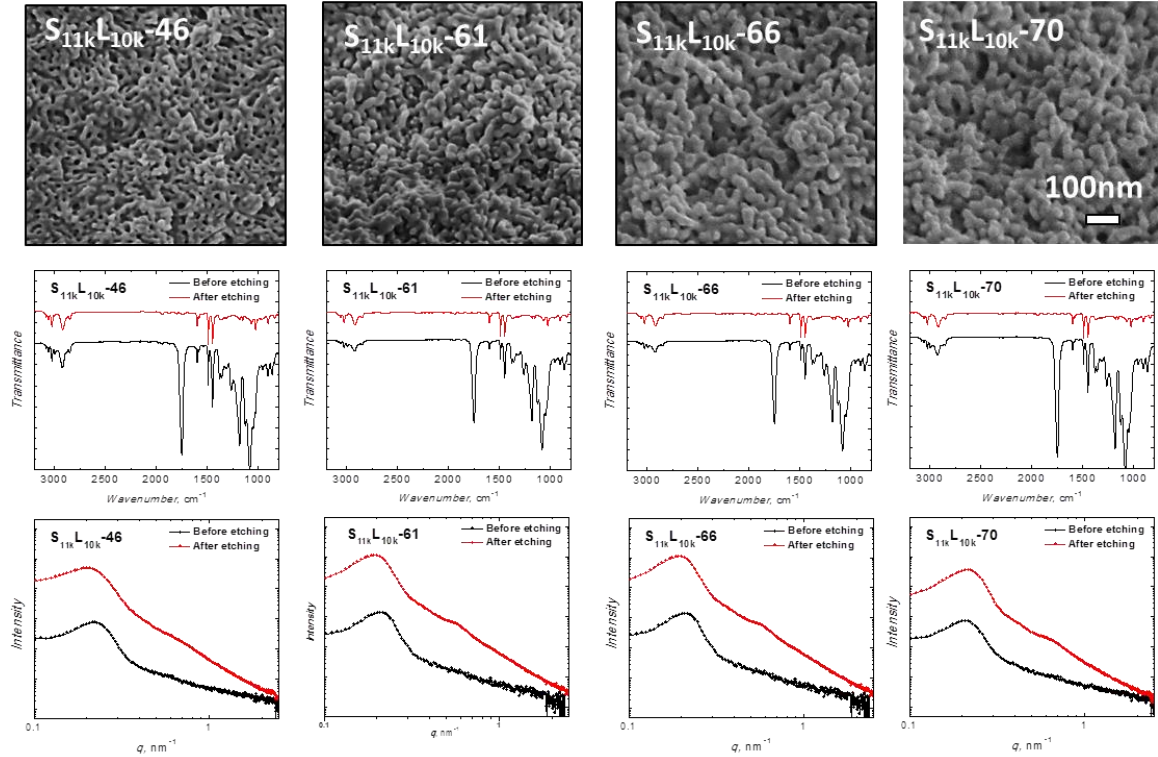
Figure 12. SEM (top row), FTIR (middle), and SAXS (bottom) data for co-continuous $S_{11k}L_{10k}$ samples.

In addition, N_2 adsorption measurements (Figure 11b) reveal that increasing the PLA content w_{PLA} = 0.46 to 0.70 yields a linear increase in porosity from 0.39 cm^3/g to 1.03 cm^3/g as a function of $\omega_{PLA}/(1 - \omega_{PLA})$, as expected for the materials with similar interconnected pore structures, further supporting that they have co-continuous morphologies with both percolating PS and PLA domains in this composition window. When the PLA content is further increased to ω_{PLA} > 0.75, the PS domains lose percolation, as evidenced by a second rapid increase in the value of $\Delta m/m_0$ to 1. After etching, samples in this region break up into small granules or even powders, as seen for $S_{11k}L_{10k}$-80 in Figure 11a, which we report as a normalized mass loss of 1. Notably, when ω_{PLA} = 0.75 (sample $S_{11k}L_{10k}$-75), though gravimetry appears to indicate a co-continuous

morphology, the SAXS pattern (Figure 11c) shows a broadening of the scattering peak and shift to larger q^* after extracting PLA domains, indicating that the nanostructure is not completely maintained upon etching. Presumably, this reflects either a partial pore collapse during solvent evaporation after etching, due to the low content of PS and tenuous percolation of these domains, or the physical attachment of isolated PS domains to the remaining percolating structure, due to the poor dispersibility of PS particles in the etching solution. We thus take this sample to be at the border between a co-continuous structure and one with dispersed PS domains. Taking all of these data together, we estimate the region for co-continuous structures as $\omega_{PLA} \approx 0.44 - 0.75$ ($\varphi_{PLA} \approx 0.40 - 0.72$), as denoted by the shaded gray region in Figure 11a. Notably, the width of the co-continuous region is similar to that of $\varphi_{PEO} \approx 0.30 - 0.65$ reported previously for PS-PEO RECNs.[47]

2.3.3 Well Controlled Pore Size
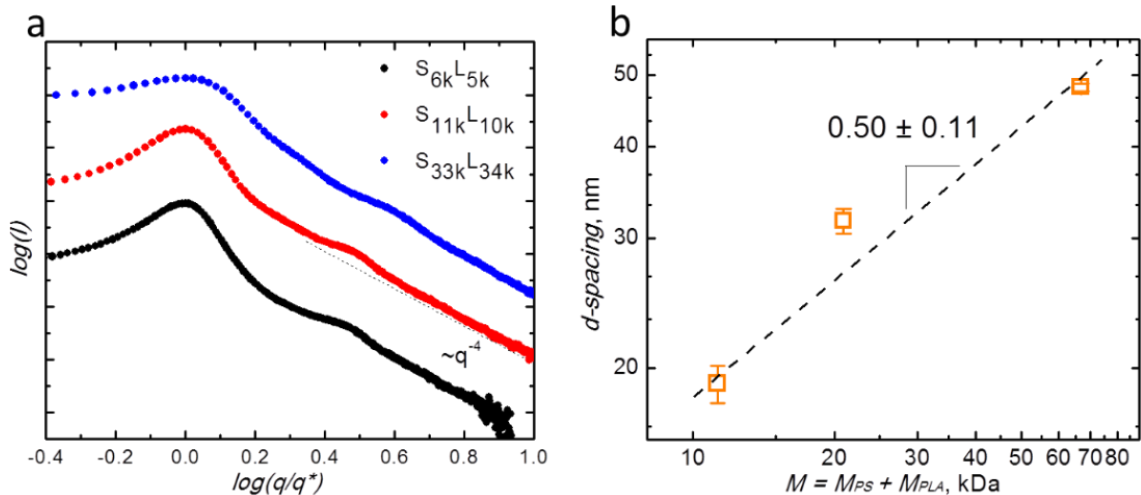
Figure 13. Dependence of RECN structure on strand molecular weight for nearly symmetric systems ($\varphi_{PLA} = 0.51$ and $M_{PS} \approx M_{PLA}$). (a) SAXS data for porous monoliths with different values of network strand molecular weight (black: 11 kDa;

red: 21 kDa; blue: 67 kDa); (b) The variation of d-spacing with M_n is consistent with the prediction $d \sim M_n^{0.5}$ by de Gennes.[38]

We then study the ability to control the characteristic size of inter-connected porous structures by adjusting the strand molecular weight for a series of nearly symmetric RECNs ($\varphi_{PLA} = 0.51$ and $M_{PS} \approx M_{PLA}$). As seen in Figure 13a, porous monoliths for each sample show a clear peak by SAXS, with no significant change in q^* or shape of the pattern upon removal of PLA domains, indicating a robustly percolating structure in each case. Meanwhile, $S_{6k}L_{5k}$ and $S_{11k}L_{10k}$ show nearly identical scattering patterns when normalized by q^*, indicating that the structures are quite similar. The normalized pattern for $S_{33k}L_{34k}$ shows a broader primary peak than the others. Although the origin of this difference requires further study, we speculate that it may reflect a more heterogeneous network structure due to the lower initial concentration of polymer in solution in this case (15 wt% for $S_{33k}L_{34k}$ vs. 30 wt% for $S_{6k}L_{5k}$ and $S_{11k}L_{10k}$), or perhaps a larger magnitude of trapped concentration fluctuations due to the higher molecular weights of the strands. However, as shown in Figure 13b, the variation in domain spacing ($d = 2\pi/q^*$) with M_n is, consistent with the dependence $d \sim M_n^{0.5}$ predicted by de Gennes[38] for randomly cross-linked copolymer networks approaching the microphase separation transition, and also previously reported for PS/PEO RECNs.[47] In all cases, the appearance of a higher-order peak ($3q^*$ for $S_{6k}L_{5k}$ and $S_{11k}L_{10k}$, but $2q^*$ and $4q^*$ for $S_{33k}L_{34k}$) and the intensity decrease corresponding to q^{-4} in the high q region for porous monoliths are consistent with a co-continuous morphology with sharp interfaces.[67]
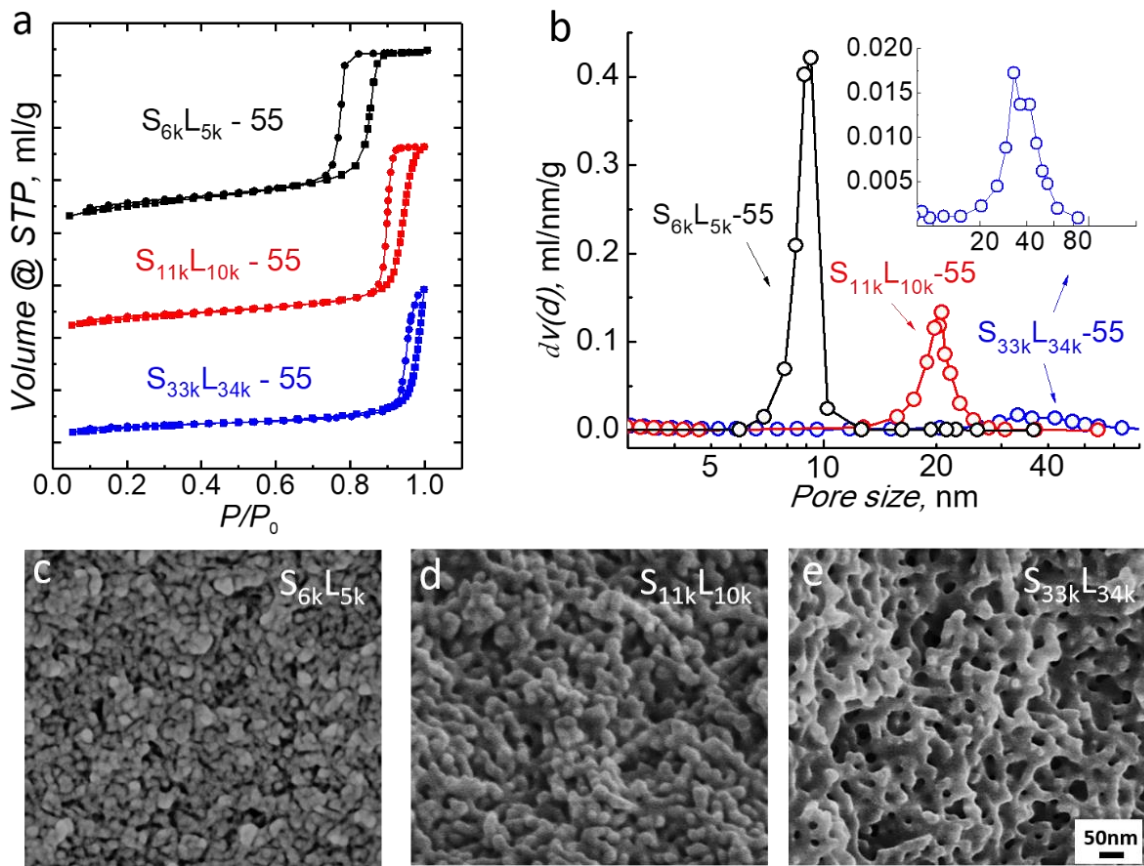
Figure 14. (a-b). N_2 adsorption isotherms and pore size distribution of symmetric RECNs with different M_n; $S_{6k}L_{5k}$ – 55 (black), $S_{11k}L_{10k}$ – 55 (red) and $S_{33k}L_{34k}$ – 55 (blue). c-e. SEM images of symmetric $S_{6k}L_{5k}$ (c), $S_{11k}L_{10k}$ (d) and $S_{33k}L_{34k}$ (e) after complete removal of PLA domains, showing an increase in pore size with increased M_n of the precursor polymers.

Further, N_2 adsorption isotherm measurements (Figure 14a-b) reveal well-controlled pore sizes varying from 9 to 34 nm with increasing M, with respective decreases in BET surface area from 191 to 102 m^2/g, and nearly constant porosities of ~ 0.55 cm^3/g. In Figure 14c-e, SEM images of porous monoliths also clearly show uniform pores with sizes that increase with M_n. Given the high χ between PS and PLA, we expect that further reductions in pore size to ≈ 7 nm should be possible with a reduction in strand molecular weight to ≈ 3 kg/mol (based on the predicted onset of microphase separation of symmetric randomly

crosslinked networks[73] at χN = 19.2). Further increases in pore size should also be possible, limited by the miscibility of high molecular weight polymers in the solvent, and the efficiency of the end linking chemistry used.

2.4 Conclusion

A robust route is developed to highly percolating and anisotropic porous materials from randomly end-linked copolymer networks. The presence of random crosslinks frustrates ordered structures, thereby providing a pathway to bicontinuous materials over a broad composition range spanning ~ 30 vol% in PLA content. After etching the degradable PLA component, monoliths are generated with narrowly-distributed pore sizes that can be tuned by varying the molecular weight of the network strands. With this PS/PLA model system, we have opened a simple means to generate nanoporous materials with well-controlled pore sizes and anisotropies. Although at this moment further practical application is limited by the brittleness of the porous PS materials obtained, other systems with better mechanical properties are likely to be accessible, given the generality of the method with respect to polymer chemistry, offering promise for a variety of applications, including filtration, insulation, and catalysis.

Chapter 3

EFFECTS OF RECNS PARAMETERS ON THE PHASE DIAGRAM

3.1 Introduction

Microphase separated copolymers with nano-scale morphologies are critically important in designing next generation materials.[74,75] Within various nanostructures, cocontinuous morphologies with domains of multiple different phases each simultaneously percolating in three dimensions, provide opportunities to synergistically combine properties of dissimilar constituent materials. For example, interconnected nanostructures throughout the materials are substantially useful in terms of mechanical robustness[7,8,11], mass transport[9,10], energy storage[76,77], and catalysis[13]. Amongst a wide variety of equilibrium[5,48,78] and kinetic routes[12,53,54,56] to achieve cocontinuous structures, recent work has established that randomly end-linked copolymer networks (RECNs) formed by crosslinking telechelic linear polymer chains with multifunctional cross-linkers are quite attractive in being able to not only preserve the well-defined network architectures, but also serve as a simple, robust and general method to fabricate cocontinuous nanostructure over a wide range composition window (spanning >30 vol %).[47,79] While maintaining cocontinuity, stretching RECNs introduces controlled orientation with substantial improvements in mechanical properties.[80] To date, a variety of previously reported binary RECNs, including polyethylene oxide (PEO)/polydimethylsiloxane (PDMS),[43,44] polyisobutylene (PIB)/PEO,[45] PS/PEO[47] and PS/poly(D,L - Lactide) (PLA),[79,80] self-organize into disordered cocontinuous morphologies

at a certain segregation strength close to the symmetric composition fraction. So far an incomplete understanding of phase separation behavior in RECNs has emerged from theory [38,40,73,81] and simulations[39,41,42,81] with few attempts at experimental confirmation[39]. For example, de Gennes has predicted a critical microphase separation transition (MST) occurring at $\chi N = 13.8$, where N corresponds to the total molecular weight of the two constitutive strands, while McLeish and co-workers predicted that the trapped concertation fluctuations should yield a higher critical MST at $\chi N = 19.2$. Although some guidance as to the expected phase separation behavior of RECNs is provided, no predictive direction exist for the design of nanostructures, especially cocontinuous morphologies in RECNs, like the well-studied phase diagrams for equilibrium self-assembly of flexible block copolymers.[14]

In this chapter we provide fundamental studies of self-assembly in binary PS/PLA RECNs as guidance for the design of cocontinuous nanostructures. Specifically, we rely on mechanical analysis below the glass transition temperature T_g of PS (95 °C) but above T_g of PLA (40 °C), and chemical degradability of PLA to unambiguously determine the percolation behavior of PS and PLA domains, respectively. Using PS/PLA RECNs as a model system, the first phase diagram of two-component symmetric ($N_{PS} \approx N_{PLA}$) RECNs is established. In the binary phase diagram of $\chi(N_{PS} + N_{PLA})$ vs. weight fraction (ω_{PLA}), we first experimentally observe the trapped concentration fluctuation and investigate the gradual transition of MST from phase mixed state to well phase separated structures. Additionally, we develop an understanding of how the

breadth and location of the cocontinuous region depends on network parameters, including strand molecular weight (M_n), strand length asymmetry and dispersity (Đ), and junction functionality (f). Domain spacing (d) dependence on M_n and volumetric content similar to BCP is also demonstrated in this report, while a very different d dependence on dispersity of is observed for RECNs, where d is dominated by the shorter chains within the high dispersity minority domain in contrast to that in BCP. These results provide a prospective study describing the morphology behavior in RECNs, enabling the robust design of cocontinuous structures with controlled length scales in a wide variety of polymer mixtures.

3.2 Results and Discussions

3.2.1 Bicontinuity Characterization

As described in our previous work,[80] we rely on thiol-Michael addition chemistry to form RECNs. Briefly, di-functional acrylate-terminated PS and PLA strands are homogeneously mixed in a non-selective solvent along with a tetra-thiol small molecule cross-linker, followed by end-linking reaction to generate well-controlled networks, as shown in Figure 15a. Solvent removal drives microphase separation into disordered nanostructures in RECNs with a well-defined characteristic length but no long-range ordering or orientation. We first consider the simplest case of symmetric RECNs with $M_{n, PS}$ (11 kg/mol) ≈ $M_{n, PLA}$ (10 kg/mol) after annealing at 150 °C for 24 h (χN = 30 at this temperature[62]), and understand how the morphology, especially the cocontinuous nanostructure, varies with volume fraction. Samples are named following the convention S$_{Mn,PS}$ L$_{Mn,PLA}$ − X, where the subscripts refer to the molecular weights of the respective

strands and X represents the percentage by weight of PLA, ω_{PLA}, prior to end-linking.
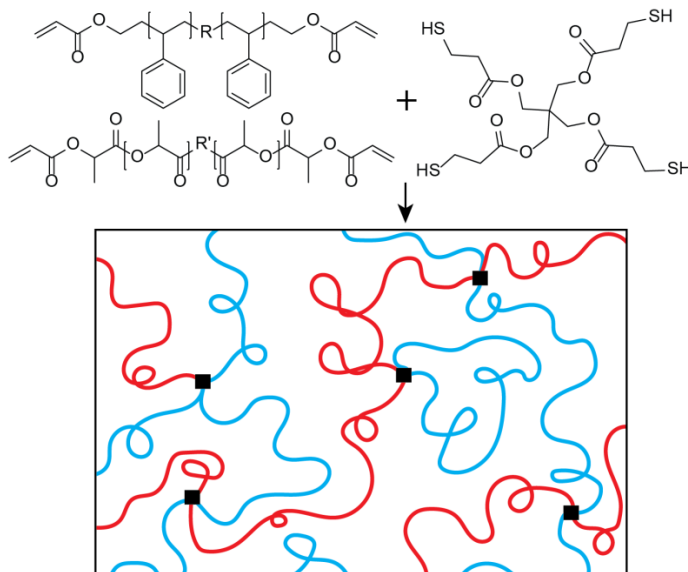
Figure 15. Preparation of randomly end-linked copolymer networks from telechelic PS and PLA.

		M_n (kg/mol) [1]	Đ [2]	f [1]
$S_{2k}L_{2k}$	PS	1.9	1.1	1.8
	PLA	2.0	1.2	1.9
$S_{3k}L_{3k}$	PS	3.4	1.1	1.8
	PLA	3.3	1.2	1.8
$S_{5k}L_{5k}$	PS	5.0	1.2	1.8
	PLA	5.4	1.2	1.8
$S_{11k}L_{10k}$	PS	11.0	1.1	1.8
	PLA	10.4	1.2	1.8
$S_{5k}L_{19k}$	PS	5.0	1.2	1.8
	PLA	19.4	1.2	1.9
$S_{11k}[L]_{10k}$	PS	11.0	1.1	1.8
	PLA	9.7	1.8	1.8

Table 1. A list of PS and PLA strands used to prepare RECNs. [1]Characterized by NMR. [2]Determined by GPC calibrated with PS standards.
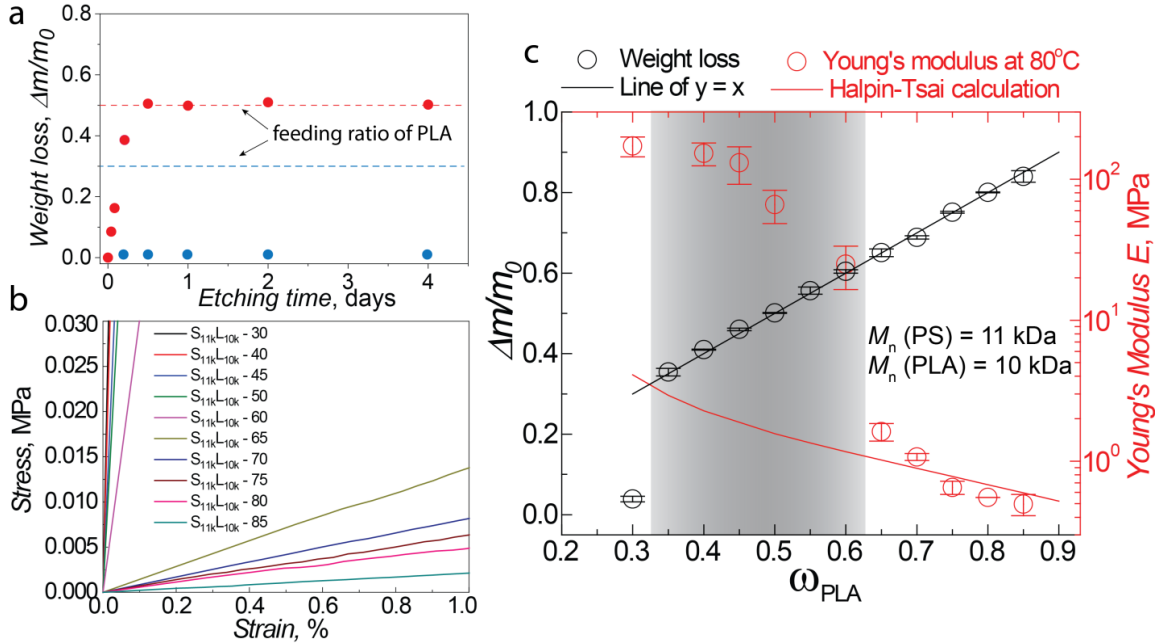
Figure 16. (a) Gravimetric analysis of PS/PLA RECNs to determine percolation behavior of PLA domains. (b) Stress – strain curves of tensile tests of $S_{11k}L_{10k}$ at 80 °C to verify PS domain percolation behavior. (c) Summary of gravimetry results (left and black) and modulus at 80 °C (right and red) of $S_{11k}L_{10k}$ with shaded area denoting cocontinuous window where both PS and PLA domain form independent interconnected channels. Black and red line referring to line y = x and Halpin-Tsai calculation.

To assess whether the morphology is cocontinuous, we use mechanical analysis below T_g of PS (95 °C) but above T_g of PLA (40 °C) to unambiguously determine the percolation of PS, and chemical degradability to probe the percolation of PLA. For example, Figure 16a shows the gravimetric results of sample $S_{11k}L_{10k}$ – 30 and 50 placed in 1 M solution of NaOH in water/methanol (6/4, v/v) at room temperature to etch the PLA domains. Around 12 h, weight loss ($\Delta m/m_0$) of $S_{11k}L_{10k}$ – 50 reaches the feeding fraction (ω_{PLA} = 0.5) of PLA in the networks, and remains unchanged with longer etching time, indicating quantitative removal of fully percolated PLA domains in the networks; however, weight loss of $S_{11k}L_{10k}$ – 30 is always far below ω_{PLA}, suggesting isolated PLA

domains surrounded by PS domains, preventing alkaline solution from accessing the PLA domain. Therefore, when plotting weights loss $\Delta m/m_0$ against ω_{PLA} in Figure 16c, we are able to determine the PLA percolation threshold as $\omega_{PLA} \approx$ 0.32, above which PLA domains form interconnected nanostructures and gravimetric data points falls upon the black line of y = x. To examine the percolation of PS domain, Figure 16b shows the uniaxial tensile tests of $S_{11k}L_{10k}$ at 80 $^{\circ}$C, from which elastic modulus is extracted as a function of ω_{PLA}. Unsurprisingly, the modulus decreases as ω_{PLA} increases, due to the decrease of glassy domain and increase of rubbery PLA domain. Moreover, the change of glassy PS domain from percolated to un-percolated nanostructures will accompany a sharp modulus decrease. In Figure 16c, when plotting elastic modulus E against ω_{PLA}, a sharp drop is indeed observed with the increase ω_{PLA}. To further evaluate the percolation threshold of PS domains, we compare the measured E to the calculated E of PS/PLA composites using the empirical Halpin–Tsai equation[82] by assuming isolated and glassy PS particles/fibers, and/or in other shapes embedded in a rubbery PLA matrix. Noticeably, the calculated values agree very well with measured results when $\omega_{PLA} \geq 0.65$ as shown in Figure 16c, while obvious deviation (the measured E exceeds the Halpin-Tsai calculation by 2 times) is observed when $\omega_{PLA} \leq 0.6$, due to the failed assumption of isolated PS domain. We then identify the point $\omega_{PLA} \approx 0.62$ as the threshold that PS domains start to form percolated structures throughout the materials. Notably, there is a fundamental difference between structural percolation of PLA domain and rigidity percolation of PS domain, and the

thresholds of which represent the composition fractions where PLA forms fully percolated structures and PS starts to form interconnected rigid channels, respectively. This difference may also explain the gradual percolation behavior for PS domains, as the rigidity is more sensitive to composition fraction.
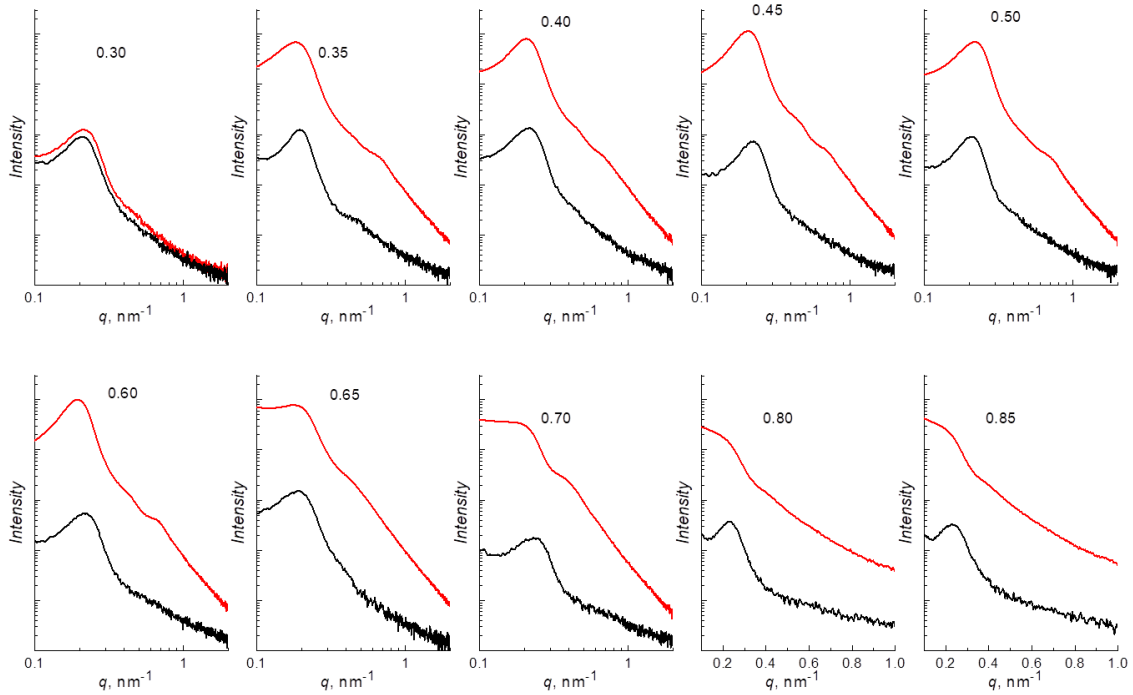
Figure 17. SAXS spectrums of $S_{11k}L_{10k}$, with numbers denoting weight fraction of PLA. Black: before etching. Red: after etching.

Additional confirmation of these percolation thresholds is provided by the comparison of small angle X-ray scattering (SAXS) before and after extracting PLA domain, as seen in Figure 17. When $\omega_{PLA} = 0.30$, almost no changes (both intensity and shapes) in the SAXS spectrums is observed, suggesting isolated PLA domains; when $0.35 \leq \omega_{PLA} \leq 0.60$, the maintained spectrum shape and two orders of magnitude increase of scattering intensity reveal the complete removal of PLA domains and preserved PS structures as a fact of cocontinuous nanostructures; when $\omega_{PLA} \geq 0.65$, broadening of the scattering peak and shifting

to larger q^* after extracting PLA domains indicate the collapsed porous structures, most likely due to the un-percolated PS domain.
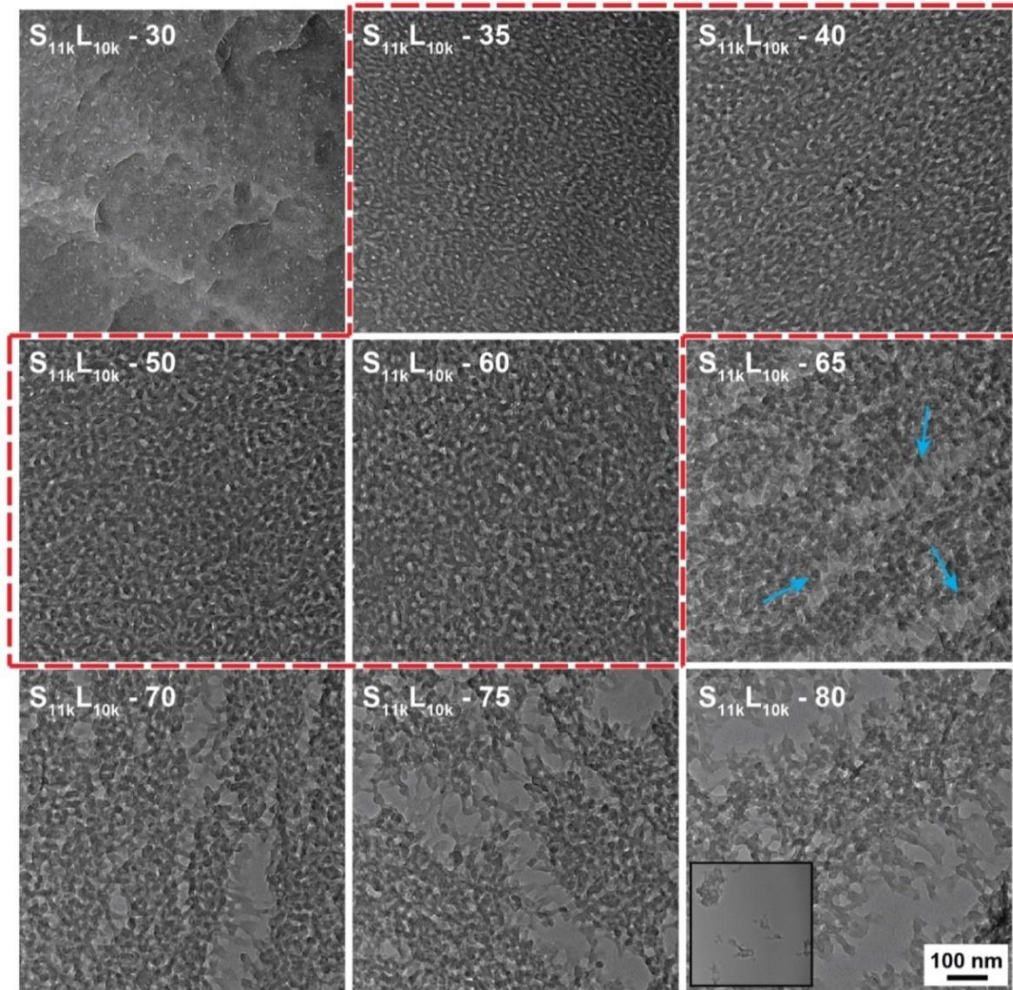
Figure 18. TEM images of porous PS by selectively removing PLA domains within PS/PLA RECNs $S_{11k}L_{10k}$ with different PLA weight fractions. Dashed red line denotes cocontinuous samples.

To better visualize the nanostructures and understand the percolation behavior of $S_{11k}L_{10k}$, transmission electron microscopy (TEM) images after PLA domain extraction are then used, as shown in Figure 18. In good agreement with gravimetric analysis, $S_{11k}L_{10k} - 30$ shows isolated porous domains (white parts), the volume fraction of which appears to be much lower than the feeding ratio of PLA ($\varphi_{PLA} = 0.26$), suggesting that most of the PLA domains are surrounded or

protected by PS domains. Indeed, gravimetry result reveals that only less than 10% PLA domains within the networks are accessible to alkaline solution. Within the wide cocontinuous window we identified before, ω_{PLA} = 0.32 − 0.62, extracting PLA domains generates interconnected nanoporous materials with curved interfaces. Beyond ω_{PLA} ≥ 0.65, the un-percolated PS matrix is not able to preserve its nanostructures after removing PLA domains, resulting in collapsed porous structures, as blue arrows denote in $S_{11k}L_{10k}$ − 65, although we do not observe macroscopic material failure maybe due to the physical attachment of isolated PS domains. Further supported by these TEM images, the cocontinuous window for $S_{11k}L_{10k}$ is characterized to span over 30 vol %, as both noted in the shaded area of Figure 16d and dashed lines in Figure 18.

3.2.2 RECNs Phase Diagram

As a straightforward comparison to diblock copolymers, we next consider how segregation strength χN ($N = N_{PS} + N_{PLA}$) of PS/PLA RECNs affects microphase separation and the morphology by tuning molecular weight of nearly symmetric RECNs ($M_{PS} \approx M_{PLA}$). As seen in Figure 19a, a series of $S_{5k}L_{5k}$ (χN = 15) with a variety of compositions expressed in ω_{PLA} are prepared in the same condition as $S_{11k}L_{10k}$, and gravimetry and mechanical tests show cocontinuous window spanning over 30 vol % (shaded area), with the percolation threshold for PS in the range 0.30 − 0.35, and that for PLA in the range 0.60 − 0.65. Comparing $S_{5k}L_{5k}$ and $S_{11k}L_{10k}$, we find a weak dependence of percolation behavior of symmetric RECNs on strand molecular weight.. Indeed, normalized SAXS curves of $S_{5k}L_{5k}$ − 50 (red) and $S_{11k}L_{10k}$ − 50 (green) in Figure 19b show

nearly identical shapes with a broad primary scattering peak but not higher order peaks, reflecting similar disordered nanostructures with a molecular weight dependent characteristic length $d = 2\pi/q^*$. Heating $S_{5k}L_{5k}$ up to 200 °C reduces χN to 12, but does not yield obvious changes in the SAXS curves, indicating negligible changes in nanostructure, as shown in Figure 20. Noticeably, $S_{2k}L_{2k}$ – 50 (black curve in Figure 19b) with further decreased segregation strength (χN = 6) shows a significantly weaker and broader peak, suggesting some level of weak concentration fluctuation. Gravimetric result of $S_{2k}L_{2k}$ – 50 with less than 1% weight loss indicates no evidence of distinctive microphase separated PLA domains which would be accessible to alkaline solution, thus we categorize this sample in the phase mixed region.
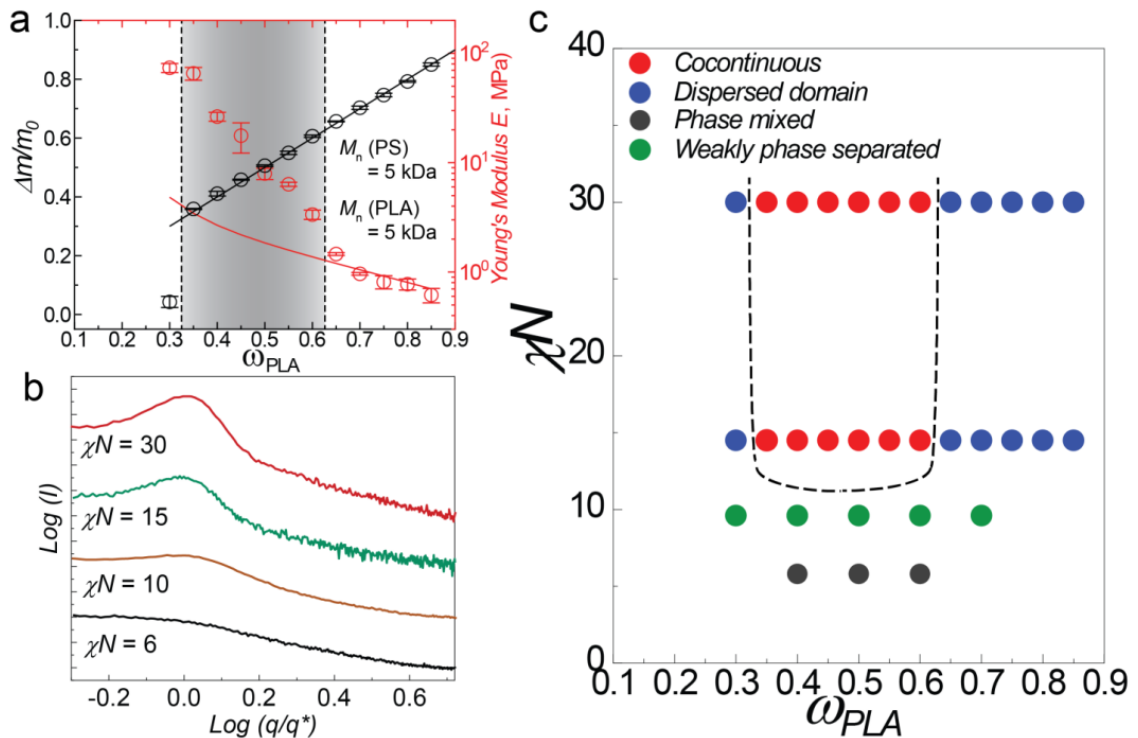
Figure 19. (a) Summary of gravimetry results and modulus at 80 °C of $S_{5k}L_{5k}$ with shaded area and dashed line denoting cocontinuous window of $S_{5k}L_{5k}$ and $S_{11k}L_{10k}$. (b) SAXS data (vertically shifted for clarity) of RECNs ω_{PLA} = 0.5 with

different network strand molecular weight $M = M_{n,\,PS} + M_{n,\,PLA}$ (black: 4 kDa; red: 10 kDa; green: 21 kDa), therefore different segregation strength $\chi N = 6, 15, 30$, respectively. (c) Phase diagram of RECNs with symmetric strand length ($M_{PS} \approx M_{PLA}$). Open circles denote $S_{5k}L_{5k}$ samples at 200 °C.
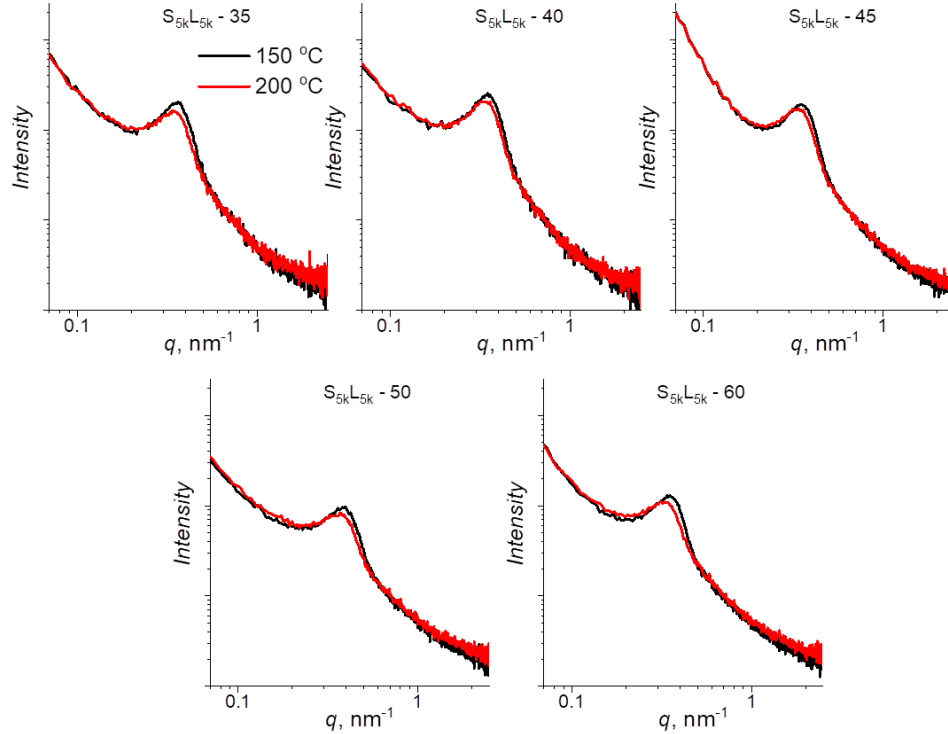
Figure 20. SAXS results for samples of $S_{5k}L_{5k}$ at 150 and 200 °C.

Interestingly in Figure 19b, we look closer to the critical MST by preparing $S_{3k}L_{3k} - 50$ with segregation strength $\chi N = 10$, and find the scattering profile of this sample also shows a weak and broad peak, although slightly stronger than that of $S_{2k}L_{2k} - 50$. While quantitative removal of PLA seems to suggest the existence of phase separated domains, the dramatically changed scattering profile (Figure 21) indicates unpreserved PS structures, due to pore collapse or weakly phase separated nanostructures. Indeed, we think this weakly phase separated nanostructure may correspond to trapped concentration fluctuations, and it is further confirmed by the single T_g observed both in differential scanning calorimetry (DSC) and dynamic mechanical analysis (DMA), as seen in Figure 22.

Theoretically, de Gennes calculated a critical MST occurring at $\chi N = 13.8$, while McLeish and co-workers predicted that the trapped concertation fluctuations in crosslinked networks would increase the critical MST to $\chi N = 19.2$. Our experiments show a critical MST, $6 < (\chi N)_{critical} < 12$, smaller than predicated values, maybe due to the defects (loops or dangling chains) in RECNs or non-monodispersed strands. We now summarize the phase diagram of symmetric RECNs in Figure 19c. As the segregation strength is increased, the structure adopted by RECNs gradually evolves from phase mixed state with slight concentration fluctuation to weakly phase separated region, and finally to well phase separated region. In the well phase separated region, disordered cocontinuous nanostructures occupy the center of the phase diagram, which does not have a strong dependence on segregation strength and spans from $\omega_{PLA} = 0.32$ to 0.62. On the left and right, there are morphologies with dispersed PLA and PS domains residing the sides.
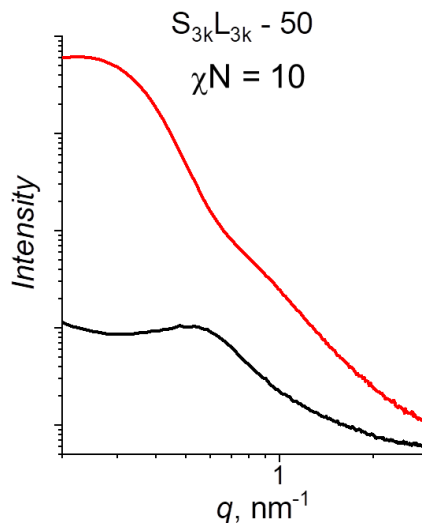
Figure 21. SAXS results for samples of $S_{3k}L_{3k}$ – 50 before and after removal of PLA domains. The dramatically changed scattering profile after removing PLA domains suggests changed PS matrix structures.
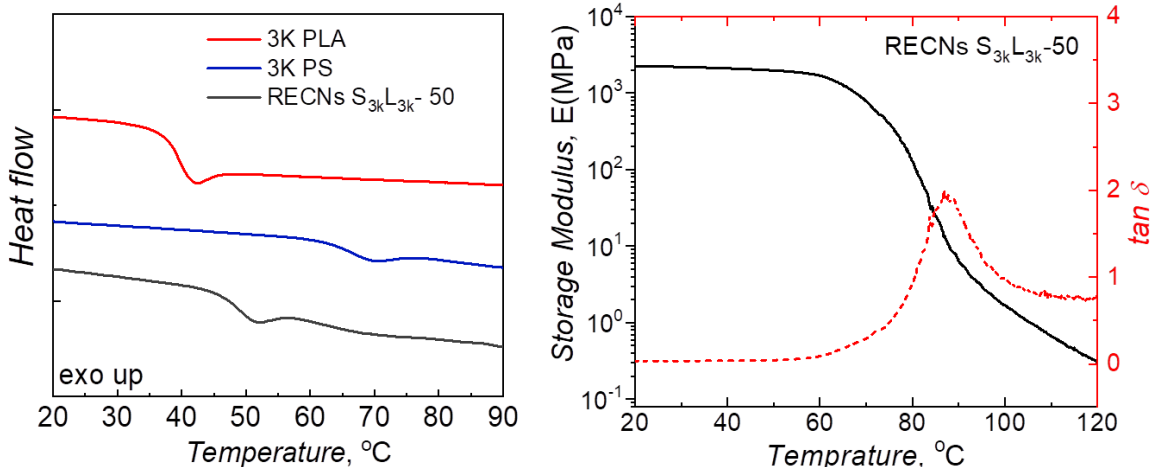
Figure 22. DSC and DMA results for samples of $S_{3k}L_{3k} - 50$. While SAXS of $S_{3k}L_{3k} - 50$ (Figure 21) indicates some scattering contrast, both DSC and DMA show a single glass transition, indicating trapped and weak concentration fluctuation.

3.2.2 Molecular Weight Asymmetry

Next, we study how the RECNs phase diagram depends on strand length asymmetry by preparing a series of $S_{5k}L_{19k}$ ($M_{n, PS} << M_{n, PLA}$), representing nearly the same segregation strength as $S_{11k}L_{10k}$, based on the sum of the two strand lengths. Surprisingly, Figure 23a shows that the asymmetric system maintains a broad co-continuous window, but there is essentially no shift in the boundaries, similar to the observation of McLeod and Tew for PS/PEO RECNs.[83] This runs counter to the behavior of miktoarm star copolymers that the boundaries would shift towards lower contents of the shorter (PS) block, because a larger number of shorter blocks prefer to occupy more interfacial area than fewer longer blocks that occupy the same volume.[84–86] Although we do not fully understand the origin of the difference between RECNs and star copolymers, we speculate one explanation as that the stretching of strands in RECNs requires greater elastic energy penalty, which does not vary much with strand asymmetry. Also in

RECNs, the existence of crosslinkers with 4 PS arms reduces the number of 3 PS : 1 PLA junctions at the interface, leading to the reverse effect of boundary shifting (see below for more details). More interestingly, Figure 23b shows that the overall d spacing of $S_{5k}L_{19k}$ decreases with the increase of mass fraction ω_{PLA} (the longer strands), indicating that the characteristic length of RECNs is more sensitive to the strand length of the minority domains. Given the high elastic stretching penalty in RECNs, the strands in the majority domains are more easily able to adjust their conformation to adopt the preferred spacing set by the minority domains. Indeed, this observation is consistent with diblock copolymers, which has decreasing d spacing as moving away from the equal volume fraction for a constant $N = N_A + N_B$.[87]
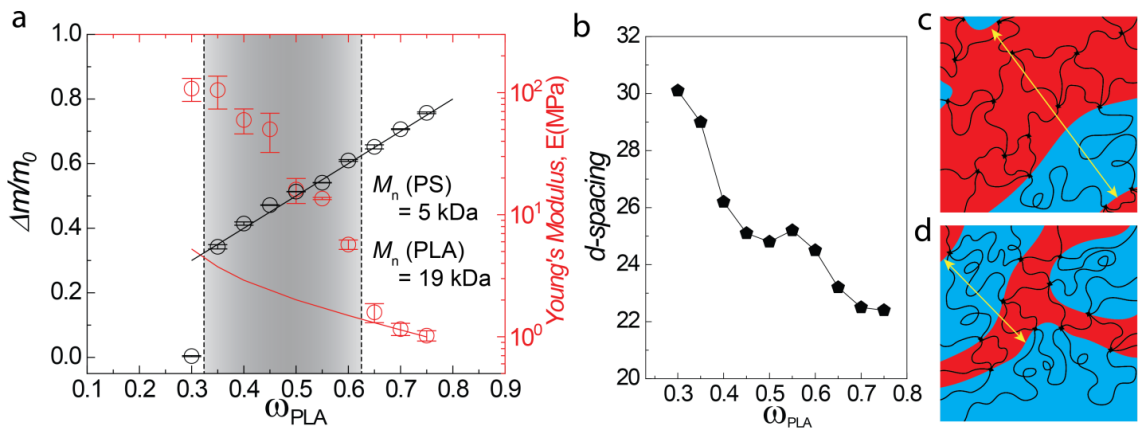
Figure 23. (a) Summary of gravimetry results and modulus at 80 °C of asymmetric RECNs $S_{5k}L_{19k}$ with shaded area denoting cocontinuous window and dashed line referring to cocontinuous window of $S_{11k}L_{10k}$. (b) Domain spacing of $S_{5k}L_{19k}$ vs. PLA weight fraction. Schematic depiction of domain spacings with longer PLA chain (c) and shorter PS chain (d) as the minority phase within $S_{5k}L_{19k}$.

Moreover, as shown in Figure 23c, when the shorter PS strands are the majority domain (towards the left side of Figure 23b), the number of PS strands exceed those of the minority longer PLA strands by 10 times, therefore resulting

in roughly 60% of crosslinkers having 4 PS arms, which tend to embed into and swell the PS domains, leading to a larger overall d spacing, compared to the case when PLA is the majority phase (towards to the right side of Figure 23b). Additionally, when we consider that a large fraction of 4 PS junctions buried within PS phase, it means that at the interface fewer number of 3 PS : 1 PLA junctions (and larger number of 2 PS : 2 PLA or even 1 PS : 3 PLA junctions) should be expected, which further explains our observation for RECNs that molecular weight asymmetry does not noticeably shift the percolation thresholds.

3.2.3 Strands Length Dispersity

We also investigate the effect of strand molecular weight dispersity Đ by mixing low M_n and high M_n PLA to achieve Đ = 1.8 (compared to Đ = 1.2, previously in $S_{11k}L_{10k}$) while keeping the value of M_n unchanged at 10 kg/mol, as shown in the GPC traces in Figure 24a. A series of $S_{11k}[L]_{10k}$ with [] referring to bimodal dispersed strands are prepared and characterized using gravimetry and mechanical tests. In comparison to cocontinuous window (ω_{PLA} = 0.32 − 0.62, shown as the shaded area) of $S_{11k}L_{10k}$, Figure 24b demonstrates that increase of PLA dispersity both widens the co-continuous window and shifts it towards larger PLA mass fraction. This can be understood from the behavior of linear block copolymers, where greater dispersity is known to both promote cocontinuity[88–90] and also favor the location of the high dispersity block on the inward side of curved interfaces[88,89,91–93], due to the tendency for increased dispersity in length of the minority domains to relieve packing frustration.
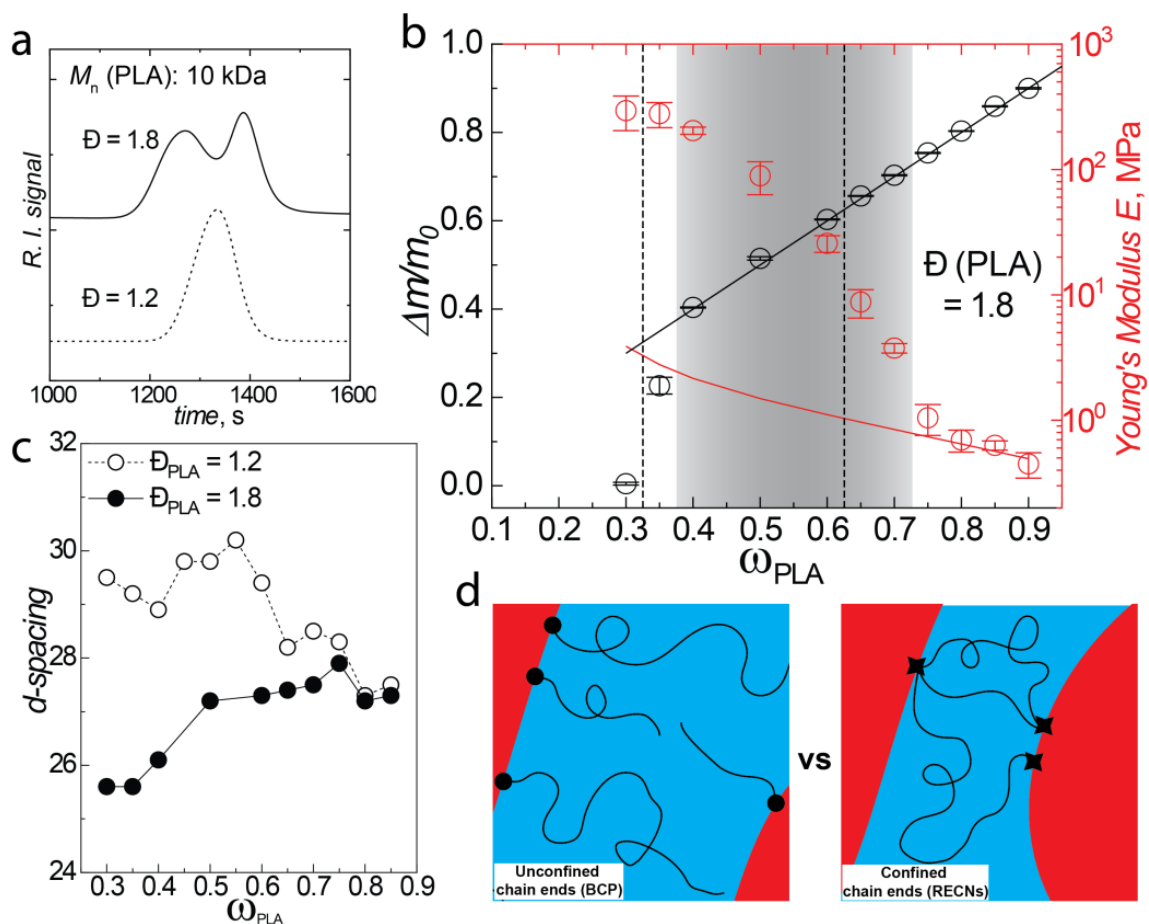
Figure 24. (a) GPC results of PLA strands with bimodal dispersity (solid line) and monodispersity (dashed line) (b) Summary of gravimetry results and modulus at 80 °C of $S_{11k}[L]_{10k}$ with [] referring to bimodal dispersed strands. (c). Domain spacing (left and black) of $S_{11k}[L]_{10k}$ (closed circle, $Đ_{PLA} = 1.8$) and $S_{11k}L_{10k}$ (open circle, $Đ_{PLA} = 1.2$) vs. PLA weight fraction. (d) Schematic illustration of bimodal dispersity effects on domain spacing in minority phase with free chain ends in BCP (left) or confined chain ends in RECNs (right).

Interestingly, when PLA is the majority phase, the overall *d* spacing has a weak dependence on PLA dispersity, because it is more sensitive to PS minority domain as we have discussed in previous section. Whereas when PLA is the minority phase, greater PLA dispersity substantially decreases the overall domain spacing (Figure 24c). In contrast, increase of Đ in linear block copolymers has been studied to increase *d* spacing.[94–97] This is attributed to the low stretching penalty due to the existence of free long and short chains,

therefore leading to a large *d* spacing dominated by the longer chains, as illustrated in Figure 24d. However, in the case of RECNs, when both chain ends are crosslinked and confined to the interface, the longer chains tend to relax to a smaller domain size set by short chains, rather than overcoming high elastic energy penalty to stretch themselves. This explains why higher dispersity of strand length in minority domain leads to a decreased overall *d* spacing.

3.2.4 Junction Functionality

We lastly examine the effect of junction functionality (*f*) by replacing thiol-Michael addition chemistry with UV-initiated thiol-ene reaction, which generates free radicals and provides fast kinetics and high conversion.[98] Specifically, in comparison to the RECNs prepared with thiol-Michael chemistry, the higher conversion of thiol-ene chemistry tends to create networks with increased average *f*. Furthermore, due to the competition between step growth and chain growth reactions, thiol-ene (thiol-acrylate)[98] reaction to form copolymer networks generates higher variability in *f*. For a clean comparison, UV-initiated thiol-ene chemistry crosslinked samples UV-$S_{11k}L_{10k}$ are prepared using the same polymer strands as those used in $S_{11k}L_{10k}$. As shown in Figure 25a, increase of average *f* and *f* variability in UV-$S_{11k}L_{10k}$ widens the cocontinuous window by shifting onset of PS percolation threshold from 0.62 to 0.72, and that of PLA domain from 0.32 to 0.27. This indicates that for copolymer networks with higher average *f* and *f* variability at the PS/PLA interface, each constituent domain needs less apparent volume to form percolated nanostructures. Unlike $S_{11k}L_{10k}$, junctions of which located at the interface always have 4 arms ideally,

UV-$S_{11k}L_{10k}$ employs a more complex structure at the junctions. As illustrated in Figure 25b, we think that the local curvature of the PS/PLA interface is largely affected by the ratio of two polymer strands (r = PS: PLA, inserted in the figure). The larger the ratio is, the local interface is more likely to curve towards PLA domain, and vice versa. In this manner, we expect UV-$S_{11k}L_{10k}$ to have more flexible interfaces with various local curvatures during the self-assembly, which promote to form winding and disordered interconnected channels. Interestingly, compared to $S_{11k}L_{10k}$, smaller d spacing is observed for UV-$S_{11k}L_{10k}$ over all the compositions. Given the complex network structures in terms of effective strands length, f, etc., although there is no clear explanation to the smaller average d spacing observed for UV-$S_{11k}L_{10k}$, we speculate that high efficiency of thiol-ene reaction results higher crosslinking density, and the increase of average f leads to fewer junctions with exclusively one chain type and therefore less swelling of the domains.
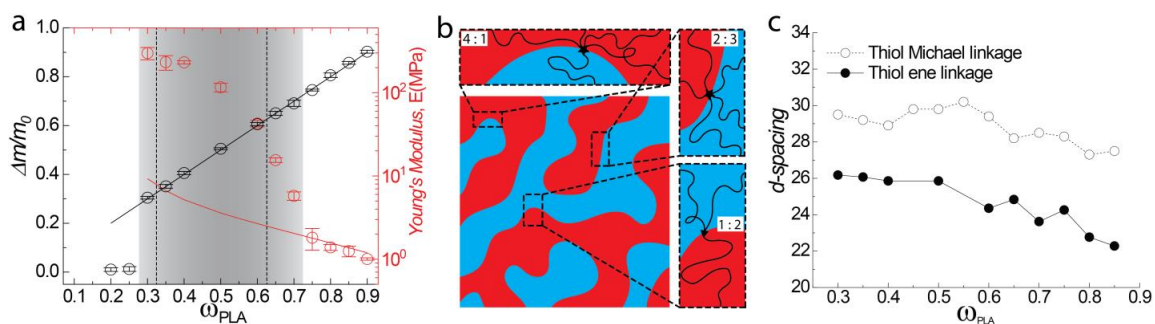
Figure 25. (a) Summary of gravimetry results and modulus at 80 °C of UV-$S_{11k}L_{10k}$ crosslinked by photo-initiated thiol-ene chemistry. (b) Schematic illustration of various junctionalities at the PS/PLA interface. The ratios denote the number of PS and PLA chains at the junction points. (c) Domain spacing of $S_{11k}L_{10k}$ (open circle) and UV- $S_{11k}L_{10k}$ (closed circle) vs. PLA weight fraction.

3.3 Conclusion

We have examined the nature of cocontinuous morphologies within PS/PLA RECNs using gravimetric and mechanical analysis. The phase diagram (χN vs. ω_{PLA}) of binary symmetric RECNs is then established, highlighting the critical microphase separation transition ($6 < (\chi N)_{critical} < 12$), above which disordered cocontinuous nanostructures span over 30 vol% from $\omega_{PLA} = 0.32$ to 0.62 and morphologies with dispersed domains resides on the sides. Facing the challenge of multi-dimensional parameter space of phase-separating networks, four experimental geometries (strand length M_n, strands asymmetry, strand dispersity $Đ$, junction functionality) are further evaluated to have a great impact on the microphase separated nanostructures. Analogous to well-studied block or branched copolymers, RECNs experience higher elastic energy penalty of stretching due to confinement of chain ends, resulting in the sensitivity of d spacing to the short chains in polydispersed domain, although it shows similar effects on cocontinuous window shifting towards high dispersity component. This model system builds a predictive understanding of network design to achieve cocontinuous nanostructures.

Chapter 4

STRESS-INDUCED ORIENTATION AND ANISOTROPY WITHIN CO-CONTINUOUS RECNS *

* Reprinted with permission from [*ACS Macro Lett.* **2018**, 7, 828−833]

4.1 Introduction

Anisotropic but three dimensionally co-continuous morphologies are of great utility in both natural and engineering materials, providing direction-dependent mass transport, energy absorption, and structural protection.[99–105] For example, in porous materials, aligned, yet still highly interconnected channels can not only provide enhanced mechanical properties along the preferred loading direction,[99–101] but also facilitate directional mass transport, such as of fluid and solutes in bone[99,100] and nutrients in plants[99,101,105]. To date, the synthesis of polymeric materials with controllably anisotropic interconnected morphologies has focused largely on kinetic trapping of macro-phase separated structures, e.g., through freeze-casting[106,107], melt processing[108,109] or thermally-induced phase separation,[110,111] with anisotropy introduced by controlling the crystal growth direction, extrusion rate, or temperature gradient, respectively. However, precise control over the competition between phase separation and structural arrest to achieve the desired interconnected structures, which typically have sizes in the micrometer range.

In many cases, achieving the desired material properties requires structural control on nanometer length scales.[4] Micro-phase separated block copolymers can provide anisotropic morphologies at this length scale, with shear

flow[62,112–114] and tensile deformation[115,116] providing convenient methods of alignment. However, it is often difficult to achieve oriented co-continuous morphologies due to the narrow composition window in which most block copolymers form co-continuous phases. Introducing crosslinks into microphase separated copolymers[57,58] is known to promote co-continuous morphologies, and furthermore can prevent structural relaxation after alignment. Although a number of studies have focused on strain-induced orientation in crosslinked block copolymers[117–119], the application of external forces to crosslinked copolymers has not been widely studied as a route to anisotropic and co-continuous nanostructured or nanoporous materials. Notably, de-alloying of metals offers a simple route to co-continuous nanoporous structures,[120,121] although typically without controlled levels of anisotropy.

As discussed in chapter 2 and 3, randomly end-linked copolymer networks (RECNs) serves as a kinetically insensitive route to co-continuous morphologies over a wide range (> 30 vol %) of composition.[47,79] Thermal instability of the urethane crosslinkers used previously leads to coarsening with thermal annealing, thereby obscuring the mechanism of structural reorganization at high temperature.[79,122,123] In this section, we study strain-induced orientation of PS/PLA RECNs with thermally stable thiol-Michael crosslinks, which provides a robust route to co-continuous materials with controlled anisotropy. Reorganization of domains proceeds initially by non-affine deformation at low strain, $\varepsilon \lesssim 0.4$, followed by domain rotation towards the stretching direction (SD) at higher strain, accompanied by topological rearrangements of the PS/PLA

interfaces. The orientation of domains yields dramatically enhanced toughness and increased stiffness of PS/PLA RECNs along the SD, while only slightly diminishing the mechanical properties in the transverse directions. Selective removal of PLA converts these materials to highly oriented porous PS structures.

4.2 Fabrication of Highly Anisotropic Interconnected Nanoporous PS

4.2.1 Functionalization of Precusor Polymers
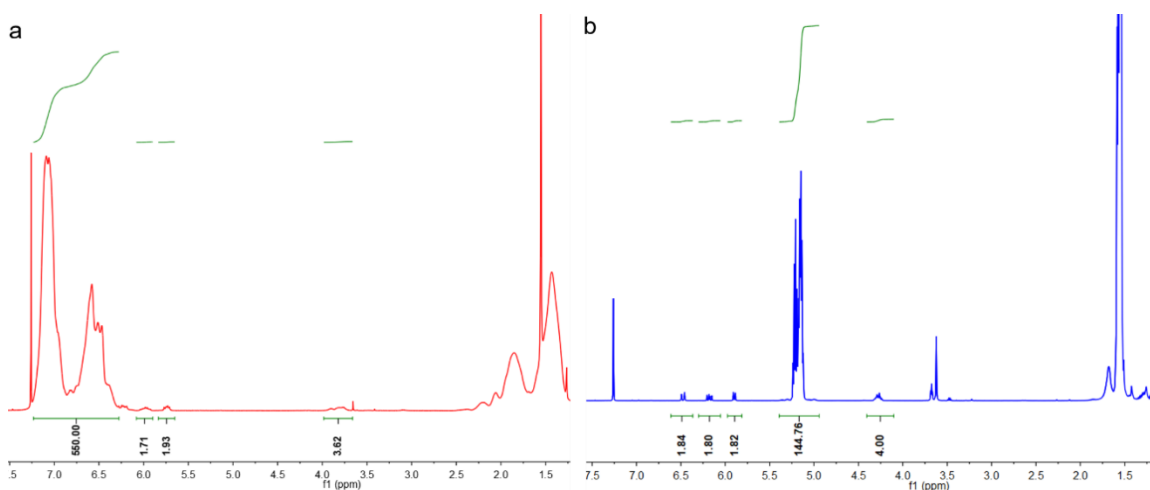
Figure 26. ^{1}H NMR in CDCl$_3$ of (a) PS (11 kg/mol) and (b) PLA (10 kg/mol) functionalized with acrylate end groups.

To prepare the diacrylate-terminated PS precursor, 2.0 g (0.18 mmol) of α,ω-dihydroxy terminated PS (M_n = 11 kDa), was dissolved in 30 mL of anhydrous dichloromethane (DCM), which had been distilled from calcium hydride, and equilibrated in an ice bath and purged with N$_2$. Acryloyl chloride (0.066g, 0.72 mmol) and triethylamine (0.074g, 0.72 mmol) were separately added drop-wise to the stirring polymer solution under N$_2$ flow. The solution was allowed to slowly warm to room temperature as it was stirred overnight. The product was precipitated three times into cold MeOH and collected by filtration at

91% yield. Figure 26 shows the NMR of the resulting product in CDCl$_3$ and acrylate end group functionality is calculated to be 1.8 using the peaks at 5.7, 6.0 ppm (H, -CH = CH$_2$) and 6.3-7.2 ppm (5H, - C$_6$H$_5$). Diacrylate-terminated PLA (M_n = 10 kDa) was prepared with the same procedure, and end group functionality is calculated to be 1.8 using the peaks at 5.8, 6.2, 6.5 ppm (H, -CH = CH$_2$) and 4.3 ppm (4H, -COO-CH_2-).

4.2.2 Anisotropic Networks and Porous PS Preparation
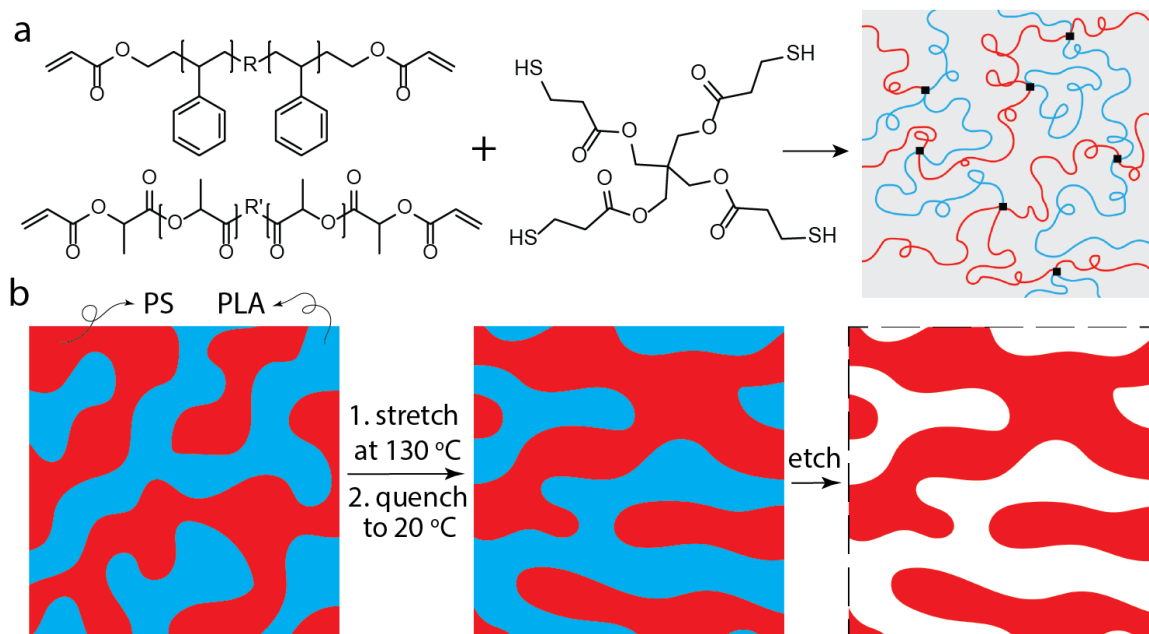
Figure 27. (a) Preparation of randomly end-linked copolymer networks from telechelic polystyrene and poly(D,L - lactide). (b) Schematic depiction of formation of anisotropic co-continuous PS/PLA RECNs and PS porous monoliths.

As shown in Figure 27a, Functionalized PS (90 mg) and PLA (110 mg, volume fraction of PLA = 0.51) were dissolved in 1.33 mL of DMF. After thoroughly mixing, 4.2 mg of pentaerythritol tetrakis(3-mercaptopropionate) (4SH) and 3.5 mg of triethylamine were added sequentially to the solution. This gave a total polymer concentration of 150 mg/mL. The 4SH, precursor polymers and

triethylamine gave a 1: 1: 1 molar ratio of double bond to thiol groups to triethylamine. The mixed solution was kept in a sealed vial under dark at room temperature for 1 day. The resulting gel was dried under nitrogen flow over 3 days, followed by thermal annealing at 150 ^{o}C overnight.
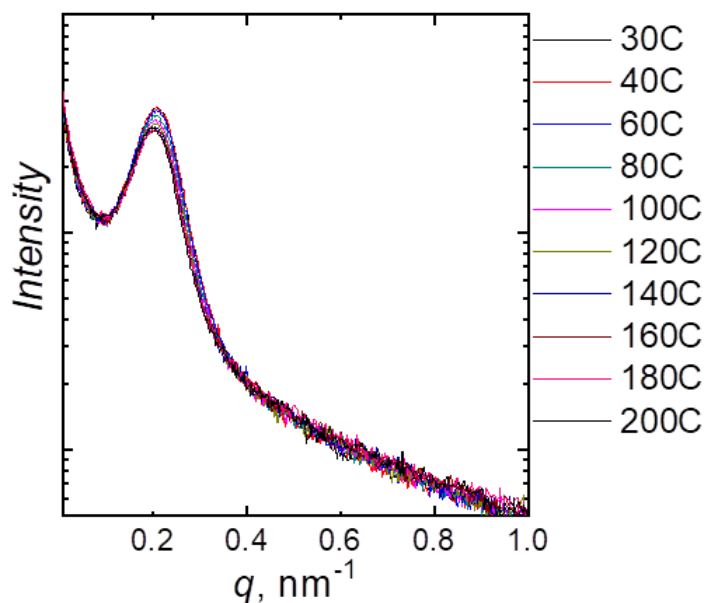
Figure 28. In-situ SAXS characterization of PS/PLA RECNs with thiol-Michael crosslinks. The near constancy of the pattern (showing only a slight, reversible, decrease in intensity with temperature) up to 200 °C indicates good thermal stability of the crosslinks.

To introduce anisotropy, RECNs samples are heated to 130 ^{o}C, above the glass transition temperature T_g of both PS and PLA (100 ^{o}C and 38 ^{o}C, respectively), and stretched uniaxially to a specified strain, reorienting domains along the stretching direction (SD), as depicted in Figure 27b. Stretched samples are annealed for 5 min before quenching to room temperature to lock in the morphology (no further changes in structure are observed for annealing times up to 24 h). These RECNs with thiol-Michael linkage are stable up to 200 ^{o}C, as

shown in Figure 28. To generate anisotropic porous PS monoliths, stretched samples are immersed in basic aqueous solution to etch PLA (Figure 29).
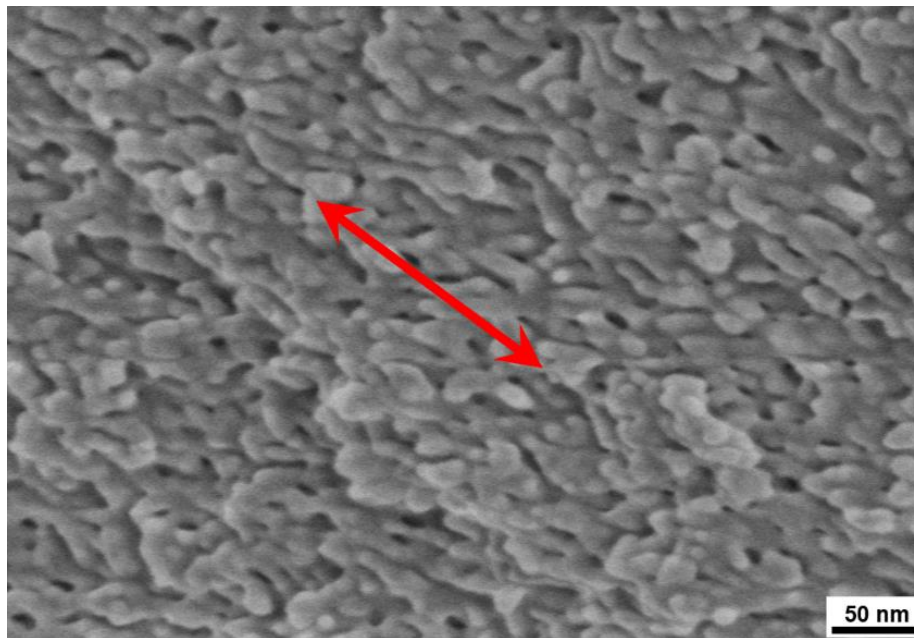
Figure 29. SEM image of anisotropic PS monolith (with 1 nm Au coating). Arrow denotes stretching direction.

4.3 Results and Discussion

4.3.1 Anisotropy Characterization and Demonstration

A typical stress-strain curve for a PS/PLA RECN measured at 130 ^{o}C is plotted in Figure 30a. A linear elastic response with modulus E = 0.4 MPa is found for $\varepsilon < 0.2$, followed by pronounced strain softening at intermediate strains ($\varepsilon > 1$). Notably, this phenomenon is absent for end-linked networks of either PS or PLA alone, whose responses are reasonably well described by a Neo-Hookean form (Inserted in Figure 30a). This "soft elastic" response of RECNs is reminiscent of that of liquid crystalline elastomers[124] and is associated with domain rotation in both cases (as described below for RECNs). Small angle X-

ray scattering (SAXS) measurements, shown in Figure 30b, reveal an isotropic structure with a characteristic length of d = 30 nm for as prepared PS/PLA RECNs. As we described previously,[79] this peak corresponds to the center-to-center spacing between neighboring domains of one component, across a domain of the other.
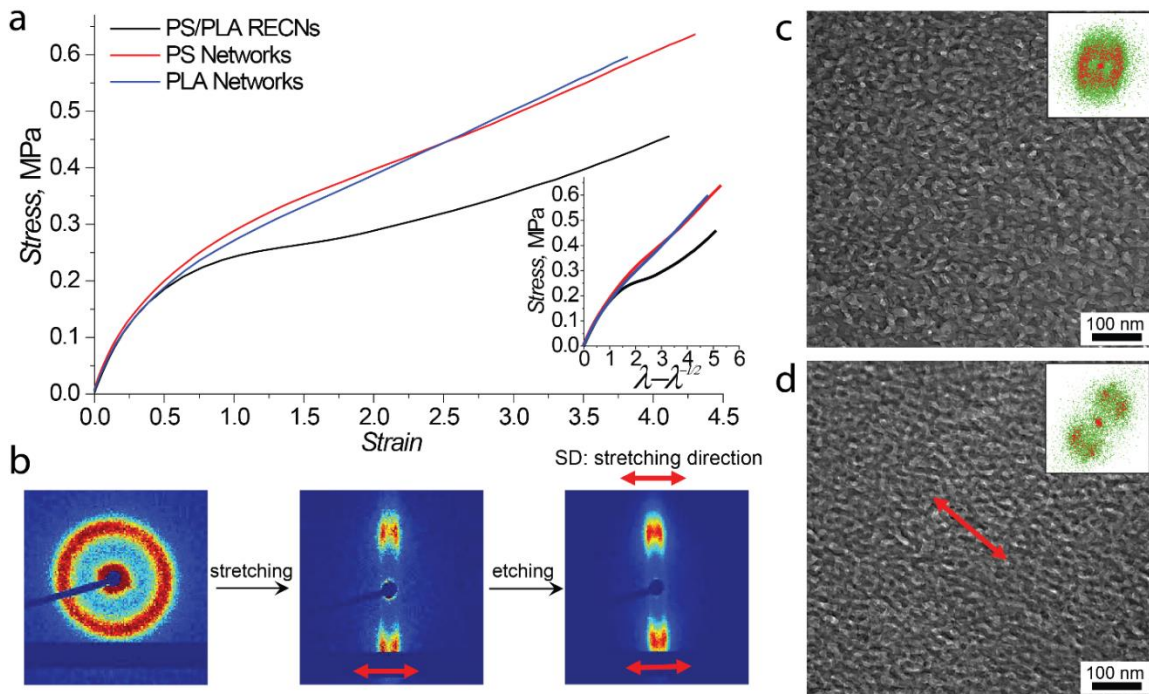
Figure 30. (a) Stress-strain curves for PS/PLA RECNs (black), PS networks (red) and PLA networks (blue) at 130 °C. (b) 2D SAXS patterns for PS/PLA RECNs, as prepared (left), after uniaxial stretching (middle) and after removal of PLA domains (right). TEM images of isotropic (c) and anisotropic (d) porous PS monoliths with fast Fourier transforms as insets. Arrows denote the stretching direction (SD).

When the sample is uniaxially stretched to ε = 4 at 130 °C, the pattern becomes highly anisotropic. The lack of a scattering peak along the SD indicates the absence of a regular structural length scale in this direction, while the intense peaks nearly in the transverse direction reflect a high degree of orientation of domain interfaces along the SD. After etching PLA, the scattering pattern stays

53

unchanged apart from a large increase in scattered intensity, confirming the formation of an anisotropic but interconnected porous PS structure. Transmission electron microscope (TEM) images on porous PS before and after deformation are shown in Figure 30c-d, further confirming orientation of domains along the SD. The fast Fourier transforms (FFT) are in good qualitative agreement with SAXS results, although slight anisotropy is evident in the undeformed sample, likely reflecting distortion due to cryo-microtomy. The co-continuity of oriented samples is confirmed by analysis of TEM tomograms (Figure 31), which indicates that > 99% of both PS and pore phases are percolated (with the remaining < 1% on the boundaries, and therefore also likely connected outside of the reconstruction volume)
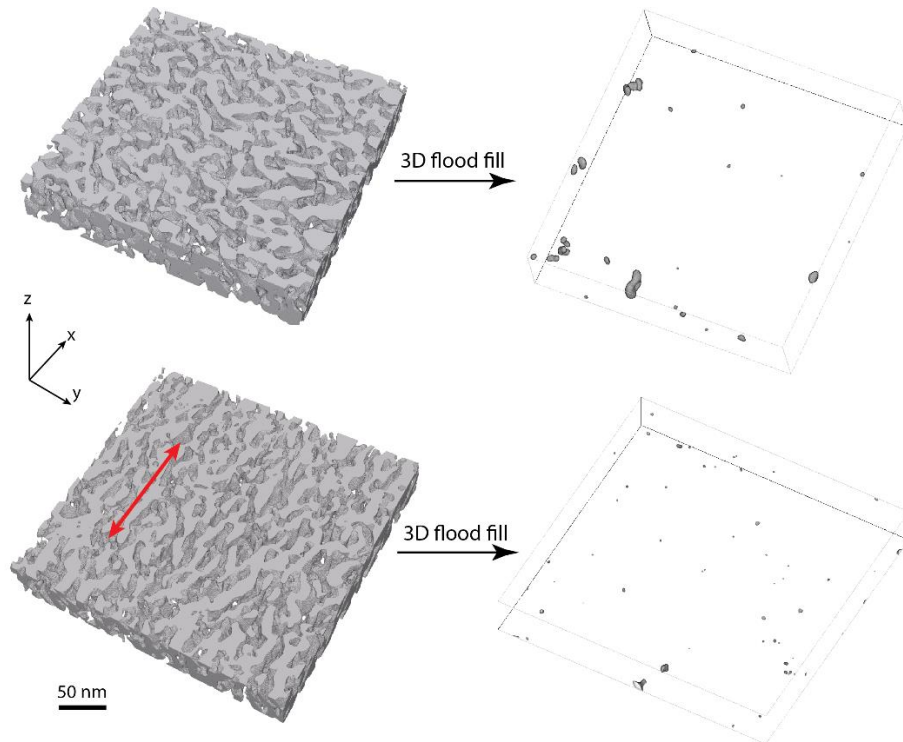
Figure 31. TEM tomographic reconstructions (left) of the isotropic (top) and anisotropic (bottom) porous samples with the PS phase shown in dark, and (right) following 3D flood filling of interconnected pores, with the unfilled (disconnected porous) portions shown in dark. These images are reconstructed by choosing a

threshold to delineate pores from PS walls based on matching the porosity to the value (1.02 cm^3/g) measured by N_2 adsorption.

4.3.2 Two Steps Morphology Evolution During Stretching

We now consider in detail how this reorientation occurs by varying the strain between 0 and 5, and find that it consists of a two stage process: first, stretching and compression of domains at low strain ($\varepsilon < 0.4$), followed by domain rotation at higher strain.
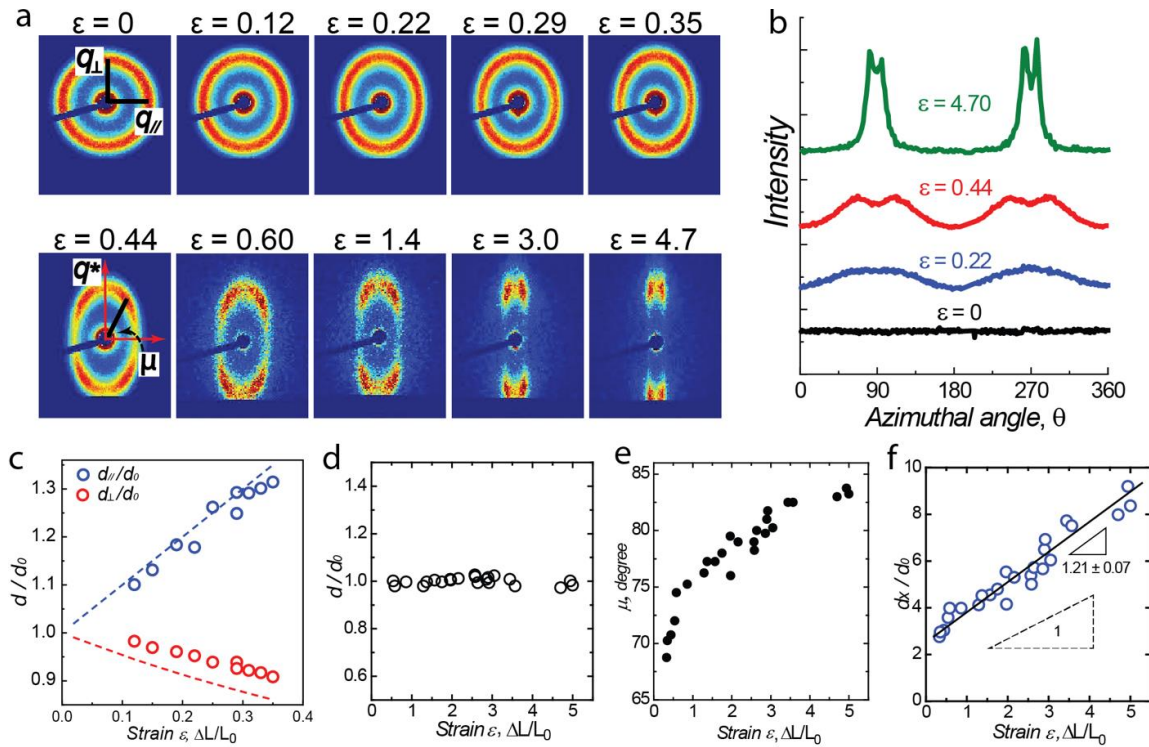
Figure 32. (a) 2D SAXS patterns for PS/PLA RECNs and (b) integrated scattering intensities between $q = 0.1$ and 0.3 nm^{-1} (covering the peak position) as a function of azimuthal angle at the indicated strain values. (c) Domain spacing parallel (blue) and perpendicular (red) to the SD in the low strain regime, normalized by the undeformed value d_0. Normalized primary domain spacing, d/d_0 (d), angle μ between the interface normal and SD (e), and decomposed domain spacing, d_x/d_0 (f) in the high strain regime

Figure 32a shows 2D SAXS patterns for samples at different strains. In the upper row, as the strain increases from 0 to 0.35, the circular scattering pattern evolves to an ellipse, with the major and minor axes perpendicular and

parallel to the SD, respectively, revealing that the domains are stretched along the SD and compressed along the perpendicular direction. Defining corresponding characteristic lengths $d_\perp = 2\pi/q_\perp$ and $d_{//} = 2\pi/q_{//}$, we quantify the increase in $d_{//}$ and decrease in $d_\perp$ with strain in Figure 32c. The dashed lines $d_{//}/d_0 = \varepsilon + 1$ and $d_\perp /d_0 = (\varepsilon + 1)^{-1/2}$ represent the expected variations for affine uniaxial stretching (assuming incompressibility, as verified by a < 1% change in macroscopic volume). Values for $d_{//}$ fall close to the affine prediction, while those for $d_\perp$ are substantially larger, suggesting that the domains reorganize to resist compression along the directions transverse to the SD. To further analyze the 2D SAXS pattern of stretched sample, the scattering intensity integrated over the range q = 0.01 - 0.03 nm^{-1} (which covers the scattering peak) is plotted as a function of azimuthal angle θ (or displayed as μ), as shown in Figure 32b. For ε = 0.22 (blue curve), the scattering intensity becomes weaker along the SD, providing further evidence that the domains reorganize to stay closer to their preferred spacing. At strains above 0.4 (Figure 32a-b), the scattering concentrates into 4 spots, which become narrower in azimuthal distribution and rotate toward the perpendicular direction with increasing strain. These 4-spots patterns indicate that the domains align preferentially at a strain-dependent angle relative to the SD, in agreement with the TEM images in Figure 30d. We characterize the structures in the domain rotation regime using the scattering vector q^* and orientation angle μ, as illustrated in Figure 32a, with $d = 2\pi/q^*$ reflecting the characteristic spacing and μ representing the angle between the interface normals and the SD. With increasing strain, as shown inFigure 32d and

f, d/d_0 remains nearly constant, while μ increases steadily from 68° to 83°, revealing that the morphology evolves by domain rotation with constant domain size. The initial angle of 68° corresponds to the orientation where the value of d remains at d_0 throughout the low-strain, non-affine deformation regime. In Figure 32e, we plot the component of the peak position along the SD, i.e., $d_x = 2\pi/(q^*\cos\mu)$, against strain, and find a line with slope slightly above the value of 1 expected for affine rotation of incompressible object.[125,126] This is in contrast to the behavior of block copolymers with one glassy block, where affine domain rotation is observed and the reorganization of domain interfaces is restricted.[125–127] Notably, the onset of domain rotation at a strain of $\varepsilon = 0.4$ corresponds well with the onset of "soft elasticity" in Figure 30a, indicating that much like in liquid crystalline elastomers,[124] domain rotation requires lower forces than stretching of homogeneous networks of either PS or PLA alone. Although the value of $\varepsilon = 0.4$ for the onset of domain rotation is not well-understood at present, we speculate that it may reflect an ability for chains to initially stretch at small applied strains, followed by an effective stiffening at higher strains.

The degree of orientation can be quantified in terms of the order parameter $P_2 = \frac{1}{2}(3\langle cos^2\theta\rangle - 1)$ with $\langle cos^2\theta\rangle = \frac{\int_0^{2\pi} (I_q(\theta)cos^2\theta|sin\theta|)\,d\theta}{\int_0^{2\pi} (I_q(\theta)|sin\theta|)\,d\theta}$, where a value of $P_2 = -0.5$ would indicate perfect orientation of the normal vectors to the domain interfaces perpendicular to the stretching direction. The order parameter P_2 (Figure 33) reaches -0.4 (where -0.5 indicates perfect orientation of interface

normals perpendicular to the SD) at strains of 4 - 5, indicating a high degree of alignment.
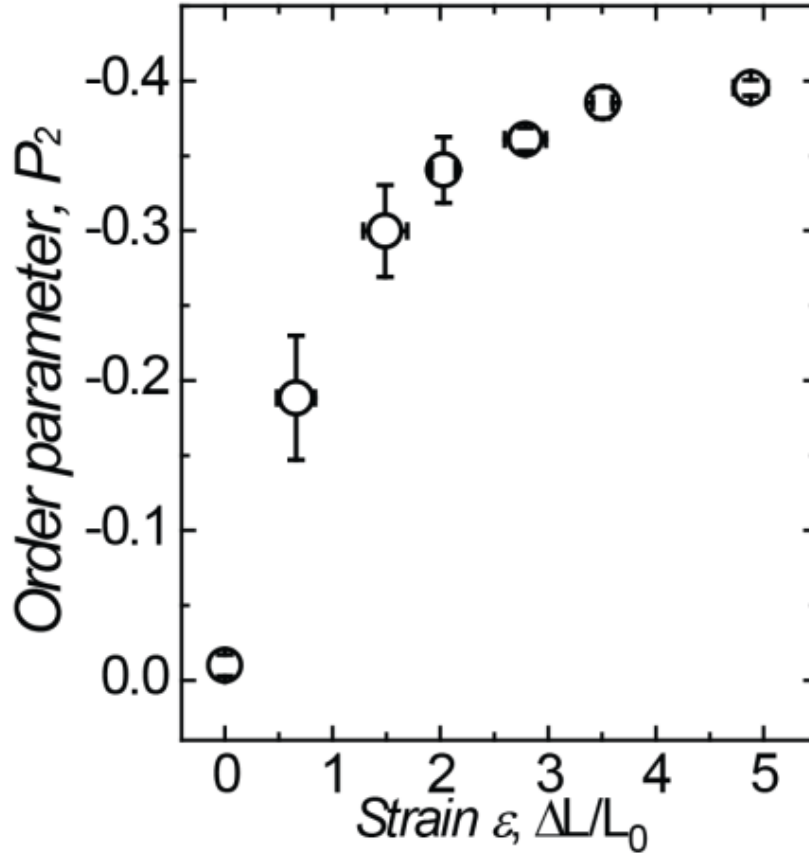
Figure 33. Order parameter P_2 calculated for PS/PLA RECNs as a function of strain.

4.3.3 Topology Changes

The fact that both stages of structural evolution involve non-affine deformation implies that the domains of PS and PLA must locally adjust their structures to accommodate the applied strain. To study this rearrangement, two porous PS samples (one unstretched, the other pre-stretched to $\varepsilon = 4$) are imaged by TEM tomography, as shown in Figure 31. To better visualize the nanostructures, a small portion of the tomogram is shown for the unstretched

sample in Figure 34a, along with a skeletonization of the PS domain obtained using a strut-thinning algorithm in Figure 34b, and the meshed PS/pore interface in Figure 34c.
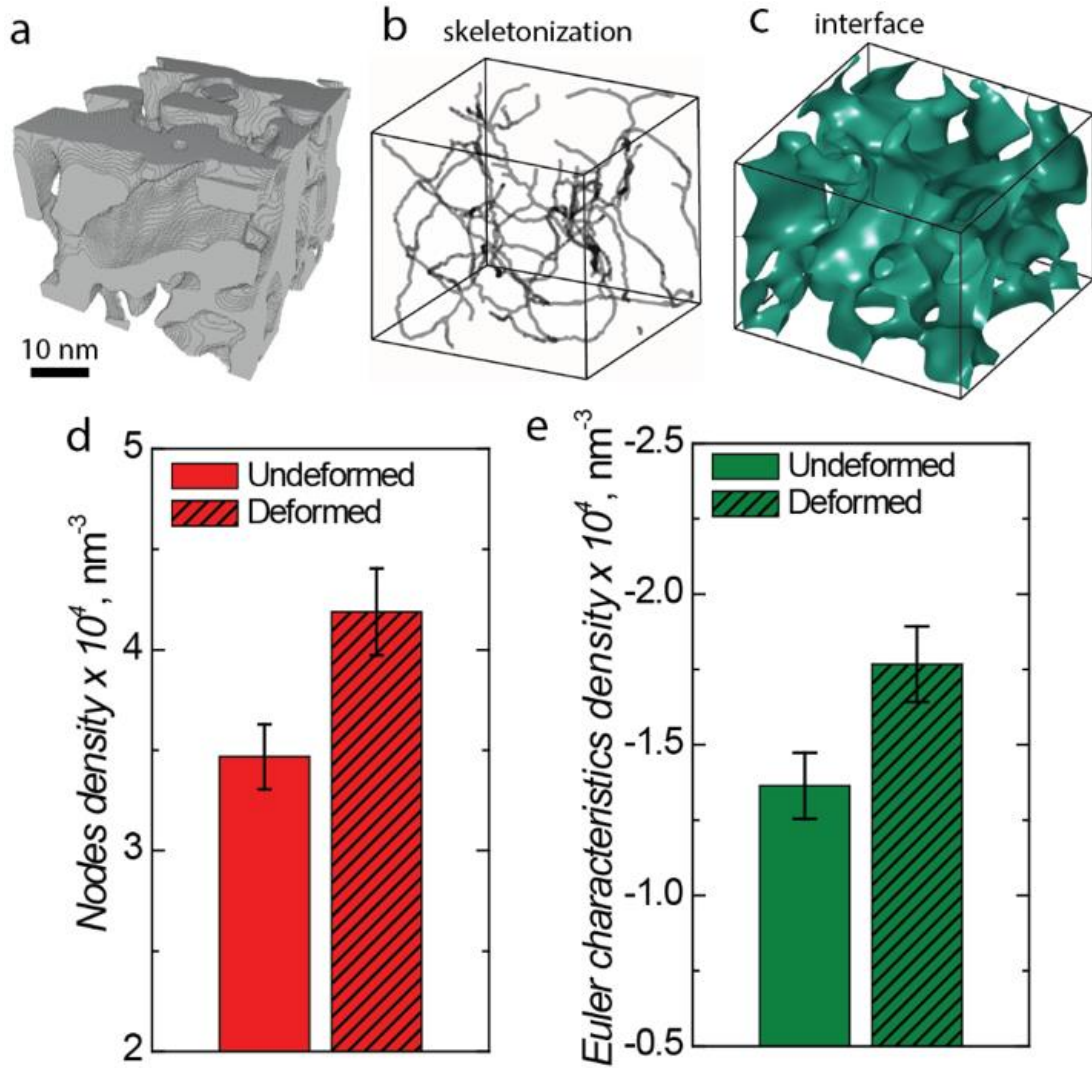
Figure 34. (a) A tomogram of an unstretched porous PS monolith (dark: PS, light: pores), with its corresponding (b) skeletonization and (c) interface mesh. (d) node density and (f) Euler characteristic density for isotropic (undeformed) and anisotropic (deformed) porous monoliths.

Analysis of the skeletonized PS phase reveals a node density of 3.4×10^4 nm^{-3}, of which 89% are triple junctions and the rest are quadruple. In comparison, the stretched sample shows a significant increase in node density to 4.2×10^4

nm^{-3}, with almost the same fraction of triple junctions (88%). Similarly, the Euler characteristic density (a topological invariant of a surface) increases by about 30% in magnitude from the isotropic to the stretched sample, reflecting an increase in the density of "holes" in the inter-material dividing surface. Both measurements clearly reveal that the topology of the nanostructure changes under strain, i.e., the interface between the PS and PLA domains rearranges, leading to net creation of new PS-PS and PLA-PLA connections, and thereby allowing the domains to accommodate the applied deformation without deviating too far from their preferred spacing.

	Surface area, S (m^2/g)
Isotropic	178
Anisotropic	195

Table 2. Table of surface area of interfaces between PS matrix and pores calculated from TEMT reconstructions for both isotropic an anisotropic samples, by assuming negligible sample densification and constant porosity (1.02 cm^3/g), as confirmed by the lack of change in either the macroscopic sample dimensions or the location of the SAXS peak.

In addition, the specific interfacial area (S) measured from the tomograms increases by 10% upon stretching (Table 1); this is well below the expected value for a sample undergoing affine deformation, further confirming that the RECNs are able to adjust their interfacial structure under strain. Notably, the tomogram of the pre-stretched co-continuous nanostructure shows substantially smaller tortuosity for the pores along the SD (τ = 1.71), compared to that along the orthogonal in-plane direction (3.50), whereas that for the isotropic sample yields τ = 1.83 and 2.29 (Figure 35).
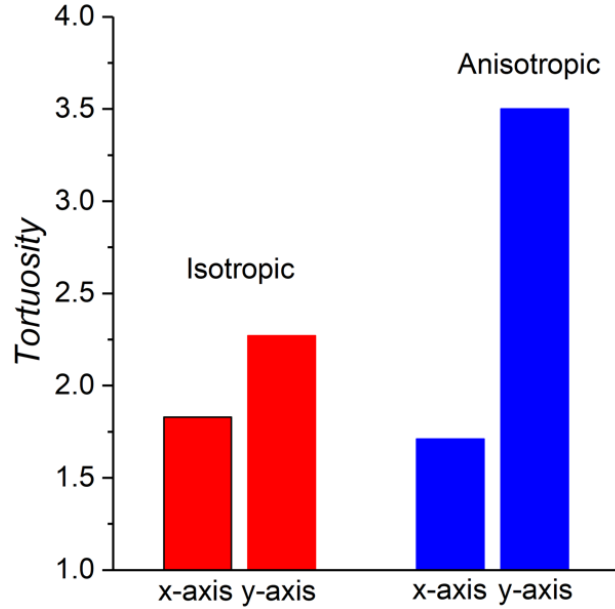
Figure 35. Tortuosity of pores extracted from the tomograms for both isotropic and anisotropic samples along the two in-plane directions. For the anisotropic sample, the SD is along the x-axis. Tortuosity is calculated using a MATLAB routine from the binary (thresholded) tomogram.[128]

4.3.4 Mechanical Properties of Anisotropic RECNs

To understand the influence of nanostructural orientation on room temperature mechanical properties of PS/PLA RECNs, we conduct uniaxial tensile tests. For each tensile test, a rectangular piece is cut from the material with dimensions of 0.3 mm × 1 mm × 10 mm, and the extension rate is fixed at 1 %/min. As seen in Figure 36a, isotropic glassy PS/PLA RECNs yield below 1% strain, with a tensile strength of 19 MPa. The brittle nature of this sample is consistent with the small number of entanglements[44,129] and low crosslinking density within the networks. When pre-oriented above T_g, however, the sample does not yield until around 2% (61 MPa yield strength) and exhibits ductile necking (Figure 36a, inset) before breaking above 80% strain. This ductile stretching absorbs a large amount of energy, increasing toughness nearly 600-fold compared to unoriented RECNs (from 11 to 6200 MJ/m^3). To better

understand the origin of these improvements in mechanical properties, we also characterize pure PS and PLA alone. For pure PS networks, pre-stretching does improve the tensile strength, from 13 to 43 MPa, but the oriented materials still undergo brittle failure at 5 % strain. On the other hand, pre-stretching PLA networks both improves the yield strength, from 17 to 34 MPa, and gives rise to necking with ultimate strain of 190%, suggesting that the ductility in pre-stretched PS/PLA RECNs is mostly due to the oriented continuous PLA domains, likely due to fibrillation of PLA during fracture.[130,131]
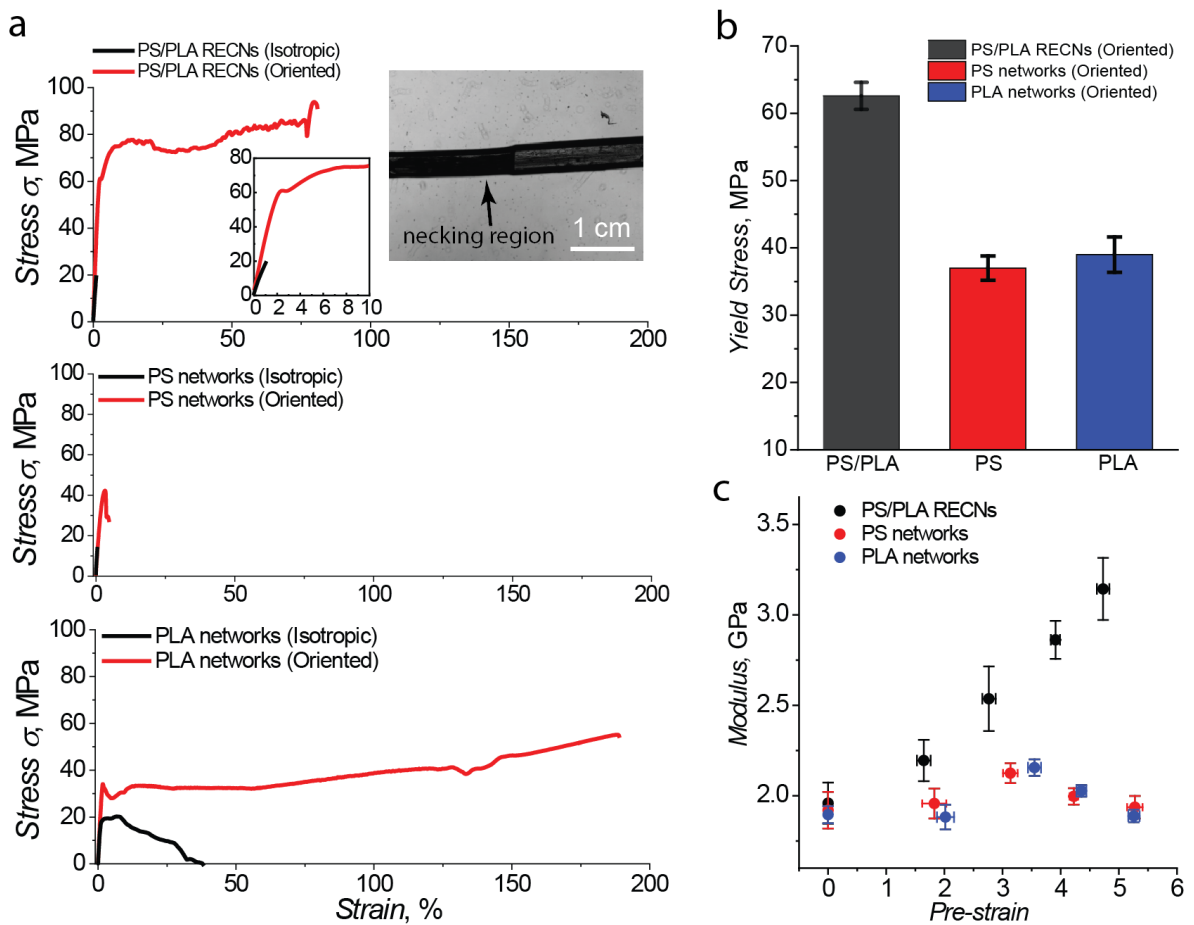
Figure 36. (a) Stress-strain curves for PS/PLA RECNs (top), PS networks (middle) and PLA networks (bottom) under uniaxial extension at room temperature (black: as-prepared isotropic network; red: pre-oriented anisotropic

networks deformed parallel to SD, ε = 5). (b) Comparison of yield stress among pre-oriented networks, ε = 5 (averaged for multiple samples). (c) Elastic modulus of networks with varying amounts of pre-orientation.
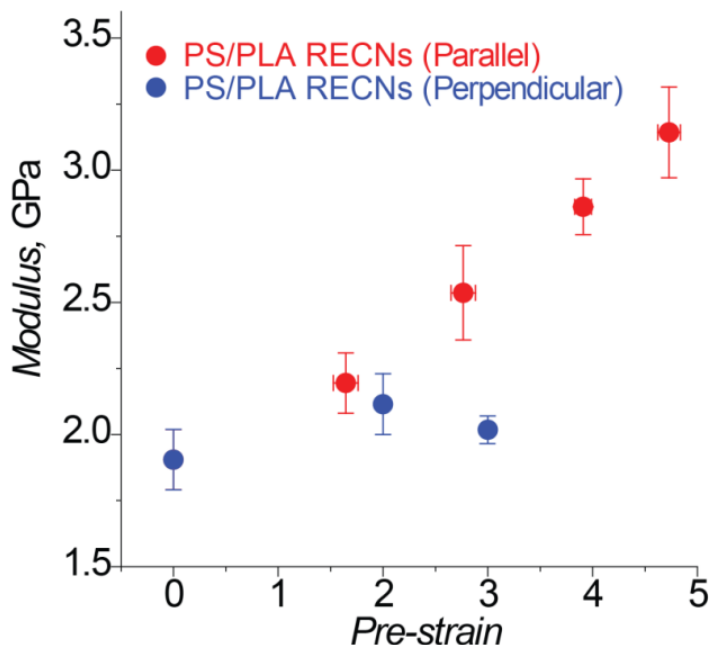
Figure 37. Elastic modulus of PS/PLA RECNs parallel and perpendicular to the SD, with different amounts of pre-strain.

Remarkably, however highly oriented PS/PLA RECNs (ε = 5) show a substantial improvement in yield stress (1.5-fold) over either pre-stretched PS or PLA networks alone, as shown in Figure 36b. Moreover, Figure 36c shows that PS/PLA RECNs also exhibit increasing elastic modulus along the SD (up to 3.2 GPa) as a function of pre-strain, while PS and PLA networks retain a modulus close to their unoriented value of 2 GPa. This increase in both modulus and yield stress of oriented PS/PLA RECNs compared to either of the components is surprising. While further study is needed to understand this behavior in detail, we note that similar phenomena have been observed in a few cases,[132,133] and speculate that the oriented microphase separated structure resulted from pre-stretching leads to an even higher degree of chain orientation in PS/PLA RECNs

compared to networks of PS or PLA alone. In the transverse direction, as shown in Figure 37, the stiffness (modulus) of PS/PLA RECNs stays almost unchanged with strain (though we could only reach $\varepsilon = 3$ in this direction due to the difficulty in sample preparation).

4.4 Conclusion

We have developed a simple method to introduce controlled orientation into co-continuous copolymer networks with well-defined architectures. Continuity can be preserved at various orientations, thus offering a robust route to highly anisotropic porous materials by selective removal of one domain. The morphology evolves via a two-stage process, where the domains initially undergo non-affine stretching and compression, followed by non-affine domain rotation that also manifests through a "soft elastic" response. Real-space morphologies obtained from transmission electron microscopy tomography indicate a change in topology during orientation, confirming the rearrangement of domains and interfaces during the non-affine deformation. The combination of molecular and microdomain orientation has a strong influence on mechanical properties, yielding materials that are both stiff and tough along the pre-stretching direction.

Chapter 5

CO-CONTINUOUS MORPHOLOGIES WITHIN LINEAR AND BRANCHED COPOLYMERS WITH DISPERSED BLOCK LENGTH

5.1 Introduction

Microphase-separated nanostructures and morphologies derived from multi-components polymers have received considerable attention due to their potential applications in a variety of fields.[134–137] The co-continuous morphology is of specific interest because multiple chemically-distinct components form their own independent continuous regions throughout the bulk materials, offering opportunities to synergistically integrate properties and function into a single polymer composite.[7–11] While equilibrium self-assembly of block copolymers[5] or microemulsions[78] have been investigated to form co-continuous morphologies, these structures are generally found in very narrow composition windows, raising practical challenges to producing them in robust and generalized processes. Recently, our group and co-workers[47,79,80] have demonstrated a kinetically insensitive method to achieve disordered co-continuous nanostructures with robustness and generality by designing randomly end-linked copolymer networks (RECNs) with well-defined architectures. However, introducing crosslinks prevents subsequent solution or melt processing, limiting the ability of these materials to be employed in many industrially-relevant contexts.

Similar to RECNs, multiblock copolymers (MBCs) with many blocks can also form disordered co-continuous morphologies.[138–143] In comparison to AB

diblock or ABA triblock copolymers, [5,144,145] MBCs provides substantially increased structural complexity, including number of blocks, effective block length, block sequence, factors which are reported to have great impacts on the nanostructures formed.[138,146–153] For example, changing from alternating MBCs to random MBCs increase the randomness of block sequence, leading to longer average block lengths and higher block dispersity, which favors disordered co-continuous nanostructures.[138] Although a number of living polymerization techniques have been developed to design versatile polymer architectures and precisely control molecular weight, dispersity, and functionality of MBCs, they are still expensive and tedious. Step growth polymerization of end functionalized small molecules or polymers offers a method to form multiblock copolymers with complex architectures and chemistries,[138,139,146,154,155] including commercially important polyurethane and polyesters.[156,157]

To access co-continuous nanostructures, linear diblock copolymers serve as a versatile method in terms of processability, but the narrow composition window for the stable double gyroid phase (~ 5 vol %) requires strict synthetic control. In contrast, RECNs with well-defined architectures offers a much wider co-continuous window (~40 vol % as discussed in chapter 3) but suffer from poor processability. In this chapter, we seek to understand the microphase separation of MBCs, and compare their ability to form disordered co-continuous structures to that of RECNs. For a direct comparison to our previously studied RECNs, MBCs are synthesized using step-growth polymerization of telechelic polystyrene (PS) and poly ($_{D,L}$ - lactide) (PLA), while keeping block (strand) length constant. With

the same linking chemistry (thiol-Michael addition, as used to form RECNs), we are able to achieve MBCs with a number average of 3 – 4 blocks, and a dispersity, $Đ = M_w/M_n \approx 2$. Interestingly, when far away from critical microphase separation transition (MST), these disperse MBCs show only a narrow co-continuous window (< 10 vol %) due to their propensity to form ordered nanostructures. However, when closer to MST, disordered co-continuous nanostructures occupy a much wider window (~ 25 % vol), approaching that of RECNs. We attribute the segregation strength dependent morphological behavior to the dramatically increased concentration fluctuation close to MST, which drives MBCs into disordered nanostructures with curved interfaces, therefore favoring co-continuous nanostructures.

5.2 Materials & Methods

Materials

Dihydroxyl-terminated PS and PLA, acryloyl chloride, 2,2'-(Ethylenedioxy) diethanethioltriethylamine, trimethylolpropane tris(3-mercaptopropionate), DMF, and methanol are purchased from Polymer Source, Advanced Polymer Materials, Sigma Aldrich, and Fisher Scientific, respectively, and used without further purification.

Functionalization of Precursor Polymers is described in chapter 3 to prepare di-acrylate terminated PS and PLA.[80]

Synthesis of linear and branched multi-block copolymers

Taking L_$S_{5k}L_{5k}$ – 50 as an example to synthesize linear multi-block PS/PLA copolymers, di-acrylate functionalized PS (40 mg) and PLA (40 mg) are

dissolved in 0.9 mL of DMF. After thoroughly mixing, 2.6 mg of 2,2'-(ethylenedioxy) diethanethioltriethylamine (di-SH) and 29 mg of triethylamine are added sequentially to the solution. This gives a total polymer concentration of about 8 % wt/wt. The 2SH, precursor polymers and triethylamine give a 1: 1: 10 (for all samples) molar ratio of double bond to thiol groups to triethylamine. The mixed solution is kept in a sealed vial starring at 60 °C for 3 days. The resulting solution is precipitated to cold methanol twice, followed by solution casting (DMF) and thermal annealing at 150 °C overnight. For branched PS/PLA copolymers, a mixture of 2SH and trimethylolpropane tris(3-mercaptopropionate) (tri-SH) is added with stoichiometry = SH / acrylate = 0.7 and branching fraction = (tri-SH * 3) / (tri-SH * 3 + di-SH * 2) = 0.5.

5.3 Results & Discussion
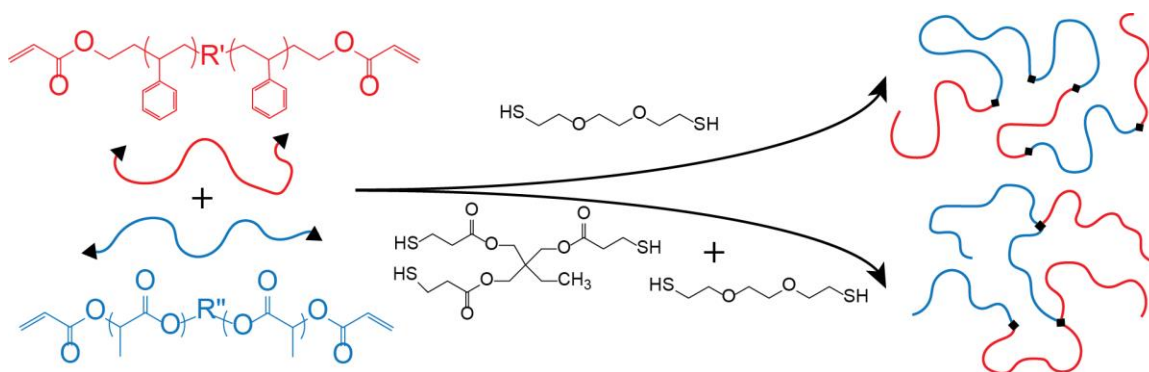
Figure 38. Synthetic scheme for preparing linear and branched multiblock copolymers.

To conduct a systematic study of the relationship between the copolymer architecture and morphological behavior, we rely on step polymerization to prepare linear and branched MBCs from di-acrylate functionalized PS and PLA precursor with symmetric strands length, $M_{n,PS} \approx M_{n,PLA}$. Synthetic details are

described in *Materials and Methods* section. Pre-designing telechelic polymer precursors provides a simple way to achieve randomly linked linear and branched MBCs, either by incorporating dithiol (di-SH) or mixture of di-SH and trithiol (tri-SH), respectively, as illustrated in Figure 38.

5.3.1 Linear Multiblock Copolymers
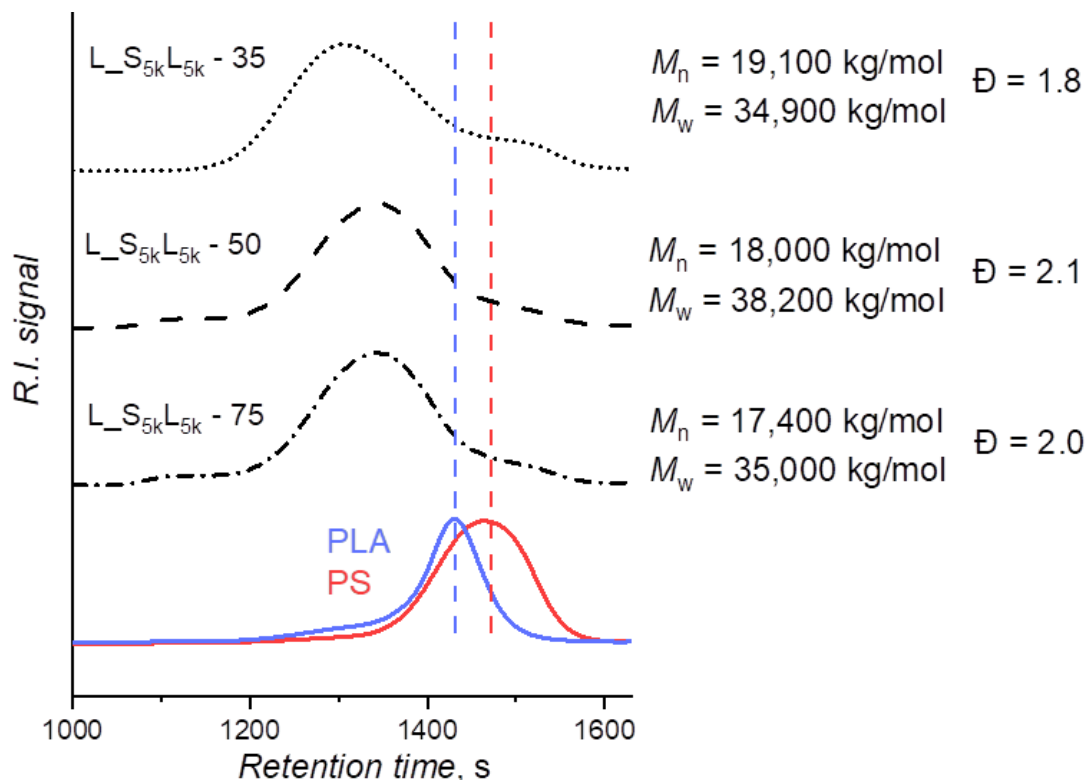
Figure 39. GPC traces of linear multiblock PS/PLA copolymers, $L\_S_{5k}L_{5k} - 35$, 50 and 75 synthesized by step polymerization of diacrylate functionalized telechelic PS (M_n = 5 kg/mol) and PLA (M_n = 5.5 kg/mol) precursors.

We first examine the simplest case of linear multiblock copolymers with strand length of precursor polymers characterized as $M_{n,PS}$ = 5.0 kg/mol and $M_{n,PLA}$ = 5.5 kg/mol. Samples are named with the convention $L\_S_{MPS}L_{MPLA} - X$, where the subscripts refer to the molecular weights of the respective strands and X represents the percentage by weight of PLA initially present in solution. Gel permeation chromatography (GPC) in Figure 39 confirms the presence of higher

molecular weight MBCs and decrease of lower molecular weight PS and PLA precursors. We resolve total number average molecular weight M_n for all $L\_S_{5k}L_{5k}$ samples in the range of 16 – 20 kg/mol. Compared to the 5 kg/mol precursors, this indicates an average number of macromolecular blocks per MBC, $n = 3 – 4$. Noticeably, the apparent upper limit of block number is not very high, mainly due to the incomplete functionalization of telechelic polymers. As characterized by NMR, only 1.8 chains ends per linear polymer precursor are functionalized, leading to a sharp decrease of M in final MBCs According to Carother's equation, the upper limit sets at n = 10.[158] Also, the imperfect stoichiometry and less than 100% conversion further decrease the average block number. Interestingly, a small shoulder at even lower M region (M_n < 5 kg/mol) is observed, suggesting cyclization of single polymer precursors, though further experiments are required to evaluate their existence. In addition, the expected incomplete conversion of functional groups in thiol Michael reaction also limits the further increase of M and reduces the average block number n. Although step polymerization suffers from these limitation and difficulties when synthesizing MBCs from pre-designed macromolecules, it introduces an important parameter in designing disordered co-continuous morphologies. This parameter can be described as architecture randomness, which is reflected in several perspectives, such as the connecting sequence of blocks, effective block length and overall chain length polydispersity. For example, GPC shows that all those samples have a broad distribution of molecular weight, with polydispersity, Đ, in the range

of 1.6 − 2.2. Considering the dispersity, the weight average number of blocks increases to $n = 5 - 8$.
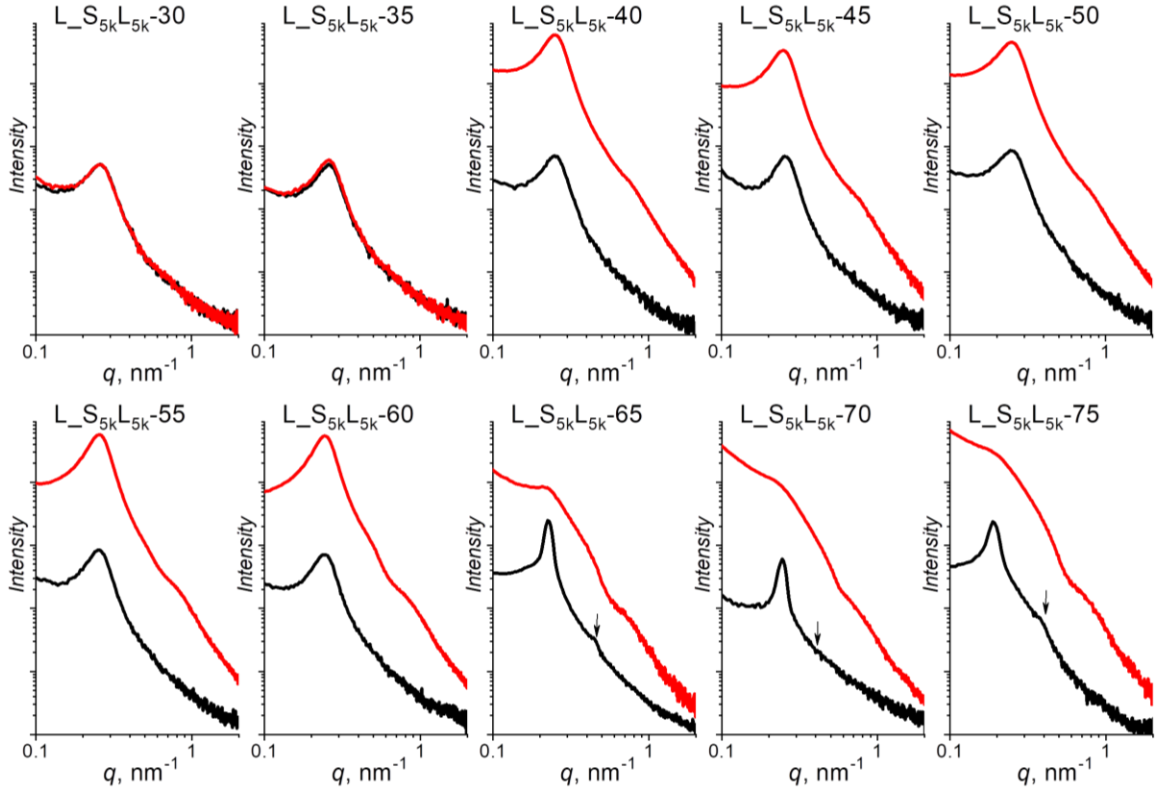
Figure 40. SAXS patterns of $L\_S_{5k}L_{5k}$ with different PLA weight fraction ($n = 3 - 4$, $Đ = 1.6 - 2.2$). Black: before etching. Red: after etching.

The morphology of linear MBCs, $L\_S_{5k}L_{5k}$, is evaluated by small angle X-ray scattering (SAXS), as shown in Figure 40. Taking advantage of the chemical degradability of PLA domains, we compare SAXS before and after immersing samples in alkaline solution (1 M NaOH in methanol/water, 6/4, v/v) to selectively remove PLA domains, which provides additional information to determine the connectivity of microphase separated structures. In Figure 40, the weight fraction of PLA is varied from 0.35 to 0.75, leading to distinctive SAXS patterns both before and after PLA removal. Based on the scattering profiles, three regions are identified with increased $ω_{PLA}$. (1) When $0.4 \leq ω_{PLA} \leq 0.6$ ($L\_S_{5k}L_{5k} - 40, 45, 50,$

55, 60), a broad primary scattering peak without higher order peaks is observed before etching PLA domains (black), reflecting the morphology with a well-defined characteristic length, $d = 2\pi/q^* = 25$ nm, but no long-range ordering or orientation. Etching PLA in this region forms corresponding nanoporous structures, which exhibit a scattering profile with the same shape and d spacing, suggesting that PS matrix has not changed its characteristic structures. The substantially increased scattering intensity, due to the increase of electron density contrast between PS and pores, further confirms the formation of nanoporous structures. Indeed, the scattering patterns are very much the same as what we observed for randomly end-linked copolymer networks (RECNs),[79] suggesting MBCs in this region exhibit similar disordered co-continuous nanostructures. (2) When $\omega_{PLA} \leq 0.35$ ($L\_S_{5k}L_{5k} - 30, 35$), SAXS patterns of as prepared samples show comparable profiles, while immersing in alkaline solution over several days does not noticeably change the shape or intensity of scattering patterns, indicating PLA domains in this region are not accessible to the etching solution. Indeed, gravimetric analysis quantifies that only less than 2% PLA domain can be removed, which is attributed to the partially connected nanostructures located on the sample surface. We speculate the microphase separated structures are disordered, without long-range orientation but slightly branched PLA domains dispersed in continuous PS matrix. (3) When $\omega_{PLA} \geq 0.65$ ($L\_S_{5k}L_{5k} - 65, 70, 75$), scattering patterns of as-prepared MBCs evolve to dramatically different profiles with greatly reduced full width at half maximum (FWHM). Additionally, the appearance of higher order peaks (as pointed by

arrows, however very weak for $L\_S_{5k}L_{5k}$ – 70) in Figure 40 indicates ordered nanostructures with decreased primary q*, corresponding to increased characteristic length d = 28, 27, 34 nm, respectively. Quantitative removal of PLA domain broadens the scattering peak and substantially increases scattering intensity at larger $q*$ due to the collapse of porous structures, suggesting that the PS matrix is not fully percolating in 3D.
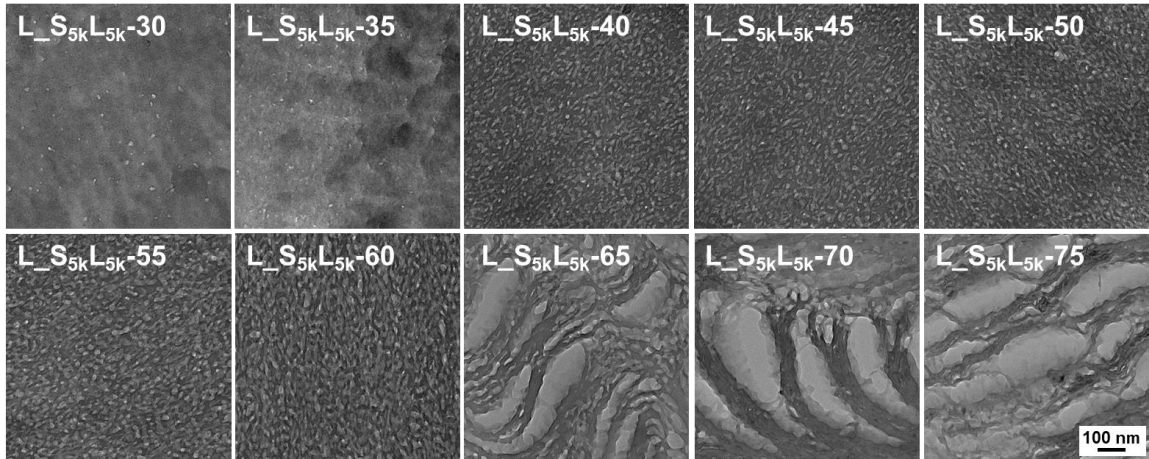
Figure 41. TEM images of porous PS by selectively removing PLA domains within PS/PLA MBCs $L\_S_{5k}L_{5k}$ with different PLA weight fractions (n = 3 – 4, Đ = 1.6 – 2.2). Dark regions are PS domains and bright regions are pores.
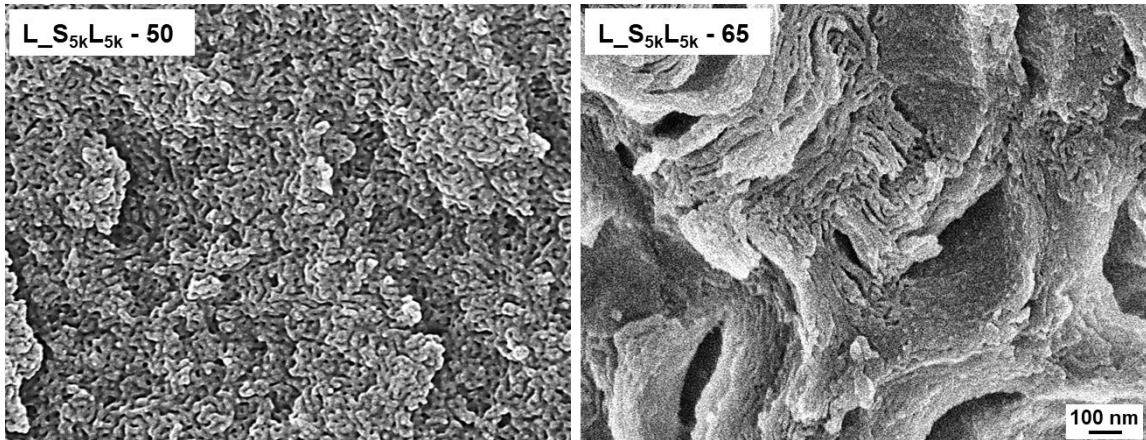
Figure 42. Scanning electron microscope (SEM) characterization of porous PS monoliths fabricated by etching PLA domains in MBCs, (left) co-continuous $L\_S_{5k}L_{5k}$ – 50 and (right) lamellar $L\_S_{5k}L_{5k}$ – 65. 1 nm of Au was coated before imaging.

The morphologies in each region are further characterized and confirmed using transmission electron microscopy (TEM), as shown in Figure 41. Although assessing the 3D structure from 2D TEM images is challenging, samples show projected contrasts in qualitatively agreement with SAXS. In fact, these MBC samples are imaged after immersing in alkaline solution for long enough time to remove accessible PLA domains. Porous structures not only provide stronger contrast but also offer additional information to determine the percolation behavior of PLA domains. Three distinctive regions are then identified from the TEM images. In the middle PLA content region ($0.4 \leq \omega_{PLA} \leq 0.6$), disordered co-continuous nanostructures with characteristic length in the range of 20 – 30 nm are observed. In the low PLA content region ($\omega_{PLA} \leq 0.35$), a few bright porous nanostructures are randomly dispersed in the dark PS matrix, indicating PLA domains do not form percolated nanostructures even in ≈ 100 nm microtomed thin films. In high PLA content region ($\omega_{PLA} \geq 0.65$), removal of PLA domain generates pores but leads to larger length scale structures (> 100 nm) due to pore collapse. Although collapse of porous structures does not preserve the PS matrix, we can still observe some ordered lamellar nanostructures from TEM images. Porous nanostructures generated from removing PLA domains are more clearly imaged by scanning electron microscopy (SEM), as shown in Figure 42. For porous sample fabricated from $L\_S_{5k}L_{5k}$ – 65, locally organized PS structures among much larger domains (> 100 nm) are observed to form lamellar morphologies, corresponding to the partially preserved nanostructures in as prepared MBCs; however in the middle region ($0.4 \leq \omega_{PLA} \leq 0.6$), uniform co-

continuous nanoporous PS with well-defined characteristic length can be prepared. Compared to RECNs composed of the same strands, MBCs greatly benefit from the high processablity due to relative low M (< 20 kg/mol), while still maintaining a reasonably wide co-continuous window.
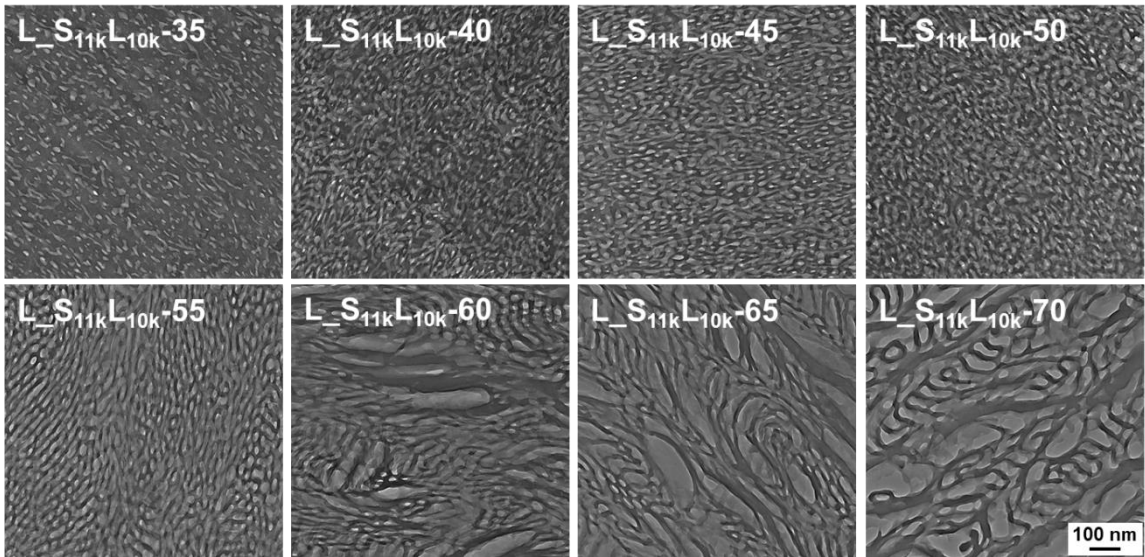
Figure 43. TEM images of porous PS by selectively removing PLA domains within PS/PLA MBCs $L\_S_{11k}L_{10k}$ with different PLA weight fractions (n = 3 − 4, Đ = 1.8 − 2.1). Dark regions are PS domains and bright regions are pores.
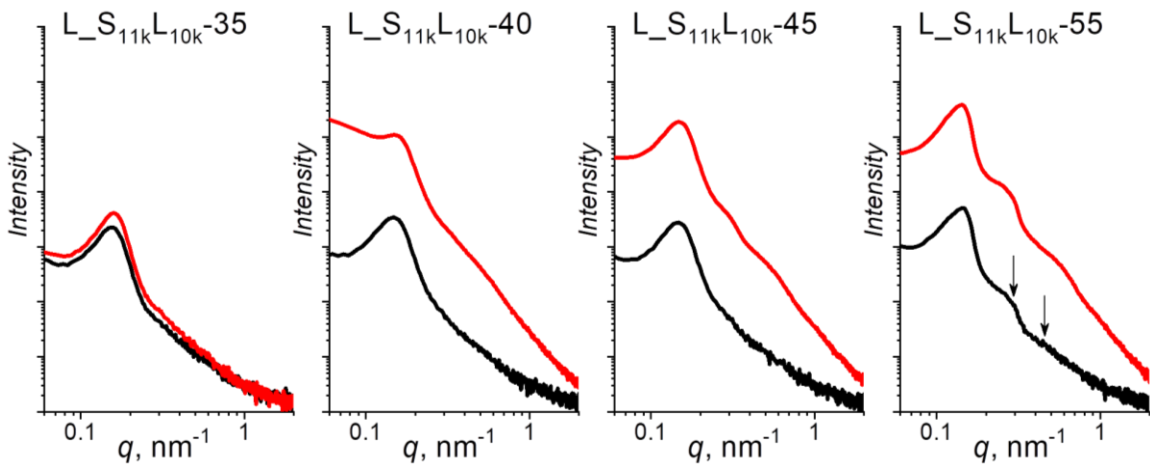
Figure 44. SAXS patterns of $L\_S_{11k}L_{10k}$ with different PLA weight fraction. Black: before etching. Red: after etching.

We next increase the strand length and consider the effect of segregation strength by doubling the molecular weight of both PS and PLA precursors to M_n =

11 kg/mol and 10 kg/mol, respectively. Similarly, step polymerization using di-SH as the chain extender leads to randomly linked linear MBCs, $L\_S_{11k}L_{10k}$, with M_n in the range of $35 - 43$ kg/mol. Compared to $L\_S_{5k}L_{5k}$, $L\_S_{11k}L_{10k}$ also converts to average block number $n = 3 - 4$ with similarly broad distributions of chain length $Đ = 1.8 - 2.1$. Unsurprisingly, as the PLA content is increased from $\omega_{PLA} = 0.35$ to 0.7 in Figure 43, the microphase separated structures evolve from dispersed PLA domains, to a disordered co-continuous morphology, and finally to ordered cylindrical and lamella-like structure. While the trend is more or less the same as MBCs with lower strand M, the transition occurs at different ω_{PLA}. For example, TEM image of $L\_S_{11k}L_{10k} - 40$ indicates well connected nanostructures, but its SAXS pattern (Figure 44) show substantially different scattering profiles before and after etching PLA domains, suggesting incomplete percolation of PLA domains. Indeed, gravimetric result demonstrates that only 50% of PLA domains are etched in alkaline solution, confirming the partial percolation. In the middle region, $L\_S_{11k}L_{10k} - 45$ and 50 show similar co-continuous morphologies as $L\_S_{5k}L_{5k}$ in the same composition region but possess larger $d = 43 - 45$ nm, as confirmed by TEM and SAXS; however, $L\_S_{11k}L_{10k} - 55$ displays a periodic nanostructured morphology. From 2D TEM images, we are able to identify packed cylindrical and perforated lamellae structures with a characteristic length of ~ 40 nm. As seen in Figure 44, SAXS pattern of $L\_S_{11k}L_{10k} - 55$ shows a clear and broad primary peak ($d = 2\pi/q^* = 43$ nm) with two higher order peaks denoted by arrows. Although the broad higher order peaks complicate the analysis, they are consistent with ordered nanostructures observed in TEM images. As ω_{PLA} is

increased to 0.6 or higher, lamella-like nanostructures are observed for $L\_S_{11k}L_{10k}$ – 60, 65 and 70 with increased characteristic length d = 42, 46 and 57 nm. Interestingly, the critical ω_{PLA} at which the nanostructure transitions from a disordered co-continuous to an ordered morphology decreases as the strand M increases. At the same time, doubling the strand M also increases the critical ω_{PLA} at which nanostructures with dispersed or partially branched PLA domains transition to a disordered co-continuous morphology. As a result, $L\_S_{11k}L_{10k}$ occupies a narrower composition window (0.45 ≤ ω_{PLA} ≤ 0.5) than $L\_S_{5k}L_{5k}$ (0.4 ≤ ω_{PLA} ≤ 0.6) with co-continuous nanostructures.
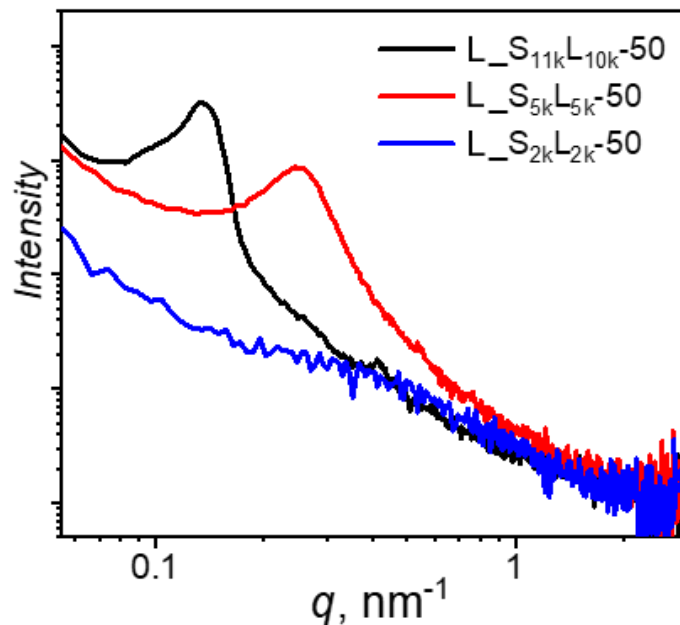
Figure 45. SAXS data for PS/PLA MBCs (ω_{PLA} = 0.5) with different strands M, representing different segregation strength $\chi(N_{PS} + N_{PLA})$ = 6, 15, 30, respectively.

Noticeably, a distinctive SAXS pattern with a weak and broad scattering peak is observed for MBCs with the smallest strand M (2 kg/mol), as seen in Figure 45, indicating weakly microphase separated or phase mixed morphology. Gravimetric measurement also shows less than 1% of weight loss, revealing that

there is PLA chains not accessible to alkaline solution, therefore we classify

$L\_S_{2k}L_{2k}$ as phase mixed copolymer.
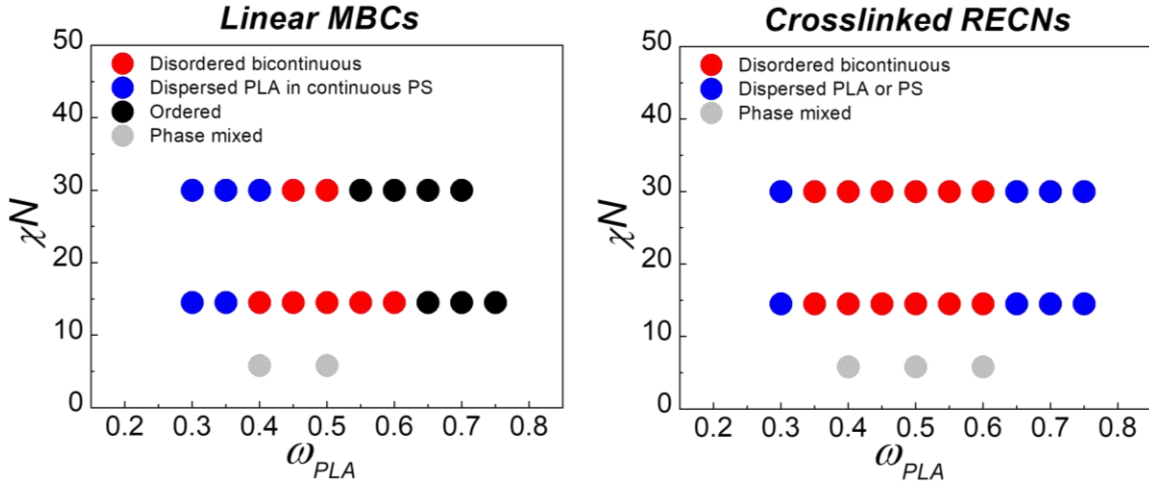
Figure 46. Phase diagrams of linear multi block copolymers (MBCs) and randomly end-linked copolymer networks (RECNs) with symmetric strand M ($M_{n, PS} \approx M_{n, PLA}$). RECNs phase diagram is discussed in chapter 3.

Using a Flory-Huggins parameter of $\chi = 0.12$ at an annealing temperature of 150 °C,[62] the segregation strength $\chi(N_{PS} + N_{PLA}) = 6$, 15 and 30 are calculated for $L\_S_{2k}L_{2k}$, $L\_S_{5k}L_{5k}$ and $L\_S_{11k}L_{10k}$, from which we construct a phase diagram describing the behavior of MBCs with symmetric strand M ($M_{n, PS} \approx M_{n, PLA}$), as shown in Figure 46. First, there is a critical microphase separation transition (MST), below which the segregation strength between PS and PLA is not strong enough to drive evident microphase separation, and above which MBCs self-assemble into various nanostructures as a function of M and ω_{PLA}. As expected, in the middle of the phase diagram, both PS and PLA phases percolate through the materials and develop to disordered co-continuous nanostructures. On the left, PLA domains form dispersed nanostructures surrounded by a continuous PS matrix, while on the right ordered morphologies

with periodic structures are observed. The disordered co-continuous window widens substantially as the segregation strength decreases from 30 to 15, indicating that weak segregation strength close to MST drives formation of a disordered morphology. We attribute this effect to strong concentration fluctuations near the MST. As understood in diblock copolymers, concentration fluctuation will shift the order-disorder transition (ODT) to larger χN in the phase diagram, leaving a window between $\chi N_{(ODT)}$ and $\chi N_{(MST)}$, within which disordered morphology is stabilized due to concentration fluctuation.[159–161] Analogous to diblock copolymers, this concentration fluctuation effect is also observed in our MBCs. Specifically, we interpret that $L\_S_{5k}L_{5k}$ has a segregation strength slightly higher than $\chi N_{(MST)}$ but lower than $\chi N_{(ODT)}$, therefore showing a pronounced concentration fluctuation effect and stabilizing disordered co-continuous naostructures. However, well above $\chi N_{(ODT)}$, $L\_S_{11k}L_{10k}$ most likely forms ordered nanostructures due to the diminished concentration fluctuation. Below $\chi N_{(MST)}$, $L\_S_{2k}L_{2k}$ stays as homogeneous phase mixed state, only showing very weak scattering contrast in SAXS. Experimentally, disordered co-continuous morphologies are also reported to exist within other triblock or multiblock copolymers with weak segregation strength.[88,90,162,163].

Moreover, polydispersity tends to relieve the packing frustration on curved interfaces, therefore promoting domains to form percolated structures.[88–93] Although it has also been suggested that large n in MBCs is generally required to frustrate the formation of regular periodic structures (it does explain the observation of cylindrical and lamellae-like morphology at high PLA

content[138,164]), we believe in our case the random block sequence, polydispersity and concentration fluctuation near MST all together promote MBCs to form disordered co-continuous nanostrucutures even with low n (< 5).[165] Overall, these arguments explain why our MBCs with low block number show wide co-continuous window near but not away from MST, while sometimes also form periodic structures at high PLA content.

In comparison, crosslinked RECNs exhibit a wider co-continuous window, which shows little dependence on segregation strength, as seen in Figure 46. Moreover, periodic and ordered morphologies are not observed across the entire composition window in RECNs. To clarify, linear MBCs and RECNs are prepared using the same polymer precursor and linking chemistry under the same reaction condition. Therefore, we attribute the stronger tendency in RECNs to form disordered co-continuous structure as the highly crosslinked architectures, where the 4-arm junctions frustrate the formation of ordered structures, due to the high elastic energy penalty in polymer chains with both ends confined; however, the narrower co-continuous window in MBCs is at least in part offset by their enhanced processability. For example, the SEM image in Figure 47 shows a thin film of nanoporous PS fabricated from MBCs by spin coating, which is not possible for crosslinked RECNs. Although further experiments are required, we speculate that with random block sequence and high polydispersity, increasing the number of blocks (n) in linear MBCs will tend to further diminish long-range order and organize the nanostructures into disordered and co-continuous morphologies.
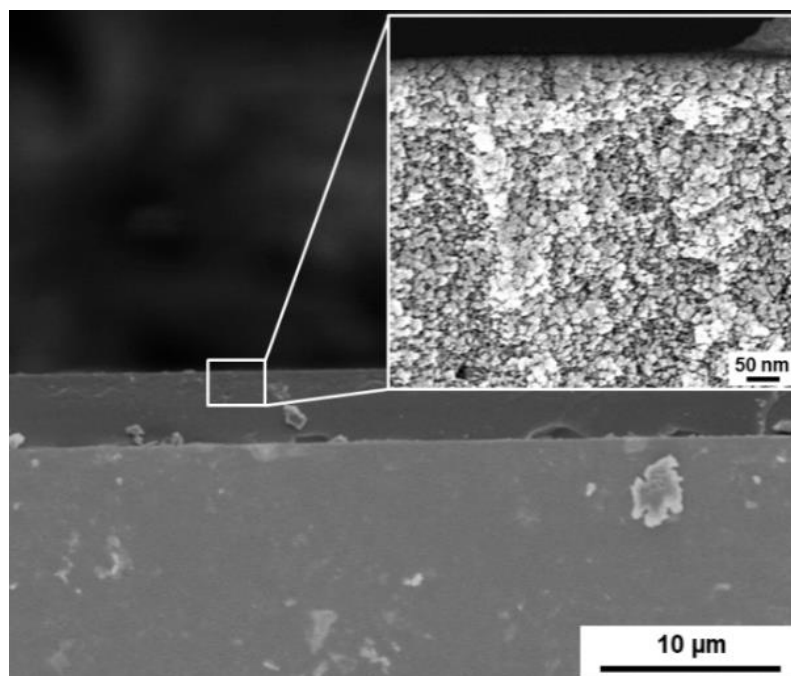
Figure 47. SEM image of 4 *μ*m thick nanoporous PS monoliths fabricated by spin-coating *L_S$_{5k}$L$_{5k}$* – 50 from DMF, followed by removing PLA in alkaline solution.

5.3.2 Branched Multiblock Copolymers

Adding branched structures to MBCs provides another opportunity to access disordered nanostructures. For example, Leibler and co-workers have demonstrated the formation of thermodynamically stable co-continuous morphologies using randomly grafted copolymers with inherent polydispersed strands.[166,167] In addition to block length dispersity and random block sequence in linear MBCs, different junctions in branched MBCs brings dispersity in interfacial curvature, favoring the formation of disordered nanostructures. This junction related interface curvature dispersity concept is discussed in chapter 3.2.4. Here, branched MBCs are synthesized from telechelic PS and PLA using a mixture of di-thiol and tri-thiol as chain extender and branching unit, respectively, and are named as *B_S$_{MPS}$L$_{MPLA}$* – *X.* We control the branching fraction (tri-SH * 3)

/ (tri-SH * 3 + di-SH * 2) = 0.5 and stoichiometric SH / acrylate = 0.7, not only to achieve branched structures, but also to make sure that reaction is always below critical gelation point even with 100 percent conversion. Similar to linear MBCs $L\_S_{5k}L_{5k}$, branched MBCs $B\_S_{5k}L_{5k}$ composed of the same strands (5k/5k) also show a low number of blocks, n = 3 – 4, over the composition range from ω_{PLA} = 0.35 to 0.75, as seen in Figure 48. In this case, on average one or two branching strands is estimated for our branched MBCs.
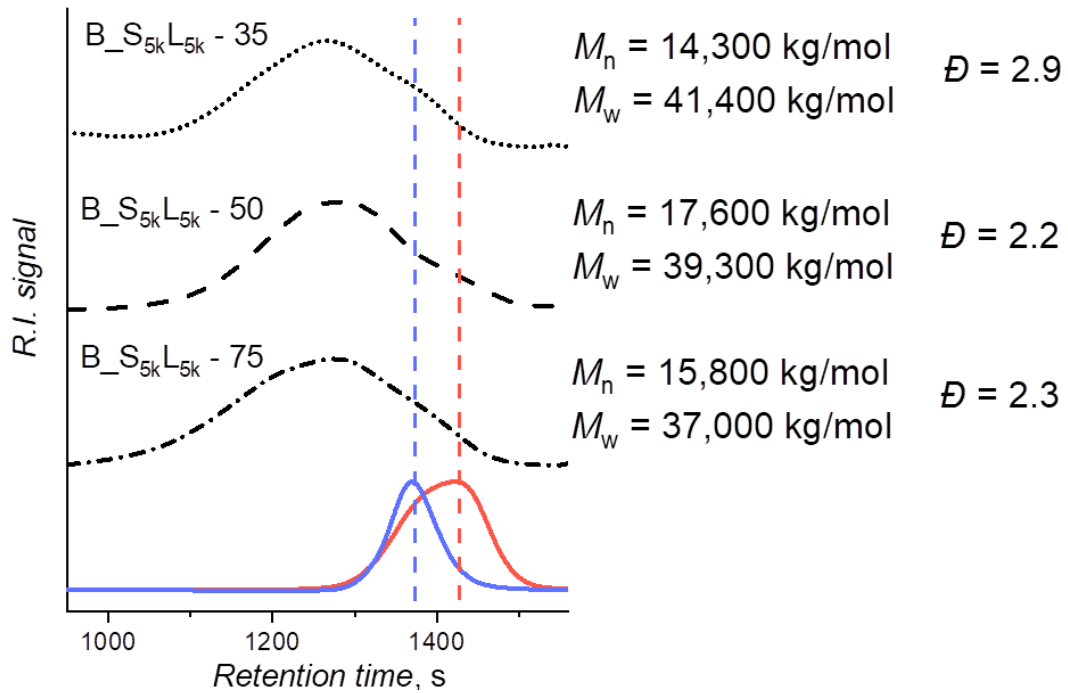
Figure 48. GPC traces of branched multiblock PS/PLA copolymers, $B\_S_{5k}L_{5k}$ – 35, 50 and 75 synthesized from di-acrylate functionalized telechelic PS (M_n = 5 kg/mol) and PLA (M_n = 5.5 kg/mol) precursors.

Slightly higher polydispersity (Đ = 2.1 – 2.9) is observed for $B\_S_{5k}L_{5k}$, while the scattering profiles shown in Figure 49 indicate a similar morphological structure. First, there are three distinctive regions: (1) dispersed PLA domains in a continuous PS matrix when ω_{PLA} ≤ 0.35; (2) co-continuous nanostructures when 0.4 ≤ ω_{PLA} ≤ 0.6; (3) ordered lamella-like morphologies when ω_{PLA} ≥ 0.65.

Second, we do not observe a qualitative difference between $L\_S_{5k}L_{5k}$ and $B\_S_{5k}L_{5k}$ in terms of the composition windows with co-continuous nanostructures. Indeed, Mays, et al. have reported that high branching density (> 5 branch points/chain) are generally required in branched PS/polyisoprene (PIP) to sufficiently frustrate the ordered morphology to form disordered nanostructures.[141,168,169] In this manner, it is not surprising that the low branching density (< 3) of branched MBCs in our case does not lead to differences in comparison to linear MBCs.
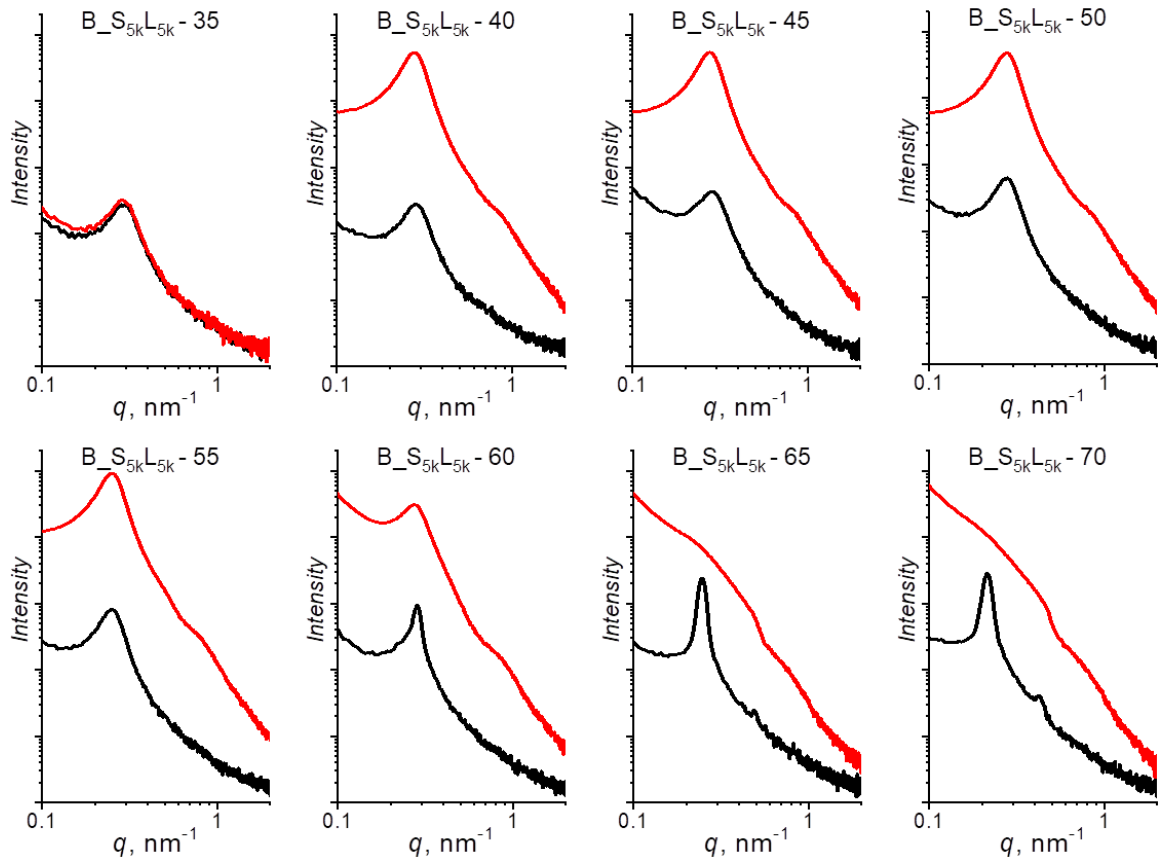
Figure 49. SAXS patterns of $B\_S_{5k}L_{5k}$ with different PLA weight fraction ($n = 3 - 4$, $Đ = 2.1 - 2.9$). Black: before etching. Red: after etching.

Although we have attempted to achieve MBCs with both high branching density and high molecular weight, further increase is again limited by the

imperfect telechelic structures (f < 2) and low efficiency of thiol-Michael reaction. This explains why we could not successfully synthesize branched MBCs with longer di-acrylate functional PS and PLA ($M_n \approx$ 10 kg/mol). To provide a more conclusive understanding of how branching affects the packing frustration and the resulting disordered morphology, we will advise some directions in section 5.3.
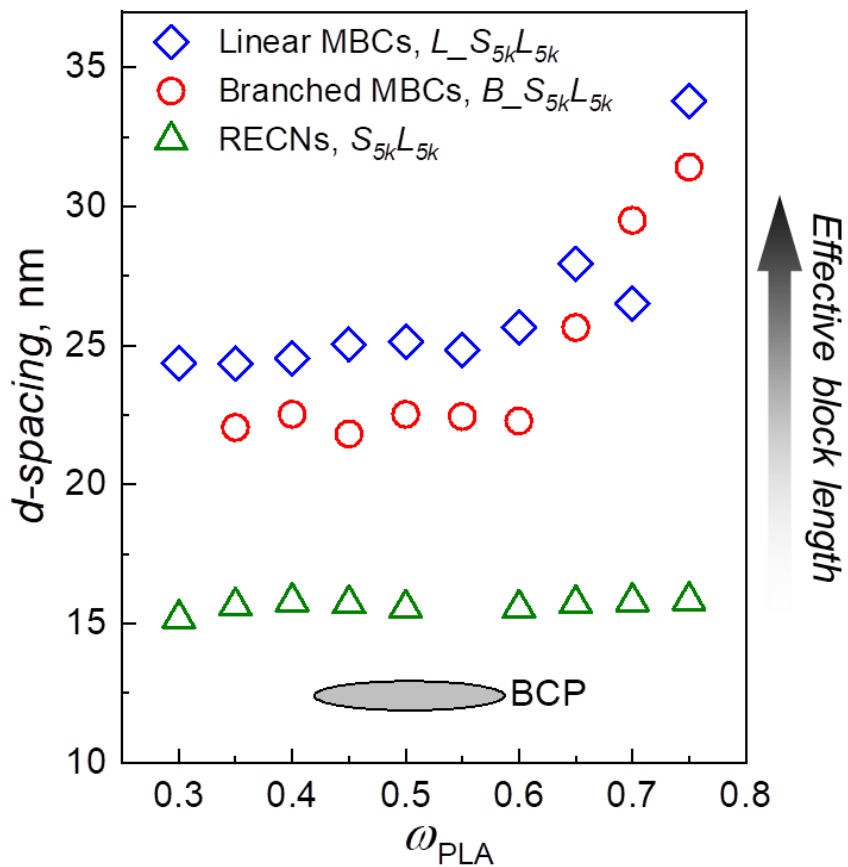
Figure 50. d-spacing of $L\_S_{5k}L_{5k}$, $B\_S_{5k}L_{5k}$ and RECNs_$S_{5k}L_{5k}$ as a function of PLA weight fraction. Domain spacing of diblock copolymers (BCP) with the same block length is also estimated and plotted based on literature experimental results.[62,170–172]

Finally, we examine the characteristic length (d spacing) of copolymers with different architectures, as shown in Figure 50. All samples, including linear

MBCs, branched MBCs and RECNs are constituted from the same blocks, but they exhibit distinctive characteristic sizes. Overall, three randomly linked copolymers with complex architectures show d spacing larger than that of diblock copolymers. This observation is rationalized by random block sequence in those copolymers, which increases the average effective block length, hence apparent d spacing.[165] Interestingly, both uncrosslinked MBCs have much larger d spacing than highly crosslinked RECNs due to the fact that crosslinked RECNs experience higher elastic energy penalty of stretching and have shorter effective block length (statistically, RECNs have half junctions with the same strands, while RECNs only have 1/8 of junctions with 4 same type of strands) .

5.3 Conclusion & Outlook

In this chapter, easily processable linear and branched MBCs have been synthesized using telechelic PS and PLA as precursors and characterized with GPC, SAXS, TEM and SEM. Although we can only achieve MBCs with the average number of blocks n = 3 – 4 because step polymerization is highly sensitive to the imperfect telechelic structures (functionality < 2) and low efficiency of thiol-Michael linking chemistry, the existence of random block sequence and high polydispersity $Đ$ ≈ 2 – 3 tends to frustrate the self-organization of regular periodic structures, therefore forming disordered co-continuous nanostructures. In addition, the pronounced concentration fluctuation near the MST further widens the composition window for disordered co-continuous morphologies. Although highly crosslinked RECNs provide a more

robust route to co-continuous nanostructures, the melt and solution processability of MBCs offers offsetting advantages.

As the effects of structural parameters of MBCs, including the number of blocks, block sequence, dispersity, and branching density, are still not fully explored, it will be important in future work to decouple these dimensions to elucidate the key design rules for generating co-continuous nanostructures. For example, click chemistry with high efficiency would help to achieve large block number in step polymerization, while living radical polymerization could provide another pathway to graft copolymers with controlled grafting density. Additionally, future studies on the effect of shear force on thin film morphology are not only important in terms of practical applications, but also interesting to help understand whether these disordered co-continuous nanostructures are thermodynamic stable or kinetically trapped.

Chapter 6

SUMMARY & FUTURE DIRECTIONS

This thesis aims to provide fundamental understandings of copolymer architectures designed to achieve desired co-continuous nanostructured materials with far-ranging applications. Our approach relies on microphase separation of copolymers with linear, branched and crosslinked architectures synthesized from telechelic polymers. The biggest advantage of this approach is the well-controlled and defined chemical parameters, strand length (M), strand polydispersity ($Đ$) and junction functionality (f), therefore providing some general and robust protocols to design co-continuous morphologies.

In chapter 2 – 4, we focused on the formation of disordered co-continuous nanostructures from randomly end-linked copolymer networks (RECNs) by crosslinking telechelic polystyrene (PS) and poly (D,L - Lactide) (PLA) with a multi-functional crosslinker in homogeneously mixed solution state, followed by solvent removal to introduce microphase separation. Building upon the gravimetric, mechanical and electron microscopic analysis, the nature of nanostructured morphologies within PS/PLA RECNs has been studied and characterized, and for the first time, a phase diagram is constructed describing the morphology behavior as a function of volume fraction and segregation strength (Chapter 3). Specifically, we highlighted a critical microphase separation transition ($6 < (\chi N)_{critical} < 12$), above which disordered cocontinuous nanostructures span over 30 vol% in the middle of the phase diagram with dispersed domains on the sides. Furthermore, we investigated the effects of

multi-dimensional parameters (M, strands asymmetry, $Đ$) on the morphology, including percolation thresholds and d-spacing. While replacing thiol-Michael with thiol-ene chemistry at the junction points offers an increase in the width of the co-continuous window by 15 vol% as the average f and f variability increase, we still lack a clear understanding of the effects of f on the interfacial curvature and the formation of co-continuous nanostructures. For the future, it will be interesting to systematically study the effects of f by replacing tetra-thiol with tri-, penta- or hexa- thiol. Additionally, it will be important to incorporate simulations to help understand the relationships among f, volume fraction, interfacial curvature, and morphology. TEM tomography of co-continuous PS/PLA has been shown to provide a direct route to determine real-space interfacial curvatures and domain sizes. Comparing these results with simulation studies hopefully will offer more insights into the design of crosslinked copolymer networks. Although we have summarized a gradual morphology evolution from phase mixed to weakly phase separated, and finally to well phase separated from a "property viewpoint" segregation strength is increased, a clearer evaluation of the difference between concentration fluctuation and disordered phase separation is necessary. To understand this point, X-ray photon correlation spectroscopy can be used to characterize the relaxation time at a certain length scale, providing a way to examine the dynamic morphology behaviors.[173,174]

The ability of the PLA phase within microphase separated RECNs to be selectively removed by an aqueous basic solution while the PS phase is essentially impenetrable, provided a robust mean to fabricate interconnected

nanoporous materials over a wide range of compositions (chapter 2). Pore sizes were tuned simply by adjusting the designed molecular weight of precursors, in agreement with the scaling relationship $d \sim M_n^{0.5}$, as predicted by de Gennes for randomly cross-linked blends[38]; however, the segregation strength necessary to achieve microphase separation limited the minimum pore size to 5 – 6 nm, corresponding to a strand molecular weight of ≈ 3 kg/mol. While future experiments are required to evaluate the performance of these mesoporous materials as ultrafiltration membranes, further reduction of pore size into the micropore range (< 2 nm) will be very exciting because of their fully interconnect porous structures and high surface area, typically 300 – 1500 m^2/g. One strategy will be the use of B-PLA-B triblock copolymer replacing PLA strands in the preparation of RECNs. While the long B blocks trigger microphase separation, the short PLA midblock in domain B would serve as the precursor for a microporous structure. Although B-PLA-B triblock copolymers will not phase separate in the bulk state, we expect the microphase separation between domain A and B will force the B strands moving towards the surface of domain A, leaving PLA blocks in the center, therefore generating distinctive A and B domains. Another strategy will be to use copolymer system with high χ, for example, PDMS and PLA, where χ ≈ 1.[175] Moreover, as this thesis focuses on a material system based on PS and PLA, the porous PS materials generated are fragile, and cannot be used for further mechanical testing or practical applications. Replacing PS strands with high performance engineering materials, such as

polycarbonate and polysulfone, could dramatically improve the mechanical and thermal properties for practical applications.

Another notable detail about the RECNs studied is that removal of PLA domains reduces the crosslinking density, pushing the porous PS below its gel point. Taking advantage of this fact, this porous PS can be used as a sacrificial template to fabricate co-continuous inorganic materials or polymerized ionic liquids (PILs) for a variety of applications in separations, catalysis, sensing, and energy storage.[176–179] While disordered bicontinuous morphology in RECNs is comparable to double gyroid morphology in BCP (both form two independent interconnected channels, confirmed by TEM tomogram), one big advantage of RECNs is the wide composition window, allowing us to prepare bicontinuous nanoporous materials with corresponding tunable porosities. Additionally, we can also potentially prepare porous membrane with pore size gradually changing along the film thickness. To achieve this, we will need to take advantage of the diffusion of short and long strands in two solutions before complete mixing. If we are able to kinetically trap the diffusion process using a fast end-linking chemistry (ie., photo initiated thiol-ene chemistry), RECNs with gradually changed strands length across the solution can be fabricated.

In chapter 4, we established the fabrication of highly oriented co-continuous structures through uniaxial stretching above the glass transition temperatures, followed by quenching to room temperature. The morphology evolution as a function of strain revealed a two-step process in which the domains initially undergo non-affine stretching, followed by domain rotation,

90

accompanied by the rearrangement of interfaces during deformation. Orientation at the nanometer scales was then found to yield substantial improvements in tensile strength, toughness, and stiffness. However, we still lack a fully understanding on the higher yield stress and stiffness of oriented RECNs than those of oriented single component networks. As we speculate this effect as the high chain orientation resulted from the oriented microphase separated structure in RECNs, polarized IR can provide further characterization of polymer chain alignments.[127] Overall, this work introduced a unique and robust method to achieve highly anisotropic nanostructures with complete continuity, and future work has the potential to expand this fundamental understanding to various practical applications, including photonics, energy absorption, and ion transport.

Lastly, in chapter 5, we provided an understanding on the microphase separation behavior of multi-block copolymers (MBCs), prepared through step polymerization of telechelic PS and PLA. Accordingly, we have discovered a strong dependence of the width of the co-continuous window on segregation strength, and the width tended to span over 20 – 25 vol% only when concentration fluctuation dominates microphase separation close to MST. So far, the interplay of many chemical parameters, including number of blocks, block sequence, polydispersity and branching structures, still complicate the relationship between copolymer architectures and morphological behaviors. Particularly, more efforts, such as simulation studies, are needed to decouple the effects of those multiple variables, in order to create key rules of designing disordered co-continuous nanostructures from microphase separated MBCs. In

addition, more precise chemistry, such as living radical polymerization,[138,146] and efficient end-linking reactions[139,154,169] are required to create linear and branched MBCs with precisely-defined parameters. As for continuing to use telechelic macromolecules for the preparation of more complicated polymer architectures, it will also be necessary to explore new chemistries to customize and synthesize functional polymers.[180,181].

BIBLIOGRAPHY

[1]   Rubinstein M and Colby R H 2003 *Polymer Physics* vol 23 (New York: Oxford University Press)

[2]   Flory P J 1942 Thermodynamics of High Polymer Solutions | Browse - Journal of Chemical Physics *J. Chem. Phys.* **51** 51–61

[3]   Huggins M L 1941 Solutions of Long Chain Compounds *J. Chem. Phys.* **9** 440

[4]   Balazs A C, Emrick T and Russell T P 2013 Nanoparticle Polymer Composites : Where Two Small Worlds Meet *Science (80-.).* **314** 1107–10

[5]   Bates F S and Fredrickson G H 1999 Block Copolymers—Designer Soft Materials *Phys. Today* **52** 32

[6]   Cochran E W, Garcia-Cervera C J and Fredrickson G H 2006 Stability of the gyroid phase in diblock copolymers at strong segregation *Macromolecules* **39** 2449–51

[7]   Hickner M A 2010 Ion-containing polymers : new energy & clean water New generations of materials are being sought as solid-state *Mater. Today* **13** 34–41

[8]   Etacheri V, Marom R, Elazari R, Salitra G and Aurbach D 2011 Challenges in the development of advanced Li-ion batteries: A review *Energy Environ. Sci.* **4** 3243–62

[9]   Nicolson P C and Vogt J 2001 Soft contact lens polymers: An evolution *Biomaterials* **22** 3273–83

[10]   Huang Y, Kramer E J, Heeger A J and Bazan G C 2014 Bulk heterojunction solar cells: Morphology and performance relationships *Chem. Rev.* **114** 7006–43

[11]   Dair B J, Honeker C C, Alward D B, Avgeropoulos A, Hadjichristidis N, Fetters L J, Capel M and Thomas E L 1999 Mechanical properties and deformation behavior of the double gyroid phase in unoriented thermoplastic elastomers *Macromolecules* **32** 8145–52

[12]   Guillen G R, Pan Y, Li M and Hoek E M V 2011 Preparation and characterization of membranes formed by nonsolvent induced phase separation: A review *Ind. Eng. Chem. Res.* **50** 3798–817

[13]   Schüth F 2005 Engineered Porous Catalytic Materials *Annu. Rev. Mater. Res.* **35** 209–38

[14]   Bates F S and Fredrickson G H 1999 Block Copolymers—Designer Soft

Materials *Phys. Today* **52** 32

[15]   Erdodi G and Kennedy J P 2006 Amphiphilic conetworks: Definition, synthesis, applications *Prog. Polym. Sci.* **31** 1–18

[16]   Sperling L H and Mishra V 1996 The current status of interpenetrating polymer networks *Polym. Adv. Technol.* **7** 197–208

[17]   Lee J C 1999 Polymerization-induced phase separation. *Phys. Rev. E* **60** 1930–5

[18]   Bruns N, Scherble J, Hartmann L, Thomann R, Iván B, Mülhaupt R and Tiller J C 2005 Nanophase separated amphiphilic conetwork coatings and membranes *Macromolecules* **38** 2431–8

[19]   Bruns N and Tiller J C 2005 Amphiphilic network as nanoreactor for enzymes in organic solvents *Nano Lett.* **5** 45–8

[20]   Mu R 2001 Formation of CdS Nanoclusters in Phase-Separated Poly (2-hydroxyethyl methacrylate) -l-polyisobutylene Amphiphilic *Polymer (Guildf).* 1429–36

[21]   Guzman G, Nugay T, Nugay I, Nugay N, Kennedy J and Cakmak M 2015 High Strength Bimodal Amphiphilic Conetworks for Immunoisolation Membranes: Synthesis, Characterization, and Properties *Macromolecules* **48** 6251–62

[22]   Gitsov I and Zhu C 2003 Novel functionally grafted pseudo-semi-interpenetrating networks constructed by reactive linear-dendritic copolymers *J. Am. Chem. Soc.* **125** 11228–34

[23]   Kepola E J, Loizou E, Patrickios C S, Leontidis E, Voutouri C, Stylianopoulos T, Schweins R, Gradzielski M, Krumm C, Tiller J C, Kushnir M and Wesdemiotis C 2015 Amphiphilic Polymer Conetworks Based on End-Linked "core-First" Star Block Copolymers: Structure Formation with Long-Range Order *ACS Macro Lett.* **4** 1163–8

[24]   Dinu M V, Perju M M and Drăgan E S 2011 Porous semi-interpenetrating hydrogel networks based on dextran and polyacrylamide with superfast responsiveness *Macromol. Chem. Phys.* **212** 240–51

[25]   Gong J P, Katsuyama Y, Kurokawa T and Osada Y 2003 Double-network hydrogels with extremely high mechanical strength *Adv. Mater.* **15** 1155–8

[26]   Nevissas V, Widmaier J M and Meyer G C 1988 Effect of crosslink density and internetwork grafting on the transparency of polyurethane/polystyrene interpenetrating polymer networks *J. Appl. Polym. Sci.* **36** 1467–73

[27]   An J H, Fernandez A M and Sperling L H 1987 Development of multiphase morphology in poly(cross-butadiene)-inier-poly(cross-styrene)

interpenetrating polymer networks *Macromolecules* **20** 191–3

[28] Lal J, Widmaier J M, Bastide J and Boue F 1994 Determination of an Interpenetrating Network Structure by Small-Angle Neutron-Scattering *Macromolecules* **27** 6443–51

[29] Inoue T 1995 Reaction-induced phase decomposition in polymer blends *Prog. Polym. Sci.* **20** 119–53

[30] Dean J M, Verghese N E, Pham H Q and Bates F S 2003 Nanostructure toughened epoxy resins *Macromolecules* **36** 9267–70

[31] Hillmyer M A, Lipic P M, Hajduk D A, Almdal K and Bates F S 1997 Self-assembly and polymerization of epoxy resin-amphiphilic block copolymer nanocomposites *J. Am. Chem. Soc.* **119** 2749–50

[32] Ratna D and Simon G . 2001 Thermomechanical properties and morphology of blends of a hydroxy-functionalized hyperbranched polymer and epoxy resin *Polymer (Guildf).* **42** 8833–9

[33] Scott R L 1949 The Thermodynamics of High Polymer Solutions. V. Phase Equilibria in the Ternary System: Polymer 1—Polymer 2—Solvent *J. Chem. Phys.* **17** 279

[34] de Gennes P G 1978 Scaling Laws for Incompatible Polymer Solutions *J. Polym. Sci. Part B Polym. Phys.* **16** 1883–5

[35] Fredrickson G H and Leibler L 1989 Theory of block copolymer solutions: nonselective good solvents *Macromolecules* **22** 1238–50

[36] Lodge T P, Hanley K J, Pudil B and Alahapperuma V 2003 Phase behavior of block copolymers in a neutral solvent *Macromolecules* **36** 816–22

[37] Lodge T P, Pan C, Jin X, Liu Z, Zhao J, Maurer W W and Bates F S 1995 Failure of the dilution approximation in block copolymer solutions *J. Polym. Sci. Part B Polym. Phys.* **33** 2289–93

[38] de Gennes P G 1979 Effect of cross-links on a mixture of polymers *J. Phys. Lettres* **40** 69–72

[39] Briber R M and Bauer B J 1988 Effect of Cross-Links on the Phase Separation Behavior of a Miscible Polymer Blend *Macromolecules* **21** 3296–303

[40] Benmouna M, Vilgis T A, Daoud M and Benhamou M 1994 Scattering and Phase Behavior of Cross-Linked Blends *Macromolecules* **27** 1172–6

[41] Klopper A V., Svaneborg C and Everaers R 2009 Microphase separation in cross-linked polymer blends : EEEfficient replica RPA post-processing of

simulation data for homopolymer networks *Eur. Phys. J. E* **28** 89–96

[42] Lay S, Sommer J U and Blumen A 2000 Monte Carlo study of the microphase separation of cross-linked polymer blends *J. Chem. Phys.* **113** 11355

[43] Erdodi G and Kennedy J P 2005 Ideal tetrafunctional amphiphilic PEG/PDMS conetworks by a dual-purpose extender/crosslinker. II. Characterization and properties of water-swollen membranes *J. Polym. Sci. Part A Polym. Chem.* **43** 4965–71

[44] Cui J, Lackey M A, Madkour A E, Saffer E M, Griffin D M, Bhatia S R, Crosby A J and Tew G N 2012 Synthetically Simple, Highly Resilient Hydrogels *Biomacromolecules* **13** 584–588

[45] Erdodi G and Ivan B 2004 Novel Amphiphilic Conetworks Composed of Telechelic Poly(ethylene oxide) and Three-Arm Star Polyisobutylene *Chem. Mater.* **16** 959–62

[46] Walker C N, Versek C, Touminen M and Tew G N 2012 Tunable networks from thiolene chemistry for lithium ion conduction *ACS Macro Lett.* **1** 737–41

[47] Walker C N, Bryson K C, Hayward R C and Tew G N 2014 Wide bicontinuous compositional windows from Co-networks made with telechelic macromonomers *ACS Nano* **8** 12376–85

[48] Hsueh H-Y, Yao C-T and Ho R-M 2015 Well-ordered nanohybrids and nanoporous materials from gyroid block copolymer templates *Chem. Soc. Rev.* **44** 1974–2018

[49] Urbas A M, Maldovan M, DeRege P and Thomas E L 2002 Bicontinuous cubic block copolymer photonic crystals *Adv. Mater.* **14** 1850–3

[50] Chan V Z H, Hoffman J, Lee V Y, Iatrou H, Avgeropoulos A, Hadjichristidis N, Miller R D and Thomas E L 1999 Ordered bicontinuous nanoporous and nanorelief ceramic films from self assembling polymer precursors *Science (80-.).* **286** 1716–9

[51] Ndoni S, Vigild M E and Berg R H 2003 Nanoporous Materials with Spherical and Gyroid Cavities Created by Quantitative Etching of Polydimethylsiloxane in Polystyrene-Polydimethylsiloxane Block Copolymers *J. Am. Chem. Soc.* **125** 13366–7

[52] Pitet L M, Amendt M A and Hillmyer M A 2010 Nanoporous linear polyethylene from a block polymer precursor *J. Am. Chem. Soc.* **132** 8230–1

[53] Li L, Shen X, Hong S W, Hayward R C and Russell T P 2012 Fabrication of Co-continuous nanostructured and porous polymer membranes:

Spinodal decomposition of homopolymer and random copolymer blends *Angew. Chemie - Int. Ed.* **51** 4089–94

[54]   Sai H, Tan K W, Hur K, Asenath-Smith E, Hovden R, Jiang Y, Riccio M, Muller D A, Elser V, Estroff L A, Gruner S M and Wiesner U 2013 Hierarchical Porous Polymer Scaffolds from Block Copolymers *Science (80-.).* **341** 530–4

[55]   Samitsu S, Zhang R, Peng X, Krishnan M R, Fujii Y and Ichinose I 2013 Flash freezing route to mesoporous polymer nanofibre networks *Nat. Commun.* **4** 1–7

[56]   Nakanishi K and Tanaka N 2007 Sol – Gel with Phase Separation: Hierarchically Porous Materials Optimized for High-Performance Liquid Chromatography Separations *Acc. Chem. Res.* **40** 863–73

[57]   Chen Y, Yuan D and Xu C 2014 Dynamically vulcanized biobased polylactide/natural rubber blend material with continuous cross-linked rubber phase *ACS Appl. Mater. Interfaces* **6** 3811–6

[58]   Seo M and Hillmyer M A 2012 Reticulated Nanoporous Polymers by Controlled Polymerization-Induced Microphase Separation *Science* **336** 1422–5

[59]   Saba S a., Mousavi M P S, Bühlmann P and Hillmyer M a. 2015 Hierarchically Porous Polymer Monoliths by Combining Controlled Macro- and Microphase Separation *J. Am. Chem. Soc.* 150710134337004

[60]   Seo M, Amendt M A and Hillmyer M A 2011 Cross-linked nanoporous materials from reactive and multifunctional block polymers *Macromolecules* **44** 9310–8

[61]   Iván B, Almdal K, Mortensen K, Johannsen I and Kops J 2001 Synthesis , Characterization , and Structural Investigations of Poly (ethyl acrylate) -l-polyisobutylene Bicomponent Conetwork *Macromolecules* **34** 1579–85

[62]   Zalusky A S, Olayo-valles R, Wolf J H and Hillmyer M a 2002 Ordered Nanoporous Polymers from Polystyrene - Polylactide Block Copolymers *J. Am. Chem. Soc.* 12761–73

[63]   Kremer J R, Mastronarde D N and Mcintosh J R 1996 Computer Visualization of Three-Dimensional Image Data Using IMOD *J. Struct. Biol.* **116** 71–6

[64]   Pettersen E F, Goddard T D, Huang C C, Couch G S, Greenblatt D M, Meng E C and Ferrin T E 2004 UCSF Chimera - A visualization system for exploratory research and analysis *J. Comput. Chem.* **25** 1605–12

[65]   Dougherty R and Kunzelmann K-H 2007 Computing Local Thickness of 3D Structures with ImageJ *Microsc. Microanal.* **13** 1678–9

[66]   Price S C, Ren X, Jackson A C, Ye Y, Elabd Y a. and Beyer F L 2013 Bicontinuous Alkaline Fuel Cell Membranes from Strongly Self-Segregating Block Copolymers *Macromolecules* **46** 7332–40

[67]   Bates F S, Wiltzius P, Bates F S, Wiltzius P, Laboratories T B and Hill M 1989 Spinodal decomposition of a symmetric critical mixture of deuterated and protonated polymer Spinodal decomposition of a symmetric critical mixture of deuterated and protonated polymer *J. Chem. Phys.* **3258**

[68]   Vonk C G, Billman J F and Kaler E W 1988 Small angle scattering of bicontinuous structures in microemulsions *J. Chem. Phys.* **88** 3970–5

[69]   Hashimoto T, Jinnai H, Nishikawa Y, Koga T and Takenaka M 1997 Sponge-like structures and their Gaussian curvatures in polymer mixtures and microemulsions *Prog. Colloid Polym. Sci.* **106** 118–26

[70]   Barrett E P, Joyner L G and Halenda P P 1951 The Determination of Pore Volume and Area Distributions in Porous Substances. I. Computations from Nitrogen Isotherms *J. Am. Chem. Soc.* **73** 373–80

[71]   Brunauer S, Emmett P H and Teller E 1938 Adsorption of Gases in Multimolecular Layers *J. Am. Chem. Soc.* **60** 309–19

[72]   Hillmyer M A 2005 Nanoporous materials from block copolymer precursors *Adv. Polym. Sci.* **190** 137–81

[73]   Read D, Brereton M, Mcleish T, Read D, Brereton M, Theory T M, Transition O P and Id H A L 1995 Theory of the Order - Disorder Phase Transition in Cross-Linked Polymer Blends

[74]   Lodge T P 2003 Block copolymers: Past successes and future challenges *Macromol. Chem. Phys.* **204** 265–73

[75]   Search H, Journals C, Contact A, Iopscience M and Address I P 2003 Nanostructure fabrication using block copolymers **39**

[76]   Lang X, Hirata A, Fujita T and Chen M 2011 Nanoporous metal/oxide hybrid electrodes for electrochemical supercapacitors *Nat. Nanotechnol.* **6** 232–6

[77]   Yan M, Wang F, Han C, Ma X, Xu X, An Q, Xu L, Niu C, Zhao Y, Tian X, Hu P, Wu H and Mai L 2013 Nanowire templated semihollow bicontinuous graphene scrolls: Designed construction, mechanism, and enhanced energy storage performance *J. Am. Chem. Soc.* **135** 18176–82

[78]   Bates F S, Maurer W W, Lipic P M, Hillmyer M A, Almdal K, Mortensen K, Fredrickson G H and Lodge T P 1997 Polymeric bicontinuous microemulsions *Phys. Rev. Lett.* **79** 849–52

[79]   Zeng D, Ribbe A and Hayward R C 2017 Anisotropic and Interconnected

Nanoporous Materials from Randomly End-Linked Copolymer Networks *Macromolecules* **50** 4668–76

[80] Zeng D, Ribbe A and Hayward R C 2018 Stress-induced Orientation of Co-continuous Nanostructures within Randomly End-linked Copolymer Networks *ACS Macro Lett.*

[81] Msick B, Benmouna M and Vilgis T A 1995 Scattered intensity by a cross-linked polymer blend **76** 67–76

[82] Affdl J H and Kardos J L 1976 The Halpin-Tsai Equations: a review *Polym. Eng. Sci.* **16** 344–52

[83] McLeod K R and Tew G N 2017 Microphase-Separated Thiol-Ene Conetworks from Telechelic Macromonomers with Asymmetric Molecular Weights *Macromolecules* **50** 8042–7

[84] Grason G M and Kamien R D 2004 Interfaces in diblocks: A study of miktoarm star copolymers *Macromolecules* **37** 7371–80

[85] Matsen M W 2012 Effect of architecture on the phase behavior of AB-type block copolymer melts *Macromolecules* **45** 2161–5

[86] Milner S T 1994 Chain Architecture and Asymmetry in Copolymer Microphases *Macromolecules* **27** 2333–5

[87] Matsen M W and Bates F S 1997 Conformationally Asymmetric Block Copolymers *J. Polym. Sci. Part B Polym. Phys.* **35** 945–52

[88] Widin J M, Schmitt A K, Schmitt A L, Im K and Mahanthappa M K 2012 Unexpected consequences of block polydispersity on the self-assembly of ABA triblock copolymers *J. Am. Chem. Soc.* **134** 3834–44

[89] Li Y, Qian H J, Lu Z Y and Shi A C 2013 Enhancing composition window of bicontinuous structures by designed polydispersity distribution of ABA triblock copolymers *Polymer (Guildf).* **54** 6253–60

[90] Widin J M, Schmitt A K, Im K, Schmitt A L and Mahanthappa M K 2010 Polydispersity-induced stabilization of a disordered bicontinuous morphology in ABA triblock copolymers *Macromolecules* **43** 7913–5

[91] Matsen M W 2013 Comparison of A-block polydispersity effects on BAB triblock and AB diblock copolymer melts *Eur. Phys. J. E* **36**

[92] Sides S W and Fredrickson G H 2004 Continuous polydispersity in a self-consistent field theory for diblock copolymers *J. Chem. Phys.* **121** 4974–86

[93] Aliev M A and Kuzminyh N Y 2011 Microphase separation in polydisperse miktoarm star copolymers *Phys. A Stat. Mech. its Appl.* **390** 3245–61

[94] Lynd N A and Hillmyer M A 2005 Influence of polydispersity on the self-

assembly of diblock copolymers *Macromolecules* **38** 8803–10

[95]   Meuler A J, Ellison C J, Qin J, Evans C M, Hillmyer M A and Bates F S 2009 Polydispersity effects in poly(isoprene-b-styrene-b-ethylene oxide) triblock terpolymers *J. Chem. Phys.* **130** 234903

[96]   Lynd N A, Meuler A J and Hillmyer M A 2008 Polydispersity and block copolymer self-assembly *Prog. Polym. Sci.* **33** 875–93

[97]   Noro A, Iinuma M, Suzuki J, Takano A and Matsushita Y 2004 Effect of composition distribution on microphase-separated structure from BAB triblock copolymers *Macromolecules* **37** 3804–8

[98]   Cramer N B, Reddy S K, O'Brien A K and Bowman C N 2003 Thiol - Ene Photopolymerization Mechanism and Rate Limiting Step Changes for Various Vinyl Functional Group Chemistries *Macromolecules* **36** 7964–9

[99]   Fratzl P and Weinkamer R 2007 Nature's hierarchical materials *Prog. Mater. Sci.* **52** 1263–334

[100] Weiner S and Wagner H D 1998 The Material Bone: Structure-Mechanical Function Relations *Annu. Rev. Mater. Sci.* **28** 271–98

[101] Matthec C 1998 *Design in nature: learning from trees* (Berlin: Springer: Berlin)

[102] Syurik J, Siddique R H, Dollmann A, Gomard G, Schneider M, Worgull M, Wiegand G and Hölscher H 2017 Bio-inspired, large scale, highly-scattering films for nanoparticle-alternative white surfaces *Sci. Rep.* **7** 1–11

[103] Engelmayr G C, Cheng M, Bettinger C J, Borenstein J T, Langer R and Freed L E 2008 Accordion-like honeycombs for tissue engineering of cardiac anisotropy *Nat. Mater.* **7** 1003–10

[104] Tarnow V 2002 Measured anisotropic air flow resistivity and sound attenuation of glass wool *J. Acoust. Soc. Am.* **111** 2735–9

[105] Gibson L J 2005 Biomechanics of cellular solids *J. Biomech.* **38** 377–99

[106] Deville S, Eduardo Saiz, Nalla R K and Tomsia A P 2006 Freezing as a Path to Build Complex Composites *Science* **311** 515–8

[107] Chen M, Zhu J, Qi G, He C and Wang H 2012 Anisotropic hydrogels fabricated with directional freezing and radiation-induced polymerization and crosslinking method *Mater. Lett.* **89** 104–7

[108] Guarino V, Guaccio A and Ambrosio L 2011 Manipulating co-continuous polymer blends to create PCL scaffolds with fully interconnected and anisotropic pore architecture. *J. Appl. Biomater. Biomech. JABB* **9** 34–9

[109] Washburn N R, Simon C G, Tona A, Elgendy H M, Karim A and Amis E J

2002 Co-extrusion of biocompatible polymers for scaffolds with co-continuous morphology *J. Biomed. Mater. Res.* **60** 20–9

[110] Guan J, Fujimoto K L, Sacks M S and Wagner W R 2005 Preparation and characterization of highly porous, biodegradable polyurethane scaffolds for soft tissue applications *Biomaterials* **26** 3961–71

[111] Yang F, Qu X, Cui W, Bei J, Yu F, Lu S and Wang S 2006 Manufacturing and morphology structure of polylactide-type microtubules orientation-structured scaffolds *Biomaterials* **27** 4923–33

[112] Uehara H, Yoshida T, Kakiage M, Yamanobe T and Komoto T 2006 Structural Arrangement of Crystalline/Amorphous Phases of Polyethylene-block-Polystyrene Copolymer as Induced by Orientation Techniques *J. Polym. Sci. Part B Polym. Phys.* **44** 1731–7

[113] Qiao L, Ryan A J and Winey K I 2002 A correlation between lamellar contraction and applied shear stress in diblock copolymers *Macromolecules* **35** 3596–600

[114] Arns C H, Knackstedt M A, Roberts A P and Pinczewski V W 1999 Morphology, Cocontinuity, and Conductive Properties of Anisotropic Polymer Blends *Macromolecules* **32** 5964–6

[115] Hermel T J, Hahn S F, Chaffin K A, Gerberich W W and Bates F S 2003 Role of molecular architecture in mechanical failure of glassy/semicrystalline block copolymers: CEC vs CECEC lamellae *Macromolecules* **36** 2190–3

[116] Ha Y H and Thomas E L 2002 Deformation behavior of a roll-cast layered-silicate/lamellar triblock copolymer nanocomposite *Macromolecules* **35** 4419–28

[117] Aida S, Sakurai S and Nomura S 2002 Strain-induced ordering of microdomain structures in polystyrene-block- polybutadiene-block-polystyrene triblock copolymers cross-linked in the disordered state *Polymer (Guildf).* **43** 2881–7

[118] Sakurai S, Aida S, Okamoto S, Sakurai K and Nomura S 2003 Mechanism of thermally induced morphological reorganization and lamellar orientation from the herringbone structure in cross-linked polystyrene-block-polybutadiene-block-polystyrene triblock copolymers *Macromolecules* **36** 1930–9

[119] Sakurai S, Aida S, Okamoto S, Ono T, Imaizumi K and Nomura S 2001 Preferential orientation of lamellar microdomains induced by uniaxial stretching of cross-linked polystyrene-block-polybutadiene-block-polystyrene triblock copolymer *Macromolecules* **34** 3672–8

[120] Zhang J and Li C M 2012 Nanoporous metals: Fabrication strategies and advanced electrochemical applications in catalysis, sensing and energy systems *Chem. Soc. Rev.* **41** 7016–31

[121] Juarez T, Biener J, Weissmüller J and Hodge A M 2017 Nanoporous Metals with Structural Hierarchy: A Review *Adv. Eng. Mater.* **19** 1–23

[122] Hepburn C 1982 *Polyurethane Elastomers*

[123] Wirpsza Z 1994 *Polyurethanes: chemistry, technology, and applications*

[124] Warner M, Bladon P and Terentjev E M 1994 "Soft elasticity" - deformation without resistance in liquid crystal elastomers *J. Phys. II* **4** 93–102

[125] Cohen Y, Albalak R J, Dair B J, Capel M S and Thomas E L 2000 Deformation of Oriented Lamellar Block Copolymer Films *Macromolecules* **33** 6502–16

[126] Cohen Y, Brinkmann M and Thomas E L 2001 Undulation, dilation, and folding of a layered block copolymer *J. Chem. Phys.* **114** 984–92

[127] Duan Y, Thunga M, Schlegel R, Schneider K, Rettler E, Weidisch R, Siesler H W, Stamm M, Mays J W and Hadjichristidis N 2009 Morphology and deformation mechanisms and tensile properties of tetrafunctional multigraft copolymers *Macromolecules* **42** 4155–64

[128] Cooper S J, Bertei A, Shearing P R, Kilner J A and Brandon N P 2016 TauFactor: An open-source application for calculating tortuosity factors from tomographic data *SoftwareX* **5** 203–10

[129] Sakai T, Matsunaga T, Yamamoto Y, Ito C, Yoshida R, Suzuki S, Sasaki N, Shibayama M and Chung U Il 2008 Design and fabrication of a high-strength hydrogel with ideally homogeneous network structure from tetrahedron-like macromonomers *Macromolecules* **41** 5379–84

[130] I. M. Ward 1997 *Structure and Properties of Oriented Polymers* ed Ian Ward (London: Chapman and Hall, London)

[131] Grijpma D W, Altpeter H, Bevis M J and Feijen J 2002 Improvement of the mechanical properties of poly(D,L-lactide) by orientation *Polym. Int.* **51** 845–51

[132] Weidisch R, Stamm M, Michler G H, Fischer H and Jérôme R 1999 Mechanical Properties of Weakly Segregated Block Copolymers. 3. Influence of Strain Rate and Temperature on Tensile Properties of Poly(styrene-b-butyl methacrylate) Diblock Copolymers with Different Morphologies *Macromolecules* **32** 742–50

[133] Weidisch R, Michler G H, Arnold M and Fischer H 2000 Mechanical properties of weakly segregated block copolymers. Part IV. Influence of

chain architecture and miscibility on tensile properties of block copolymers *J. Mater. Sci.* **35** 1257–68

[134] Bates F S, Hillmyer M A, Lodge T P, Bates C M, Delaney K T and Fredrickson G H 2012 Multiblock Polymers : Panacea or Pandora's Box? *Science (80-.).* **336** 434–40

[135] Li Z, Kesselman E, Talmon Y, Hillmyer M A and Lodge T P 2004 Multicompartment micelles from ABC miktoarm stars in water *Science (80-.).* **306** 98–101

[136] Zhang L and Eisenberg A 1995 Multiple Morphologies of "Crew-Cut" Aggregates of Polystyrene-b-poly (acrylic acid) Block Copolymers *Science (80-.).* **268** 1728–31

[137] Russell T P, Karis T E, Gallot Y and Mayes A M 1994 A lower critical ordering transition in a diblock copolymer melt *Nature* **368** 729–31

[138] Lee I and Bates F S 2013 Synthesis, Structure, and Properties of Alternating and Random Poly(styrene-b-butadiene) Multiblock Copolymers *Macromolecules* **46** 4529–39

[139] Walker C N, Sarapas J M, Kung V, Hall A L and Tew G N 2015 Multiblock Copolymers by Thiol Addition Across Norbornene *ACS Macro Lett.* **3** 453–7

[140] Koo C M, Hillmyer M A and Bates F S 2006 Structure and properties of semicrystalline - Rubbery multiblock copolymers *Macromolecules* **39** 667–77

[141] Duan Y, Thunga M, Schlegel R, Schneider K, Rettler E, Weidisch R, Siesler H W, Stamm M, Mays J W and Hadjichristidis N 2009 Morphology and deformation mechanisms and tensile properties of tetrafunctional multigraft copolymers *Macromolecules* **42** 4155–64

[142] Sarapas J M, Saijo K, Zhao Y, Takenaka M and Tew G N 2016 Phase behavior and Li+ Ion conductivity of styrene-ethylene oxide multiblock copolymer electrolytes *Polym. Adv. Technol.* **27** 946–54

[143] Kavassalis T A and Whitmore M D 1991 On the theory of linear multiblock copolymers *Macromolecules* **24** 5340–5

[144] Leibler L 1980 Theory of microphase separation in block copolymers *Macromolecules* **13** 1602–17

[145] Bates F S and Fredrickson G H 1990 Block copolymer thermodynamics: theory and experiment. *Annu. Rev. Phys. Chem.* **41** 525–57

[146] Lee I, Panthani T R and Bates F S 2013 Sustainable Poly(lactide- b - butadiene) Multiblock Copolymers with Enhanced Mechanical Properties

Macromolecules **46** 7387–98

[147] Li S, Register R A, Weinhold J D and Landes B G 2012 Melt and solid-state structures of polydisperse polyolefin multiblock copolymers *Macromolecules* **45** 5773–81

[148] Park H E, Dealy J M, Marchand G R, Wang J, Li S and Register R A 2010 Rheology and structure of molten, olefin multiblock copolymers *Macromolecules* **43** 6789–99

[149] Koo C M, Hillmyer M A and Bates F S 2006 Structure and properties of semicrystalline-rubbery multiblock copolymers *Macromolecules* **39** 667–77

[150] Lim L S, Harada T, Hillmyer M A and Bates F S 2004 High strength polyolefin block copolymers *Macromolecules* **37** 5847–50

[151] Wu L, Cochran E W, Lodge T P and Bates F S 2004 Consequences of block number on the order-disorder transition and viscoelastic properties of linear (AB) n multiblock copolymers *Macromolecules* **37** 3360–8

[152] Edson J B, Wang Z, Kramer E J and Coates G W 2008 Fluorinated bis(phenoxyketimine)titanium complexes for the living, isoselective polymerization of propylene: Multiblock isotactic polypropylene copolymers via sequential monomer addition *J. Am. Chem. Soc.* **130** 4968–77

[153] Arriola D J, Carnahan E M, Hustad P D, Kuhlman R L and Wenzel T T 2006 Catalytic Production of Olefin Block Copolymers via Chain Shuttling Polymerization *Science (80-.).* **312** 714–9

[154] Sarapas J M and Tew G N 2016 Thiol-Ene Step-Growth as a Versatile Route to Functional Polymers *Angew. Chemie - Int. Ed.* **55** 15860–3

[155] Zhu Y, Radlauer M R, Schneiderman D K, Shaffer M S P, Hillmyer M A and Williams C K 2018 Multiblock Polyesters Demonstrating High Elasticity and Shape Memory Effects *Macromolecules* **51** 2466–75

[156] Akindoyo J O, Beg M D H, Ghazali S, Islam M R, Jeyaratnam N and Yuvaraj A R 2016 Polyurethane types, synthesis and applications-a review *RSC Adv.* **6** 114453–82

[157] Amass W, Amass A and Tighe B 1998 A review of biodegradable polymers: Uses, current developments in the synthesis and characterization of biodegradable polyesters, blends of biodegradable polymers and recent advances in biodegradation studies *Polym. Int.* **47** 89–144

[158] Cowie J M G and Arrighi V 2007 *Polymers: Chemistry and Physics of Modern Materials* (CRC press)

[159] Bates, F S. R J H F G H 1990 Fluctuation effects in a symmetric diblock

copolymer near the order-disorder transition *J. Chem. Phys.* **92** 6255–70

[160] Fried H and Binder K 1991 The microphase separation transition in symmetric diblock copolymer melts: A Monte Carlo study *J. Chem. Phys.* **94** 8349–66

[161] Vassiliev O N and Matsen M W 2003 Fluctuation effects in block copolymer melts *J. Chem. Phys.* **118** 7700–13

[162] Schmitt A K and Mahanthappa M K 2014 Characteristics of lamellar mesophases in strongly segregated broad dispersity ABA triblock copolymers *Macromolecules* **47** 4346–56

[163] Vidil T, Hampu N and Hillmyer M A 2017 Nanoporous Thermosets with Percolating Pores from Block Polymers Chemically Fixed above the Order-Disorder Transition *ACS Cent. Sci.* **3** 1114–20

[164] Krause S 1970 Microphase separation in block copolymers: Zeroth approximation *Macromolecules* **3** 84–6

[165] Fredrickson G H, Milner S T and Leibler L 1992 Multicritical Phenomena and Microphase Ordering in Random Block Copolymers Melts *Macromolecules* **25** 6341–54

[166] Pernot H, Baumert M, Court F and Leibler L 2002 Design and properties of co-continuous nanostructured polymers by reactive blending *Nat. Mater.* **1** 54–8

[167] Ruzette A V and Leibler L 2005 Block copolymers in tomorrow's plastics *Nat. Mater.* **4** 19–31

[168] Beyer F L, Gido S P, Büschl C, Iatrou H, Uhrig D, Mays J W, Chang M Y, Garetz B A, Balsara N P, Tan N B and Hadjichristidis N 2000 Graft copolymers with regularly spaced, tetrafunctional branch points: morphology and grain structure *Macromolecules* **33** 2039–48

[169] Zhu Y, Burgaz E, Gido S P, Staudinger U, Weidisch R, Uhrig D and Mays J W 2006 Morphology and tensile properties of multigraft copolymers with regularly spaced tri-, tetra-, and hexafunctional junction points *Macromolecules* **39** 4428–36

[170] Mao H and Hillmyer M A 2006 Macroscopic samples of polystyrene with ordered three-dimensional nanochannels *Soft Matter* **2** 57–9

[171] Song J and Cho B K 2013 Mesoporous polystyrenes via lamellar block copolymer assembly *Bull. Korean Chem. Soc.* **34** 23–4

[172] Knapp B and Kohl P A 2014 Selective Etching of Polylactic Acid in Poly(styrene)-Block-Poly(D,L)Lactide Diblock Copolymer for Nanoscale Patterning *J. Appl. Polym. Sci.* **131**

[173] Patel A J, Mochrie S, Narayanan S, Sandy A, Watanabe H and Balsara N P 2010 Dynamic signatures of microphase separation in a block copolymer melt determined by X-ray photon correlation spectroscopy and rheology *Macromolecules* **43** 1515–23

[174] Jang W-S, Koo P, Sykorsky M, Narayanan S, Sandy A and Mochrie S G J 2013 The Static and Dynamic Structure Factor of a Diblock Copolymer Melt via Small-Angle X-ray Scattering and X-ray Photon Correlation Spectroscopy *Macromolecules* **46** 8628–37

[175] Rodwogin M D, Spanjers C S, Leighton C and Hillmyer M A 2010 Polylactide-Poly(dimethylsiloxane)-Polylactide Triblock Copolymers as Multifunctional Materials for Nanolithographic Applications *ACS Nano* **4** 725–32

[176] Hsueh H Y, Chen H Y, Hung Y C, Ling Y C, Gwo S and Ho R M 2013 Well-defined multibranched gold with surface plasmon resonance in near-infrared region from seeding growth approach using gyroid block copolymer template *Adv. Mater.* **25** 1780–6

[177] Lee H C, Hsueh H Y, Jeng U S and Ho R M 2014 Functionalized nanoporous gyroid SiO2with double-stimuli- responsive properties as environment-selective delivery systems *Macromolecules* **47** 3041–51

[178] Robbins S W, Beaucage P A, Sai H, Tan K W, Werner J G, Sethna J P, Disalvo F J, Gruner S M, Dover R B Van and Wiesner U 2016 Block copolymer self-assembly – directed synthesis of mesoporous gyroidal superconductors *Sci. Adv.* 1–8

[179] Tan K W, Jung B, Werner J G, Rhoades E R, Thompson M O and Wiesner U 2015 Transient laser heating induced hierarchical porous structures from block copolymer – directed self-assembly *Science (80-.).* **349** 54–9

[180] Vanderlaan M E and Hillmyer M A 2016 "Uncontrolled" Preparation of Disperse Poly(lactide)-block-poly(styrene)-block-poly(lactide) for Nanopatterning Applications *Macromolecules* **49** 8031–40

[181] Legge T M, Slark A T and Perrier S 2007 Novel difunctional Reversible Addition Fragmentation Chain Transfer (RAFT) agent for the synthesis of telechelic and ABA triblock methacrylate and acrylate copolymers *Macromolecules* **40** 2318–26